ACOUSTIC SOURCE ANALYSIS OF A SUPERSONIC RECTANGULAR CHEVRON JET

A THESIS

SUBMITTED TO THE FACULTY OF THE

UNIVERSITY OF MINNESOTA

BY

Jordan Richard Kreitzman

IN PARTIAL FULFILLMENT OF THE REQUIREMENTS

FOR THE DEGREE OF

MASTER OF SCIENCE

Joseph W. Nichols, Adviser

June 2015

Acknowledgments

I would first and foremost like to thank my research adviser, Dr. Joseph W. Nichols. He assisted and oversaw all of the work that was done for this thesis. Without his constant help, this work would not be possible. I would like to thank the Argonne National Laboratory for their computational resources. Their resources were very helpful, especially for extracting the mesh that was used throughout all of the research. I would like to thank the Aerospace Engineering and Mechanics Department at the University of Minnesota-Twin Cities for all of their resources as well. Finally, I'd like to thank my family for their endless support.

Abstract

In this thesis, acoustic source terms corresponding to Goldstein's generalized acoustic analogy are computed from a high-fidelity simulation of a supersonic jet issuing from a rectangular nozzle with chevrons. The simulation data are validated against experimental measurements from a flow configuration involving a nozzle of precisely the same geometry. A statistical description of the simulated flow field is established in detail including an in-depth look at first, second, and fourth order statistics.

This thesis investigates the theoretical underpinning of reduced-order acoustic source models by testing the assumptions of quasi-normality and statistical axisymmetry. First, the quasi-normality hypothesis is tested using Millionshchikov's identity. This identity allows fourth order acoustic source statistics to be expressed in terms of second order statistics. This is a simplifying assumption upon which most of the models rely. In addition, local statistical axisymmetry is tested using basic quadratic forms of the fourth order correlation terms to determine if local fluctuations in the transverse directions of the flow are equivalent. It is found that the flow field is not quasi-normal in the axial direction but is however quasi-normal in the transverse directions. Our analysis also shows that the flow is locally statistically axisymmetric close to the edges of the flow field but not near the center.

Previously used acoustic source models are fit to the fourth order correlation statistics. Specifically, this thesis performs a detailed analysis of four different models: the Gaussian model, moving-frame model, fixed-frame model, and modified-distance model. These

models were previously used to describe correlation data from axisymmetric jets. In this thesis, we assess the accuracy of these models in the context of highly complex nozzle shapes. The latter three models are found to be similar in accuracy, while the Gaussian model is found to be a poorer fit.

The thesis concludes with an analysis of the large scale turbulent structures in the flow field. It is observed that there is noticeable large scale coherence near the edges of the flow. Therefore, since large scale coherence is a primary mechanism of sound generation, it is believed that the large scale turbulence significantly contributes to the sound generated from this complex flow field.

Contents

List of Tables

List of Figures

Nomenclature

α	scaling factor for testing the quasi-normality hypothesis
$\bar{u}_i$	i^{th} component of the basic time averaged velocity field
Δ_1	axial component of the spatial separation vector
δ_{ij}	Kronecker delta
γ	ratio of specific heats
$\hat{R}_{ijkl}$	cross correlation 4^{th} order tensor using basic time averages and no density inclusion
$\hat{T}_{ij}$	mean Reynolds stress using basic time averages and no density inclusion
μ	first coefficient of viscosity
ρ	density of the flow field
σ_{ij}	stress tensor including both compressive and viscous stresses
σ_{u_i}	standard deviation of the i^{th} component of velocity
τ	time delay
τ_s	time scale fit for all four acoustic source models

$\vec{x}$	spatial vector in the flow field
$\widetilde{v_1}$	convection velocity fit for all four acoustic source models
$\widetilde{T}_{ij}$	mean Reynolds stress using Favre averages with density inclusion
$\widetilde{u}_i$	i^{th} component of the Favre averaged velocity field
A	amplitude for the Gaussian curve fit for the histogram
a, b, c	coefficient fits for the simplified Gaussian model
A_{ijkl}	amplitude fit for all four acoustic source models
b_1	peak-decay shape regulator fit for axial spatial separations for the modified-distance model
c_0	speed of sound in a uniform medium
c_p	heat capacity at constant pressure
c_v	heat capacity at constant volume
D_e	nozzle equivalent diameter
dt	time delay
E	total energy of the flow field
e	internal energy of the flow field
$E[X]$	expectation operator
f	frequency
KE	kinetic energy of the flow field

l_0	length scale 0 fit for the fixed-frame model
l_1	axial length scale fit for all four acoustic source models
p	pressure of the flow field
R	ideal gas constant
R_{ijkl}	cross correlation 4^{th} order tensor using Favre averages with density inclusion
SK	skewness
St	Strouhal number
T	temperature of the flow field
T'_{ij}	fluctuating Reynolds stress
T^L_{ij}	external stresses in the Lighthill analogy
u_i	i^{th} component of the velocity field
u'_i	i^{th} component velocity fluctuations about the basic time average
u''_i	i^{th} component velocity fluctuations about the Favre average
U_j	center line jet velocity coming out of the nozzle
V	total velocity of the flow field
x'	independent variable for the Gaussian curve fit for the histogram and the simplified Gaussian model
x_i	i^{th} component of the spatial dimensions
$y(x')$	dependent variable for the Gaussian curve fit for the histogram and the simplified Gaussian model

Chapter 1

Introduction

1.1 Motivation

Reducing jet noise is becoming increasingly important. For one, jet noise has always been a problem for communities living near airports and military bases. The number of flights and airports are continuously increasing year to year. Future populations will likely be forced to live near airports, so reducing jet noise is a vital research topic [4].

Also, the problem of noise on aircraft carrier flight decks is still a major concern for deck personnel. The decibel level on the flight decks can reach 150 dB [5]. While improvements have been made to hearing protection, it still does not provide complete protection from the high decibel levels generated by the exhausts of tactical aircraft. Therefore, jet noise poses a serious health risk for safety personnel in close proximity. Commercial airliners have achieved more reduction in noise levels compared to military aircraft. This is due to the noise regulations enforced on the design of commercial airliners. There is no maximum sound decibel level by which military aircraft must abide [5].

Supersonic jet noise could be a major problem in the future due to military aircraft continuously being engineered to reach quicker speeds [5]. Lighthill's U_j^8 power law

for jet noise indicates that acoustic power is proportional to the eighth power of the jet velocity coming out of the nozzle [6]. Therefore, this indicates that faster jets produce more acoustic power. Also, supersonic jets produce additional noise due to the formation of shock diamonds. Supersonic aircraft will become more prevalent in the future, so the need for jet noise research is becoming more of a necessity. While attempting to reduce the shock produced noise is a very important topic, it is also important to look into methods of reducing turbulent mixing noise by analyzing acoustic sources in the turbulent flow field [2].

A previous study applied an unstructured finite-volume large eddy simulation (LES) solver to simulate a rectangular supersonic turbulent jet both with and without chevrons [2]. This specific high fidelity simulation was needed for the research done in this thesis for a number of reasons. For one, it allows for the analysis of the fine scales of turbulence. This is a mechanism of sound generation, and the refined grid allows these turbulence scales to be seen and analyzed as acoustic sources. Also, high-fidelity simulations provide access to complete flow fields in such refined detail that is hard to recreate in a laboratory. An unstructured mesh in particular is an ideal setup for complex geometries such as a rectangular nozzle with chevrons [2]. Another benefit of this simulation is that the solver utilizes wider numerical stencils to minimize numerical dissipation, an important feature for aeroacoustic prediction [7].

Because current jet noise technologies rely upon complex geometry, we expect a careful assessment of acoustic source models in this context to have important practical value to design. Acoustic source models developed for axisymmetric jets are currently the industry gold standard for design of chevron nozzles. The topic of analyzing acoustic sources from supersonic nonaxisymmetric chevron jets is a topic that will most certainly have value, especially in the near future. These types of nozzles have been under analysis for a while now. While supersonic rectangular jets have been studied experimentally, the

recent availability of large-scale simulation has provided unprecedented access to complete flow fields needed to compute acoustic source terms.

1.2 Past research

Supersonic jet noise has been studied extensively in the past and is generally thought to be composed of three parts: turbulent mixing noise, broadband shock-associated noise, and screech tones [8]. With regard to turbulent mixing noise, it is composed of two different parts: the fine-scale turbulence and large coherent structures [8]. This thesis is primarily concerned with fine-scale turbulence, but large scale turbulent structures are also considered. In fact, the large scale motions are responsible for peak noise, although it is confined to the downstream direction. Fine-scale turbulence, on the other hand, is important for predicting lateral sound levels which are more difficult to predict correctly. Fine-scale turbulence noise is less directional than the Mach wave radiation generated from large coherent structures [9; 10]. While research in supersonic jet noise has come a long way, there is still a need for more supersonic jet analysis pertaining to non-circular jets, fine-scale turbulence, and computational methods in aeroacoustics [9].

Since a rectangular nozzle is nonaxisymmetric, the sound has been found to be louder and softer depending on the axis. Paliath & Morris found that the sound propagating parallel to the major axis of a rectangular jet is quieter compared to that propagating parallel to the minor axis [11]. This was an important discovery because it showed that rectangular nozzles can change the directivity of the sound, and this means that high sound levels can potentially be directed away from people. Comparing to axisymmetric nozzles, Tam actually found that maximum sound levels for different nozzle geometries are nearly identical [12]. Tam & Zaman also concluded that modifying nozzle geometry was not a good method for achieving a reduction in noise [13]. This was based on experimental measurements. However, they did observe a small reduction in downstream sound using

chevron-type flow disturbers. They concluded that large scale turbulent structure sound is slightly reduced by the use of chevrons by shifting the power spectrum peak of the flow to a higher frequency. Nichols et al. also showed that adding chevrons to a rectangular jet substantially reduces the sound [2]. This reduction in noise was seen for low to mid frequencies, while high frequency noise actually increased slightly. They found that the overall reduction in sound was primarily due to reductions in broadband-shock associated noise and noise due to large turbulent structures.

Acoustic source modeling has primarily focused upon axisymmetric jets. Tam & Auriault proposed a three parameter Gaussian model for fine-scale turbulence [14]. The turbulence information was found from a $k - \epsilon$ model, while the three parameters were found from fitting calculated noise spectra to experimental data. The model produced good results, but due to the empiricism of the model, they stated that much improvement could be made. However, they obtained good results for both subsonic and supersonic jets. Among others, Morris & Farassat successfully applied this Gaussian model among other similar Gaussian models to turbulent flow [15]. Past this, Afsar et al. applied the Gaussian model, proposed by Tam & Auriault, to LES simulated data [16]. Karabasov et al. successfully applied a Gaussian acoustic source model to LES simulations of subsonic axisymmetric jets [17; 18; 19].

Goldstein & Leib introduced a moving-frame model for fine-scale turbulence [20]. The results were successful when comparing to experimental data and proved that the moving-frame model is arguably a better model for acoustic sources than the Gaussian model due to its ability to account for the cusp behavior of the correlation calculations at zero spatial separation. It is even flexible enough to account for the negative correlation values at large time delays, although that aspect of the model is not analyzed in this thesis.

Improving upon the moving-frame model, Leib & Goldstein introduced a fixed-frame model [21]. This model was introduced because it was found that based on more re-

cent experimental data, the fixed-frame model was thought to better model turbulent flow characteristics than the moving-frame model. The fixed-frame model was tested for both subsonic and supersonic turbulent jets and found to be in even better agreement with Harper-Bourne measurements [22] than the moving-frame model.

Bassetti & Morfey first introduced a modified-distance model [23]. The modified-distance model was compared to other models, such as a Gaussian model and exponential-Gaussian model, and experimental data from Harper-Bourne [22]. The modified-distance model was the best fit out of the three models to the Harper-Bourne measurements. The modified-distance model has also been used to model turbulence outputted from an LES simulation by Bassetti & Nichols [24]. The model continued to show cusp-like behavior at zero spatial separation and bell-like behavior when spatial offsets were introduced.

The next chapter of this thesis will be devoted to explaining the configuration of the analyzed flow field as well as validating the physics of the flow. From there, the thesis will cover in detail all of the theory and methodology pertinent to the flow analysis. After this, results for single point statistics will be shown in detail. This includes an in-depth look at first, second, and fourth order statistics as well as tests for the validity of quasi-normality and statistical axisymmetry assumptions. Next, an extensive look at the accuracy of the proposed acoustic source models will be shown. Finally, large scale turbulent structures will be shown in detail for both center planes and full three dimensional views.

Chapter 2

Flow configuration/validation

2.1 Nozzle and flow details

The thesis begins with an understanding of the flow field. This particular flow modeled the NA2C3 geometry that was also used for experimental testing at the NASA Glenn Research Center [1].

Figure 2.1 illustrates the nozzle geometry and the coordinate system used throughout the entire thesis. The rectangular jet has an aspect ratio of 2:1 with four large chevrons attached to each of the long edges. The chevrons extend into the flow and generate streamwise vorticity. The produced jet is isothermal and supersonic with a fully-expanded jet Mach number of 1.4. The ratio of the stagnation pressure inside the nozzle reservoir to the ambient pressure is 3.18, while the ratio of the stagnation temperature inside the nozzle reservoir to the ambient temperature is 1.391. The nozzle is also purely convergent so that the produced supersonic jet is underexpanded and contains shocks. The Reynolds number with respect to the nozzle equivalent diameter and fully expanded conditions is 1.5 x 10^6. The nozzle equivalent diameter is defined as the diameter of a circle with the same area as the nozzle [2].

Figure 2.2 top shows an axial cross section of the instantaneous temperature field of

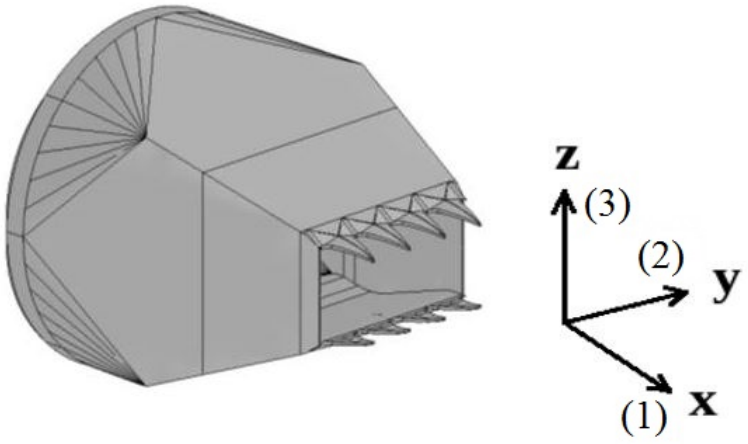

Figure 2.1: Rectangular nozzle with chevrons (NA2C3 geometry) and coordinate system [1].

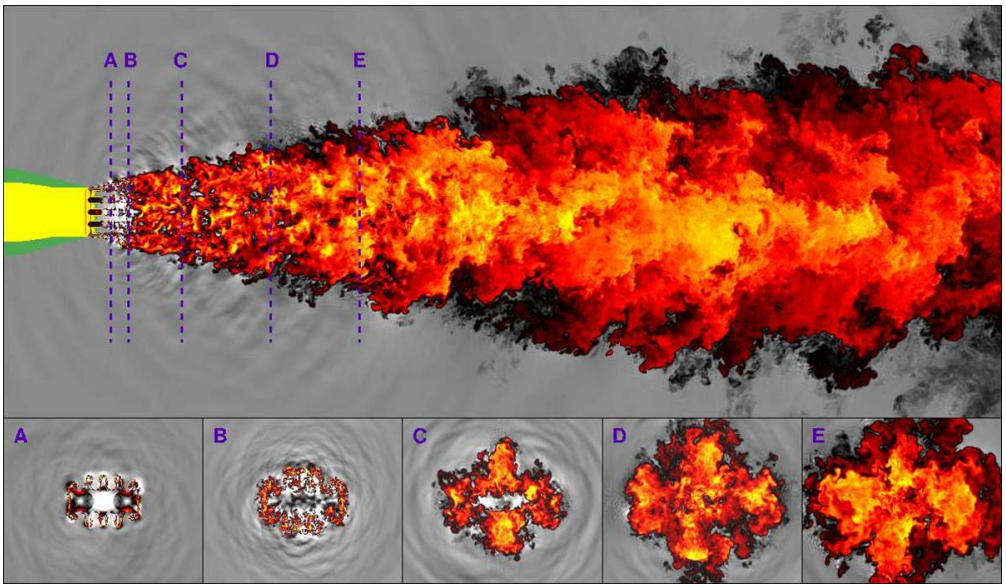

Figure 2.2: Instantaneous temperature field of the flow showing “plus-shaped” cross section downstream due to side jet effect [2].

the generated flow taken near the lipline of the nozzle. Figure 2.2 bottom shows five radial cross sections taken at different spatial locations in the flow field. Analyzing these radial cross sections, one can see that the chevrons produce side jets. This is due to the jet being underexpanded coming out of the nozzle, so the fluid gets squeezed out between the chevrons by the over-pressure at the outlet. These side jets gradually merge into a "plus-shaped" cross section. Another result of these side jets is that they enhance turbulent mixing in areas away from the axis of the jet. The chevrons used to generate the flow field also create additional weak shocks due to shocks being created at both the chevron tips and the areas in between the chevrons. This causes the shock cells of the rectangular jet to be broken up into many small shock cells. This process leads to the jet expanding in an abundance of small steps instead of a few large steps. This reduces the sound [2]. While shock associated noise is not analyzed in this thesis, it is still an important benefit of chevron use.

The chevron jet simulation was a part of a larger group of simulations that involved rectangular nozzles with and without chevrons as well as different mesh resolutions [2]. This allowed for a better understanding of how the chevron rectangular jet behaves differently than the no chevron rectangular jet.

2.2 Flow domain and simulation details

The domain of the simulated flow field includes the flow both inside and outside of the nozzle extending out to thirty times the nozzle equivalent diameter. The high-fidelity simulation was a peta-scale computation consisting of a mesh with 528 million control volumes. The control volumes were "purely hexahedral elements which were body fitted to the nozzle geometry by means of an adaptive refinement procedure" [2]. The simulation was run in parallel using up to 163,840 processors at the Argonne National Laboratory. It consumed a total of 17 million CPU-hours and took four days to run. By the end of the

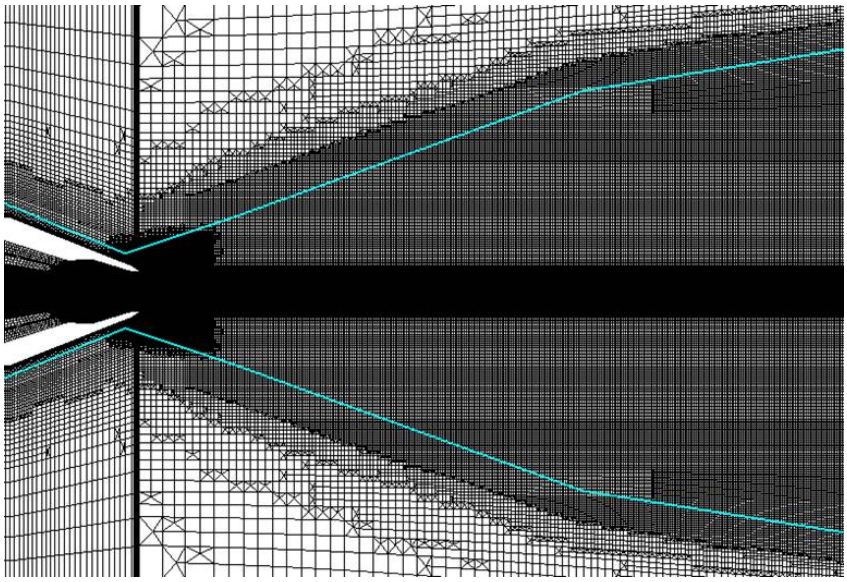

Figure 2.3: Hexahedral mesh visualization [2].

simulation, there were almost 200 Tb of data outputted [2]. A visualization of the mesh is shown in figure 2.3. In addition to this, the flow simulation utilized a time step of 0.001 and outputted snapshots of the flow data every 100 time steps.

2.3 Validation of the flow field

As stated before, the rectangular chevron nozzle (NA2C3 geometry) was used for experimental testing at the NASA Glenn Research Center [1]. This allowed for validation of the simulated flow field. Validation ensures that the simulated physics can be trusted for the current study done in this thesis. Figure 2.4 shows a comparison of the mean velocity of the flow field between the experimental data and the simulated data. The experimental data reside on the top half, while the simulated data reside on the bottom half. As one can see, the experimental data line up with the simulated data very well. There are a couple of slight differences though. The shear layer near the nozzle does appear to be slightly thicker with the experimental data. This is due to the surface roughness of the nozzle

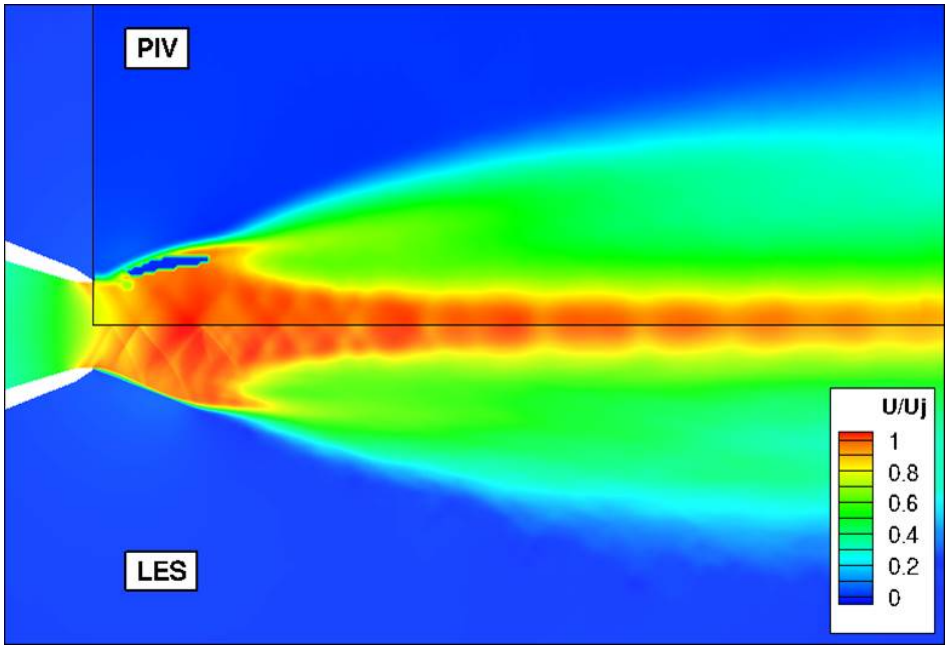

Figure 2.4: Validation of the simulated flow field's mean velocity.

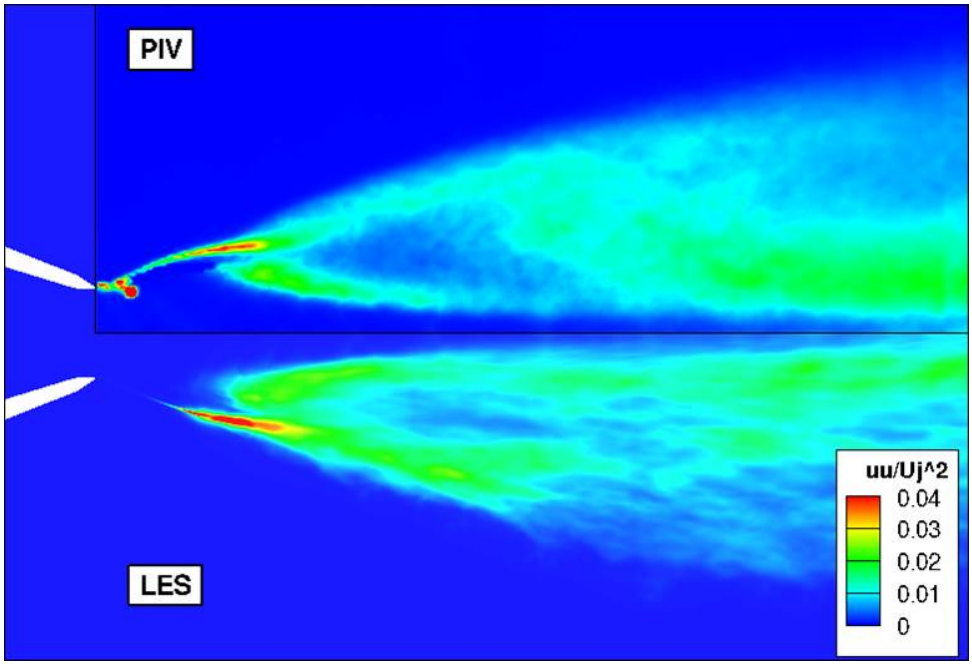

Figure 2.5: Validation of the simulated flow field's mean Reynolds stress.

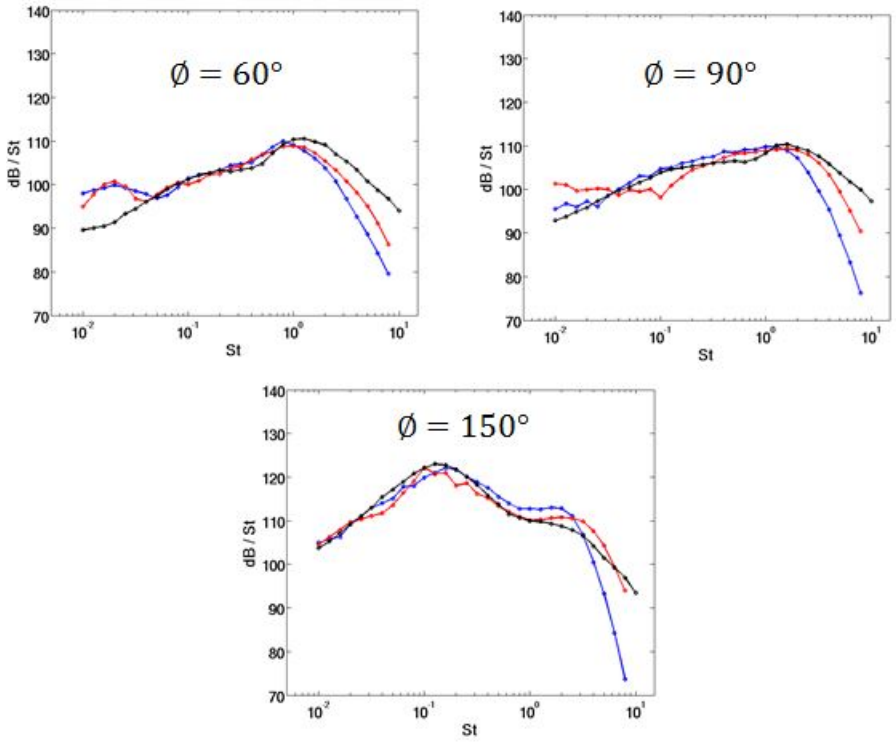

Figure 2.6: Validation of the simulated flow field's farfield acoustics [2].

creating more turbulence in the flow field as it exits the nozzle. Surface roughness was not included in the flow field simulation [2]. Another observation to point out is that there is an area of zero mean velocity in the flow field near the nozzle with the experimental data. This is simply due to the speed of the fluid being too fast for the sensors in the experiment to measure at that location. Figure 2.5 shows a comparison of the turbulence statistics between the experimental and simulated data. Once again, the two data sets line up pretty well other than the increased shear layer in the experimental data due to the surface roughness of the nozzle.

Validation of the simulated farfield acoustics is also very important. Figure 2.6 is a representation of that validation. The plots are for observer angles of 60°, 90°, and 150°. The black curves represent the experimental data. The red curves represent the simulated data using 528 million control volumes. The blue curves represent the simulated

data using 100 million control volumes. The blue curves are simply there to show that the simulation converges properly with increased grid resolution [2]. The black and red curves line up well with each other. This is further proof that the simulated data model the physics of the actual flow field quite well.

Chapter 3

Theory and Methodology

3.1 Acoustic analogies

3.1.1 The Lighthill analogy

The Lighthill acoustic analogy is derived from the compressible, viscous Navier-Stokes equations. Equation 3.1 is the conservation of mass equation, while equation 3.2 is the conservation of momentum equation [25]. Equation 3.3 defines the stress tensor used in equation 3.2.

$$\frac{\partial \rho}{\partial t} + \frac{\partial}{\partial x_i}(\rho u_i) = 0 \tag{3.1}$$

$$\frac{\partial}{\partial t}(\rho u_i) + \frac{\partial}{\partial x_j}(\rho u_i u_j - \sigma_{ij}) = 0 \tag{3.2}$$

$$\sigma_{ij} = -p\delta_{ij} + \mu\left(\frac{\partial u_i}{\partial x_j} + \frac{\partial u_j}{\partial x_i} - \frac{2}{3}\frac{\partial u_k}{\partial x_k}\delta_{ij}\right) \tag{3.3}$$

If one takes the time derivative of equation 3.1 and the divergence of equation 3.2, equations 3.4 and 3.5 are the result.

$$\frac{\partial^2 \rho}{\partial t^2} + \frac{\partial}{\partial t}\frac{\partial}{\partial x_i}(\rho u_i) = 0 \tag{3.4}$$

$$\frac{\partial}{\partial t}\frac{\partial}{\partial x_i}(\rho u_i) + \frac{\partial}{\partial x_i}\frac{\partial}{\partial x_j}(\rho u_i u_j - \sigma_{ij}) = 0 \tag{3.5}$$

Equations 3.4 and 3.5 are then combined to form the Lighthill analogy which is represented by equations 3.6 and 3.7. The form of equation 3.6 is an inhomogeneous wave equation where the acoustic source term is on the right hand side and of quadrupole-type [25].

$$\frac{\partial^2 \rho}{\partial t^2} - c_0^2 \nabla^2 \rho = \frac{\partial^2 T_{ij}^L}{\partial x_i \partial x_j} \tag{3.6}$$

$$T_{ij}^L = \rho u_i u_j - \sigma_{ij} - c_0^2 \rho \delta_{ij} \tag{3.7}$$

There are a couple of things to note about the T_{ij}^L term. The transformation of acoustic energy into heat by viscous forces and heat conduction typically occurs in a slow manner. Therefore, the inclusion of the viscous stresses in the T_{ij}^L term is usually unnecessary. Also, if the temperature of the flow field departs minimally from a uniform state, then the ($p\delta_{ij}$ - $c_0^2 \rho \delta_{ij}$) expression is also negligible. This means that the main source of sound is the fluctuating Reynolds stresses [25]. Equation 3.8 shows this approximation.

$$T_{ij}^L \approx \rho u_i u_j \tag{3.8}$$

The Lighthill analogy was a revolutionary discovery that showed that fluctuating Reynolds stresses are a primary mechanism of sound generation in a turbulent flow. This primary concept has been included in every type of acoustic analogy since the Lighthill analogy.

3.1.2 Goldstein's generalized acoustic analogy

The Lighthill analogy proved to be a very successful method for determining sound radiation from turbulent jet noise. However, jet engine manufacturers soon became aware that they needed a model that could detect changes in sound radiation for even the slightest change in flow conditions, and they sought to improve upon Lighthill's original analogy [26].

Acoustic analogy approaches, such as Lighthill's analogy, generally treat the nonlinear generalized Reynolds stresses and enthalpy flux as established source terms that can be predicted. There are, however, situations in which the base-flow sources contribute the most to the source terms of the flow [26]. Goldstein showed that the Navier-Stokes equations can be rearranged as a set of linearized inhomogeneous Euler equations (LIE) with source terms that are identical to externally imposed shear stress and energy flux perturbations [26]. These equations show that "there is an exact analogy between the fluctuations in any real flow and the linear inviscid fluctuations about an arbitrary base flow produced by externally imposed stress and energy flux perturbations" [26]. This process is known as Goldstein's generalized acoustic analogy and is used for analyzing acoustic sources in this thesis.

3.2 Background and calculation of R_{ijkl}

When analyzing turbulence and aeroacoustics, correlations characterize the spatio-temporal behavior of fluctuations [27]. The two-point, two-time Reynolds stress cross correlation tensor, R_{ijkl}, is of fourth order and an important quantity for determining jet noise because the farfield acoustic spectrum results when R_{ijkl} is convolved with an appropriate Green's function [18]. For a given spatial location and time delay, R_{ijkl} is simply a calculation involving a specific point and spatial offset in the flow field where the fluctuating

Reynolds stresses of each location are being correlated with each other [28].

The actual R_{ijkl} calculation involves a number of steps [18]. It should be noted that all overbars in the following sequence of equations represent time averages. The Favre averaged velocity field is defined as

$$\widetilde{u_i} = \frac{\overline{\rho u_i}}{\overline{\rho}}. \tag{3.9}$$

Once the Favre averaged velocity field is obtained, velocity fluctuations, u_i'', are then found using

$$u_i = \widetilde{u_i} + u_i''. \tag{3.10}$$

The Reynolds stress fluctuations, T_{ij}', are then

$$T_{ij}' = -(\rho u_i'' u_j'' - \overline{\rho u_i'' u_j''}). \tag{3.11}$$

Finally, the cross correlation is found by multiplying a Reynolds stress fluctuation term at a point by a Reynolds stress fluctuation term at a given time delay and spatial offset and then averaged in time. This process is shown as equation 3.12.

$$R_{ijkl} = \overline{T_{ij}'(\vec{x}, t) T_{kl}'(\vec{x} + \Delta, t + \tau)} \tag{3.12}$$

While it will be shown that this correlation calculation involves three passes through the simulated data, a one pass equation for the correlation calculation was also developed. This can be seen as equation A.1 in the Appendix.

3.3 Statistics of acoustic sources

3.3.1 Quasi-normality hypothesis

The quasi-normality hypothesis assumes that the variables of interest are independent and normally distributed. In the case of this research, it predicts that the components of velocity in the flow field are normally distributed. Quasi-normality is especially important to this research because it indicates that reduced-order acoustic source modeling is valid for the flow field. Many acoustic source models assume quasi-normality.

Millionshchikov's identity is used to test the quasi-normality hypothesis. With this identity, one can see if fourth order velocity correlations are correlated with second order velocity correlations via a scaling factor that is accurate for normal Gaussian probability distributions.

In order to test for the quasi-normality hypothesis using Millionshchikov's identity, one must look at the cross correlation terms with basic time averaging and no densities included so as to analyze only four variables for the correlations. The importance of this will be shown later. Equations 3.13, 3.14, and 3.15 show the process behind the simplified cross correlation calculation.

$$u_i = \overline{u_i} + u_i' \tag{3.13}$$

$$\hat{T}_{ij} = \overline{u_i' u_j'} \tag{3.14}$$

$$\hat{R}_{ijkl} = \overline{(u_i' u_j' - \overline{u_i' u_j'})(u_k' u_l' - \overline{u_k' u_l'})} \tag{3.15}$$

Millionshchikov's identity can now be shown. If one expands equation 3.15, equation 3.16 is the result.

$$\hat{R}_{ijkl} = \overline{u_i' u_j' u_k' u_l'} - \overline{u_i' u_j'} \cdot \overline{u_k' u_l'} \tag{3.16}$$

Equation 3.17 illustrates an identity that is valid for any four independent and normally distributed variables [29].

$$\overline{u_i' u_j' u_k' u_l'} = \overline{u_i' u_j'} \cdot \overline{u_k' u_l'} + \overline{u_i' u_k'} \cdot \overline{u_j' u_l'} + \overline{u_i' u_l'} \cdot \overline{u_j' u_k'} \tag{3.17}$$

If the right hand side of equation 3.17 is inserted in place of the first term on the right hand side of equation 3.16, the equation then becomes equation 3.18.

$$\hat{R}_{ijkl} = \left[\overline{u_i' u_j'} \cdot \overline{u_k' u_l'} + \overline{u_i' u_k'} \cdot \overline{u_j' u_l'} + \overline{u_i' u_l'} \cdot \overline{u_j' u_k'}\right] - \overline{u_i' u_j'} \cdot \overline{u_k' u_l'} \tag{3.18}$$

Simplifying, the expression then becomes equation 3.19.

$$\hat{R}_{ijkl} = \overline{u_i' u_k'} \cdot \overline{u_j' u_l'} + \overline{u_i' u_l'} \cdot \overline{u_j' u_k'} \tag{3.19}$$

For determining the scaling factor associated with testing the quasi-normality hypothesis, $\hat{R}_{1111}$ is analyzed. If single point statistics are being considered, meaning no spatial offsets being analyzed, equation 3.19 becomes the expression illustrated by equation 3.20.

$$\hat{R}_{1111} = 2\left[\overline{u_1'^2}\right]^2 = 2\hat{T}_{11}^2 \tag{3.20}$$

However, if spatial offsets are being considered, the final equation becomes equation 3.21.

$$\hat{R}_{1111} = 2\left[\overline{u_1'(u_1')'}\right]^2 \tag{3.21}$$

The additional apostrophe in the $(u_1')'$ expression indicates that it is the velocity fluctuation at the spatial offset. This derivation implies that the scaling factor for testing the quasi-normality hypothesis should theoretically be 2. Millionshchikov's identity is

now shown as equation 3.22, where (α) is the calculated scaling factor and single point statistics are assumed.

$$\hat{R}_{1111} = \alpha \hat{T}_{11}^2 \tag{3.22}$$

Once the scaling factor is found by minimizing the error between both sides of equation 3.22, it is used for equations 3.23 and 3.24. The goal of this process is to test the quasi-normality hypothesis by using the same scaling factor and seeing if the statistics line up on both sides of the equations. This is done for a spatial offset analysis as well. If the second and fourth order statistics line up with each other, the flow field is completely quasi-normal in all directions. This logic is also assumed by the MGBK code used for jet noise prediction at NASA [30].

$$\hat{R}_{2222} = \alpha \hat{T}_{22}^2 \tag{3.23}$$

$$\hat{R}_{3333} = \alpha \hat{T}_{33}^2 \tag{3.24}$$

3.3.2 Statistical axisymmetry

R_{ijkl} contains two invariants, R_{iikk} and R_{ikik}. For the purposes of testing statistical axisymmetry, the amplitudes of these two quadratic forms are analyzed. It should also be noted that these correlation values are calculated with the density field and Favre averaging, unlike the quasi-normality study. R_{iikk} represents the diagonal quadratic form because only diagonal terms in R_{ijkl} appear. The R_{ikik} term represents the Hermitian quadratic form because of the pair symmetries in R_{ijkl}. The expansions of R_{ikik} and R_{iikk} are shown as equations 3.25 and 3.26 [28].

$$R_{ikik} = R_{1111} + R_{2222} + R_{3333} + 2[R_{1212} + R_{1313} + R_{2323}] \tag{3.25}$$

$$R_{iikk} = R_{1111} + R_{2222} + R_{3333} + 2[R_{1122} + R_{2233} + R_{1133}] \tag{3.26}$$

Local statistical axisymmetry indicates that fluctuations in the transverse directions are equal to each other as well as the cross correlation tensor is axisymmetric [28]. Statistical axisymmetry is important because if a flow field is statistically axisymmetric, it can reduce the order of an accurate and needed acoustic source model. The assumption of statistical axisymmetry indicates a few identities as well. These identities are $R_{2222} = R_{3333}$, $R_{1122} = R_{1133}$, and $R_{1212} = R_{1313}$ [28]. These identities were used to obtain equations 3.27 and 3.28 [28].

$$\frac{R_{ikik}}{R_{1111}} = 1 + \frac{2}{R_{1111}}[R_{2222} + 2R_{1212} + R_{2323}] \tag{3.27}$$

$$\frac{R_{iikk}}{R_{1111}} = 1 + \frac{4}{R_{1111}}[R_{2222} - R_{2323} + R_{1122}] \tag{3.28}$$

For testing statistical axisymmetry, either equation can be evaluated on both sides. Then, the left and right sides of the equation are compared to each other to see how close they are in value. A small error residual between both sides of the equation indicates local statistical axisymmetry.

3.4 Acoustic source models

Accurate acoustic source models together with an appropriate adjoint Green's function provide a low fidelity method for jet noise prediction [18]. There has been some success with these models for round jets, but it was unclear whether similar success with these models could be achieved with complex jets.

The following sections will describe the equations that represent the models. For all source models used in this thesis, only axial spatial separations, Δ_1, were considered.

Also, with regard to the source model formulas, τ represents time delays, $\widetilde{\upsilon_1}$ represents convection velocity, l_1 is an axial length scale fit, τ_s is a time scale fit, and A_{ijkl} is an amplitude fit.

3.4.1 Gaussian model

A Gaussian model fit is a simple model that has had reasonable success [19]. However, a Gaussian model cannot model the negative loops of the cross correlation terms caused by large coherent structures in the flow field [17]. Also, it cannot model the cusp behavior of the correlation values at zero spatial separation. Equation 3.29 is the model equation that is used for representing the Gaussian model in this thesis [19]. It has been modified to only include axial spatial separations.

$$R_{ijkl}(\vec{x}, \Delta_1, \tau) = A_{ijkl} exp\left[-\frac{\Delta_1}{\widetilde{\upsilon_1}\tau_s} - \ln 2\left(\frac{(\Delta_1 - \widetilde{\upsilon_1}\tau)^2}{l_1^2}\right)\right] \tag{3.29}$$

3.4.2 Moving-frame model

Goldstein & Leib developed the moving-frame model and were able to calculate reasonably good jet noise predictions for a cold supersonic axisymmetric jet [20]. The model assumes both quasi-normality and statistical axisymmetry for the flow field. Although not done in this thesis, the model can be modified to account for the negative loops of the correlation values at large time delays. Equation 3.30 shows the equation that is used to represent the moving-frame model, modified to only include axial spatial separations [20].

$$R_{ijkl}(\vec{x}, \Delta_1, \tau) = A_{ijkl} exp\left[-\left(\left(\frac{(\Delta_1 - \widetilde{\upsilon_1}\tau)}{l_1}\right)^2 + \left(\frac{\tau}{\tau_s}\right)^2\right)^{0.5}\right] \tag{3.30}$$

Taylor's hypothesis states that turbulence is almost in a frozen state and decays very slowly with time advancement when observed in an appropriate moving-reference frame. The moving-frame model uses Taylor's hypothesis to treat fine-scale turbulence as approximately frozen. In other words, the decay rate of the turbulence is slow compared to the background convection [21].

3.4.3 Fixed-frame model

Leib & Goldstein developed a fixed-frame model to predict acoustic source behavior [21]. The model assumes statistical axisymmetry, but unlike the moving-frame model, it does not assume quasi-normality for the flow field. They found that while the moving-frame model results appeared to be more in line with the original Taylor hypothesis, the fixed-frame model provided slightly better results for a cold supersonic axisymmetric jet. Like the moving-frame model, the fixed-frame model, while not done in this thesis, can be modified to account for the negative loops of the correlation values at large time delays. Equation 3.31 represents the fixed-frame model, again modified to only include axial spatial separations [21].

$$R_{ijkl}(\vec{x}, \Delta_1, \tau) = A_{ijkl} exp \left[- \left(\left(\frac{(\Delta_1 - \widetilde{v_1}\tau)}{l_0} \right)^2 + \left(\frac{\Delta_1}{l_1} \right)^2 \right)^{0.5} \right] \tag{3.31}$$

3.4.4 Modified-distance model

The modified-distance model has had success in previous papers as well [23; 24]. It is an exponential function of a space-time modified distance. However, in the interest of being thorough, the model has been found to decay too quickly at large time delays [24]. Equation 3.32 represents the model equation that is used for the modified-distance model [23]. The b_1 term represents the peak-decay shape regulator fit.

$$R_{ijkl}(\vec{x},\Delta_1,\tau) = A_{ijkl}exp\left[-\left(\left(\frac{\tau-\frac{\Delta_1}{\widetilde{v_1}}}{\tau_s}\right)^2+\left(\frac{|\Delta_1|}{l_1}\right)^{b_1}\right)^{0.5}\right] \tag{3.32}$$

3.5 Theory of large scale coherent motions

While fine-scale turbulence is definitely a primary component of turbulent mixing noise, larger coherent motions in the turbulent flow field are also a significant factor particularly in the downstream regions [10]. In fact, turbulent flows are dominated by these moving spatially coherent vortical structures known as coherent motions [31]. According to Robinson, a coherent motion is "a three-dimensional region of the flow over which at least one fundamental flow variable...exhibits significant correlation with itself or with another variable over a range of space and/or time that is significantly larger than the smallest local scales of the flow" [32]. These coherent motions are nearly periodic in the flow field and exist due to non-random behavior in the flow. In other words, coherent structures are caused by instabilities in the flow field itself. Velocity and pressure correlations are often used to identify large coherent structures [32].

In order to see the coherent motions in the flow, pressure is calculated and Fourier transformed in time. Pressure was not explicitly given in the data outputted from Nichols et al.'s study [2], but the calculation for it using available data is very simple. It can be found in the Appendix of this thesis. Equation 3.33 represents an equation for pressure that can directly be solved using the outputted data from the study done by Nichols et al. [2]. A little more rearranging can be done that directly shows the outputted data of ρ, ρu_1, ρu_2, ρu_3, and ρE. Equation 3.34 is the result.

$$P = (\gamma-1)[\rho E - \frac{1}{2}\rho V^2] \tag{3.33}$$

$$P = (\gamma - 1)[(\rho E) - \frac{1}{2(\rho)}\left((\rho u_1)^2 + (\rho u_2)^2 + (\rho u_3)^2\right)] \tag{3.34}$$

3.6 Computer codes

The following sections will describe every detail of the coding process performed in this thesis.

3.6.1 Data extraction (alternating digital tree algorithm - ADT)

The high-fidelity data set generated by the rectangular chevron jet simulation totaled 200 Tb in size [2]. These data are stored on robotic tape silos at the Argonne National Laboratory and are too large to fit entirely on high-speed disks accessible to processing elements. Therefore, to facilitate the statistical analysis routines developed for this thesis, the high-fidelity data set was first decimated spatially to a uniformly spaced Cartesian mesh. It is important to note that this does not sacrifice accuracy since the data were generated by a high fidelity simulation. The decimated data totaled 1 Tb in size.

The data were extracted using a basic alternating digital tree algorithm (ADT). The ADT is an efficient solution of the geometric searching problem by offering the opportunity of adding or removing points and optimally searching for points inside a region of interest [3]. Geometric searching is the process of finding the points of a set of n points which reside inside a region of an N dimensional space [3]. For this thesis, the geometric searching was gathering a uniform Cartesian grid inside the flow field with 512x65x65 points corresponding to (x,y,z). The location of the statistical domain in the LES domain is shown as figure 3.1. The field shown is a snapshot in time for the axial velocity. Only the $z = 0$ plane is shown because it shows the maximum transverse spreading of the flow field. The reason for this is that the long sides of the rectangular nozzle are aligned

with the y axis. The actual dimensions of the extracted statistical domain from the LES domain are $5.5 \leq x \leq 35.5$ and $-5.0 \leq y, z \leq 5.0$. Since the established statistical domain is 512x65x65 points, this means that the Δx is roughly 0.0587, while Δy and Δz are 0.15625. Also, the dimensions of the statistical domain in multiples of the equivalent diameter, D_e, are $2.59D_e \leq x \leq 16.71D_e$ and $-2.35D_e \leq y, z \leq 2.35D_e$. This means that Δx is $0.028D_e$, and Δy and Δz are $0.074D_e$. It is important to note that in the simulation, the nozzle exit is not at the origin but rather at a value of $x = 4.74$, or $2.23D_e$. The statistical domain does not start at this location because of the chevrons extending past the nozzle exit. As one can see from figure 3.1, the statistical grid captures almost all of the transverse jet spreading. However, it does cut off axially where the LES domain continues to predict the speeds. The axial extent of the statistical domain was chosen to capture the primary sound-producing regions of the jet, i.e. the high turbulent areas. Also, while the extracted statistical grid is too coarse to accurately model the shear layer coming out of the nozzle, it ultimately does not matter since the goal of this thesis is to accurately model the primary acoustic sources in the flow. The side jets are much more important in this aspect, and the extracted grid is refined enough to accurately model the side jets.

The non-sequential data structure used in the application of the ADT is the binary tree. The binary tree has been the basis for many searching algorithms, not just the ADT [3]. Tree structures were initially constructed for the purpose of systematically storing data in such a way that allows quick access to stored information and also quick addition and removal of data [3]. This type of data storage requires non-sequential locations in the computer's memory. With this in mind, every data item is extended by two integer values, the left and right links, and stored in a node of the binary tree. Every link can contain a zero or the memory address of another node. Therefore, when analyzing one node of the tree, one can reach at most two other nodes. This is the most basic idea of a binary tree

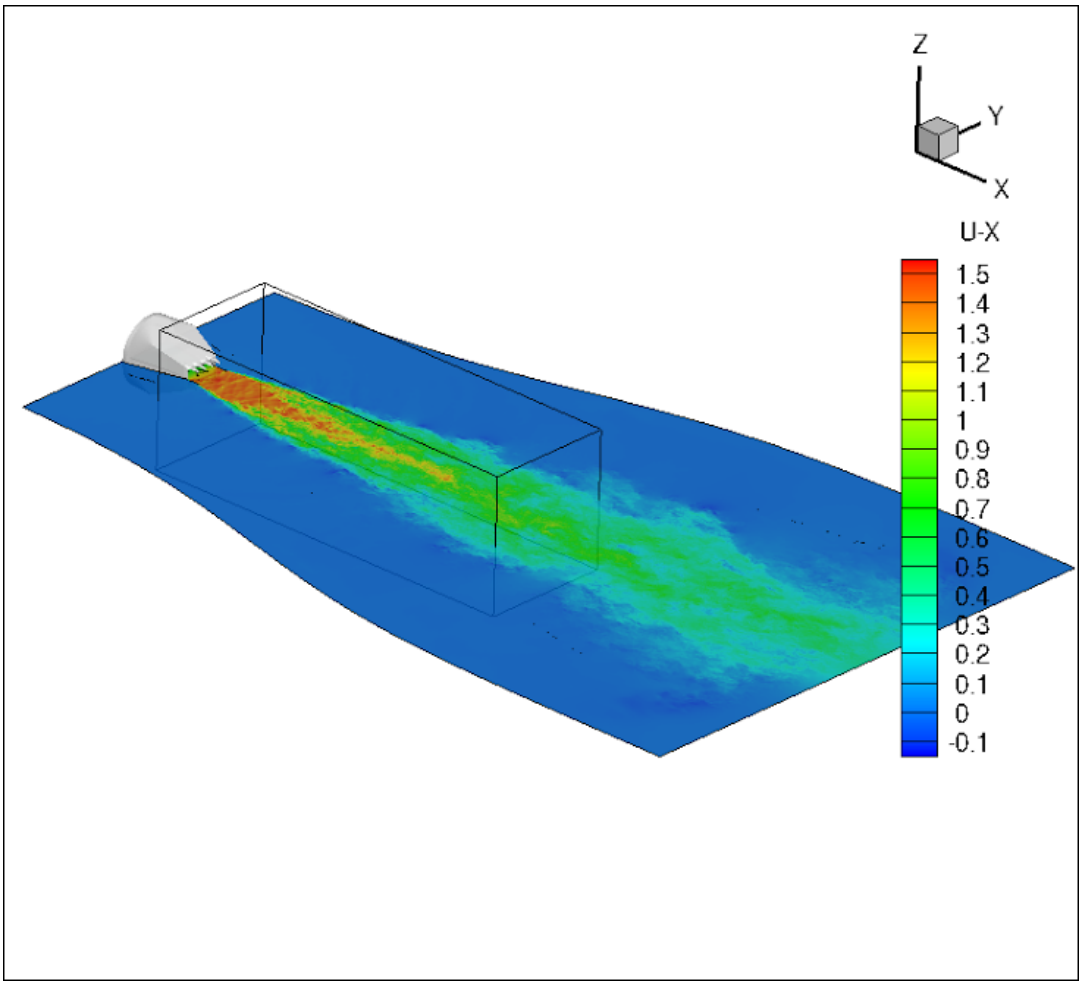

Figure 3.1: Statistical domain (rectangular prism) extracted from the LES domain.

[3]. Figure 3.2 shows a simple diagram of a binary tree.

The alternating digital tree algorithm essentially stores data in a binary tree where its structure models the positions of the points in the desired space region. This makes the process less computationally expensive. In other words, the alternating digital tree is a binary tree in which n points are stored in a specific geometrical pattern where each node in the tree contains two sons [3]. The basic idea is that a "bisection process divides a given region into two smaller sub-regions" [3]. As an example, assume an N dimensional space with coordinate axes of $[x_1, x_2, ..., x_N]$ that all vary within the interval of [0 1). The region starts by getting bisected across the x_1 axis. The data contained in the sub-region that represents $0 \leq x_1 < 0.5$ get assigned to the left son, while the data in the sub-region that represents $0.5 \leq x_1 < 1$ get assigned to the right son. The process gets repeated for each axis [3].

In the case of extracting data from the analyzed flow field, the process followed the same ADT structure. The x axis was bisected so that data in the sub-region of $5.5 \leq x < 20.5$ got assigned to one son while the data in the sub-region of $20.5 \leq x \leq 35.5$ got assigned to another son. Similarly, the y and z axes were bisected so that data in the sub-regions of $-5.0 \leq y, z < 0.0$ got assigned to one son while the data in the sub-regions of $0.0 \leq y, z \leq 5.0$ got assigned to another son. It should be noted that this process was only formed once at the beginning of the extraction, not for every time step. After the search completed the first time, addresses were saved and used for subsequent steps.

3.6.2 Three pass routine for statistical calculations

The following information will be using the calculation of R_{1111} as an example.

As stated earlier, the calculation of the correlation terms involved a three pass system. The first pass was generated to calculate the Favre averaged axial velocity field. The extracted data containing the ρu and ρ fields was read into a C file. Then, the code ran

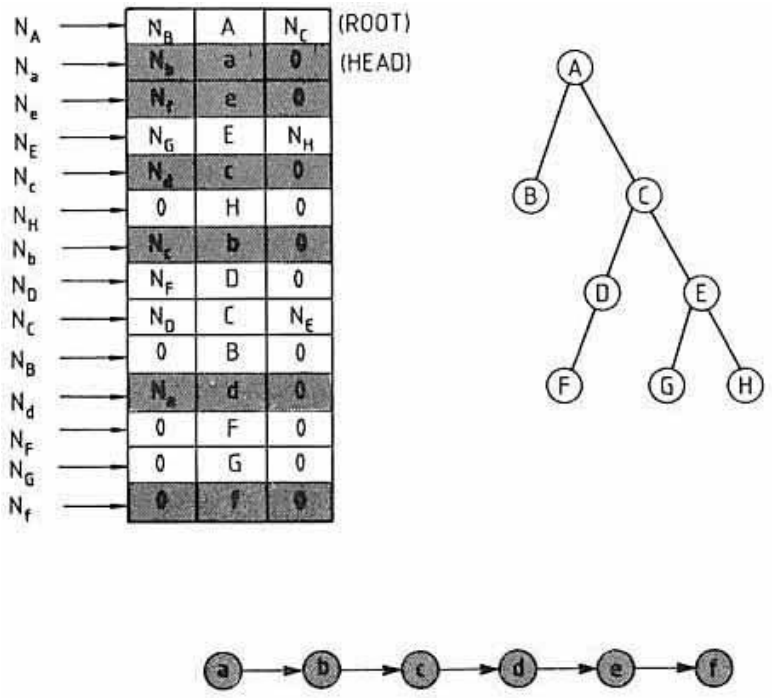

Figure 3.2: A simple diagram of a binary tree (adapted from Bonet et al. [3]).

through every time snapshot, 7340 in total, of the data and took a time average of both fields. The Favre averaged velocity field calculation was then performed for all points in the flow field. The results were stored in a one dimensional array and reshaped into a three dimensional array in MATLAB when plotting was necessary.

The second pass was generated to calculate the mean Reynolds stress field. To do this, the Favre averaged axial velocity field was read into a C file as well as the ρu and ρ fields. Then, the code ran through every time snapshot and performed a number of essential calculations at each snapshot. First, an axial velocity value was calculated using the ρ and ρu fields at every point. Then, the velocity values were used along with the Favre averaged velocity field to obtain the axial velocity fluctuation values at every point. The axial velocity fluctuation field was then multiplied by itself and the ρ field to obtain the Reynolds stress field. This process repeated itself for every snapshot while also simultaneously time averaging the Reynolds stress field to obtain the mean Reynolds stress field. The results were stored in a one dimensional array and reshaped into a three dimensional array in MATLAB when plotting was required.

The third pass was generated to calculate R_{1111}. To accomplish this goal, the results from pass 1 and 2 were read into a C file as well as the ρu and ρ fields. Then, variations of the third pass were established.

If single point statistics were being analyzed, the setup of the cross correlation calculation was the same as pass 1 and 2. The code ran through every snapshot and performed a number of essential calculations at each snapshot. First, the velocity at every point was calculated using the ρ and ρu fields. Then, the velocity values were used along with the Favre averaged velocity field to obtain the velocity fluctuation field at every point. Then, the velocity fluctuation field was multiplied by itself and the ρ field to obtain the instantaneous Reynolds stress at every point. Then, the averaged Reynolds stress field was used to subtract from the instantaneous Reynolds stress field to obtain the fluctuating Reynolds

stress at every point. Finally, the fluctuating Reynolds stress was multiplied by itself at every point. This process repeated itself for every snapshot while also simultaneously time averaging the product of the two fluctuating Reynolds stress values to obtain R_{1111}. The results were stored in a one dimensional array and reshaped into a three dimensional array in MATLAB.

If spatial offsets and time delays were involved in the correlation calculations, the analyzed flow field was shrunk down to 503x65x65 points instead of the full flow field of 512x65x65 points. This allowed for each point in the analyzed flow field to have spatial separations up to 9 points downstream and including 0 spatial separation. Also, 0-49 time delays were analyzed. One time delay increment in this study is equal to 0.1 due to time snapshots being outputted from the chevron jet simulation every 100 time steps [2]. All in all, this means that up to 500 calculated values were stored for every point in the 503x65x65 mesh for the correlation calculations. The final results were once again stored as a one dimensional array and reshaped into a five dimensional array in MATLAB.

Processing statistical data was significantly slowed down by having to read in the flow field data for the calculations. The amount of time it took for the computer to go from memory to disk drive was much longer than the actual time it took to perform the statistical calculations.

3.6.3 Application of symmetry to statistics

Most of the results for statistical calculations are confined to the $y = 0$ plane of the flow field. This was thought to be the most interesting plane for visual analysis due to the chevron effect being prominent. However, there are some $z = 0$ plane and full three dimensional flow fields spread throughout the thesis. When planes were created, there was almost always two-way averaging involved. This essentially allowed for better resolution by doubling the amount of usable data. This was done by averaging the top half of the

plane with the bottom half of the plane. This works if the instantaneous fluctuations are statistically uncorrelated, which for a turbulent flow means that they are sufficiently spatially separated. The flow must also be statistically symmetric. When three dimensional plots were created, four-way averaging was involved. This effectively quadrupled the data set. There were a few cases where averaging was not done. For instance, when testing local statistical axisymmetry, averaging was not done to preserve the local nature of the test. Also, when analyzing large turbulent structures in the flow, averaging was left out to once again look at local behavior.

3.6.4 Histogram creation

Generating the histogram plots for analyzing single point velocity probability distribution functions was a fairly easy process. After determining points of interest, a C file was generated that tracked the axial velocity at these points. Once the axial velocity was outputted as a function of time, it was read into MATLAB. The histogram function was then used while specifying 50 total bins to be used for each point. Each bin represents a range of velocity values. Once the histogram plots were generated, a basic Gaussian curve was fit to both data sets. The curve was found by finding the mean and standard deviation of the data sets and using that data to generate basic Gaussian curves. The equation for the Gaussian fit is shown as equation 3.35.

$$y(x') = \frac{1}{\sigma_{u_1}^2\sqrt{2\pi}} exp\left[-\frac{(x' - \bar{u_1})^2}{2\sigma_{u_1}^2}\right] \tag{3.35}$$

3.6.5 Power spectrum calculation

The points analyzed for the histogram creation were also used for analyzing power spectra and turbulence. Power spectra are directly related to acoustic sources, as the power spectrum of a point is the Fourier-cosine-transform pair of its R_{ijkl} auto-correlation curve

[33]. The power spectra were calculated in MATLAB. Once the velocity was tracked in time for both points using the C file that was created for the histogram plots, the data were read into MATLAB. The Fast Fourier Transform function built into MATLAB was then used to calculate the Fourier coefficient vs. frequency spectrum data for both points. Then, to calculate the power spectra, the Fourier coefficients were multiplied by their complex conjugates using the "conj()" function in MATLAB.

The next step in the process was to calculate an average line of the power spectrum data. This was done in MATLAB as well by using a routine that essentially increments the data and takes averages of the increments. The results are then outputted in a $10log_{10}$ scale.

3.6.6 Finding the scaling factor for testing the quasi-normality hypothesis

As stated earlier, the scaling factor for Millionshchikov's identity was calculated and not assumed to be 2. The process of finding the scaling factor was a very simplified yet effective process. MATLAB was used to minimize the $\|error\|_2$ between the cross correlation term, $\hat{R}_{1111}$, and the square of the mean Reynolds stress times the scaling factor, $\alpha\hat{T}_{11}^2$. From theory, the expected scaling factor should be about 2. With this in mind, a basic MATLAB script was written that looped scaling factor values from 1 to 3 in 0.01 increments. For every scaling factor value, $\|error\|_2$ was calculated for the entire three dimensional domain of the flow field. The results were then plotted in order to visually see what scaling factor corresponded to the minimum of $\|error\|_2$. This same process was also done for the entire three dimensional domain with spatial offsets.

3.6.7 Computational method for acoustic source models

The computational process behind fitting the acoustic source models to the cross correlation data was all done in MATLAB. Function files were created for each model containing the corresponding model equations. When necessary, the equations were scaled to quickly find the best fit to the cross correlation data. In particular, the amplitude and time scale fits were scaled due to the fact that the amplitude fits were found to be typically much smaller than the other coefficient fits, while the time scale fits were found to be slightly larger than the other fits.

After the function files were created for each model, separate files were then made that actually fit the model to the the cross correlation data. The files utilized the least squares curve fit function provided in MATLAB. The file looped through every desired point of interest in the flow and fit the desired model equation to the data. Tolerances pertaining to the least squares curve fit function were lowered until there was no apparent change in the solutions for differing initial guesses. The output of the files were coefficient fit fields for the flow as well as residual error fields between the models and calculated R_{ijkl} values.

3.6.8 The computational process behind finding large scale coherent motions

FFTW (Fastest Fourier Transform in the West) was used to calculate the pressure Fourier coefficients of the center plane [34]. Once again, the full 7340 snapshots were used along with equation 3.34 to calculate the pressure in time for every point in the center plane. A temporal FFT of the pressure was then taken for every point. Since an FFT of real data is conjugate symmetric, only the positive frequency Fourier coefficients were stored, not the negative frequency values. The final data was then stored in a one dimensional array, read into MATLAB, and reshaped as an array of dimensions 3670x512x65. Then, in order to determine the dominant frequencies, the data was plotted for various low frequencies. The

motivation for looking solely at low frequencies is that large scale coherent motions are linked to low frequency turbulent mixing noise [9]. A general frequency range was then determined based on the strength of the Fourier coefficients. This range was determined to be around 1-100 frequency values.

Once the dominant frequencies were established, another C file was generated. This time, however, the entire three dimensional flow field was cycled through the code for the purpose of calculating pressure Fourier coefficients. The simulation had to be broken up into seven different parts due to the limited capacity of the memory on the desktop that was used. Also, once the FFT was performed for a given point, only the dominant frequency region was saved. Once all seven output files were generated, they were concatenated together and read into MATLAB.

Chapter 4

Single point statistics

4.1 Velocity statistics (first order)

The importance of the Favre averaged axial velocity field is that it is used to find Reynolds stresses in the axial direction which are then used to find the correlation R_{1111}. For axisymmetric jets, R_{1111} is known to contribute the most to the sound [18]. Figure 4.1(a) shows contours of the Favre averaged axial velocity, $\widetilde{u}_1$, on the $y = 0$ plane. The field is physically accurate. Shock cells can be seen at the center of the flow field. Also, the highest average speeds reside in the center of the field and gradually decay to zero near the edges of the shear layer. For a full three dimensional view of the mean velocity, figure 4.2(a) represents an isosurface of $\widetilde{u}_1$ = 0.75. A close up view of the flow exiting the nozzle is included as figure 4.2(b) to show the chevron effect. Figure 4.3 is also included as a three view system of the mean velocity using the isosurface quantity 0.75. When analyzing figure 4.3(b), side jets caused by the chevrons can clearly be seen. Also, when analyzing figure 4.3(a), one can see the side jets caused by the rectangular shape of the nozzle.

As an additional study, since the more basic $\hat{R}_{ijkl}$ was calculated and used for testing the quasi-normality hypothesis, it was necessary to see how various statistics changed

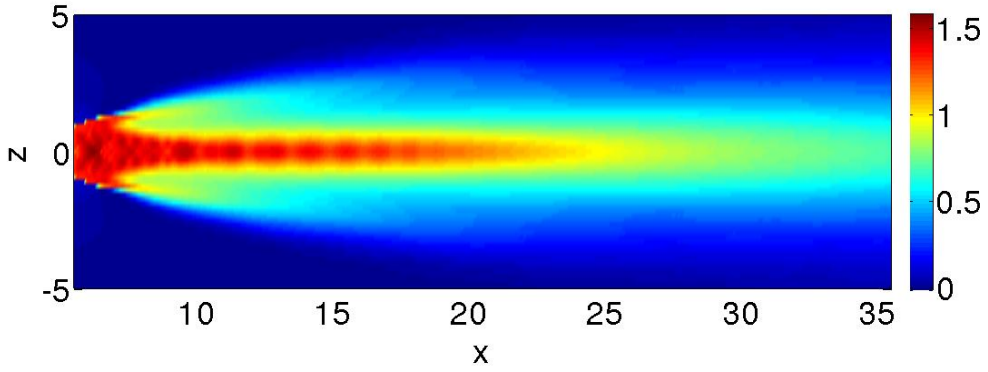

(a) The Favre averaged axial velocity field, $\widetilde{u}_1$.

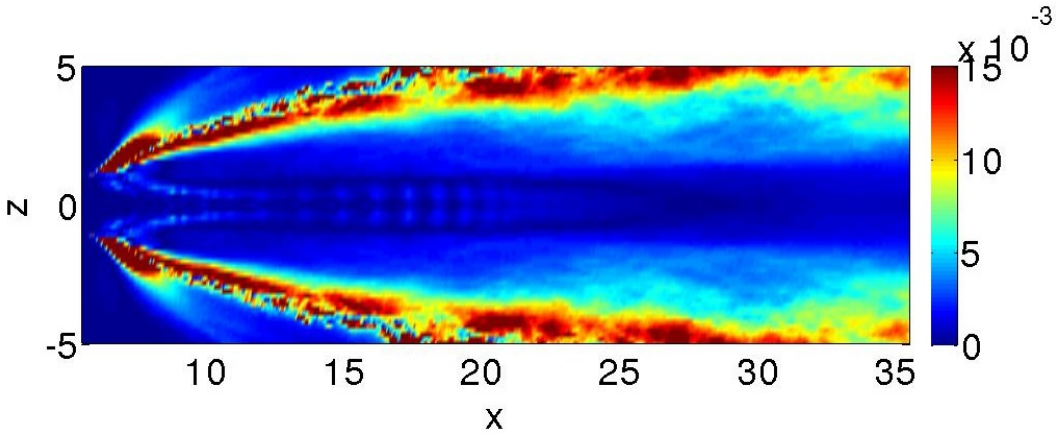

(b) Contours of the residual between the Favre averaged and time averaged axial velocities, $\widetilde{u}_1$ and $\bar{u}_1$, respectively.

Figure 4.1: The Favre averaged axial velocity field, $\widetilde{u}_1$, and a comparison between the time averaged and Favre averaged axial velocities, $\bar{u}_1$ and $\widetilde{u}_1$, respectively ($y = 0$ plane).

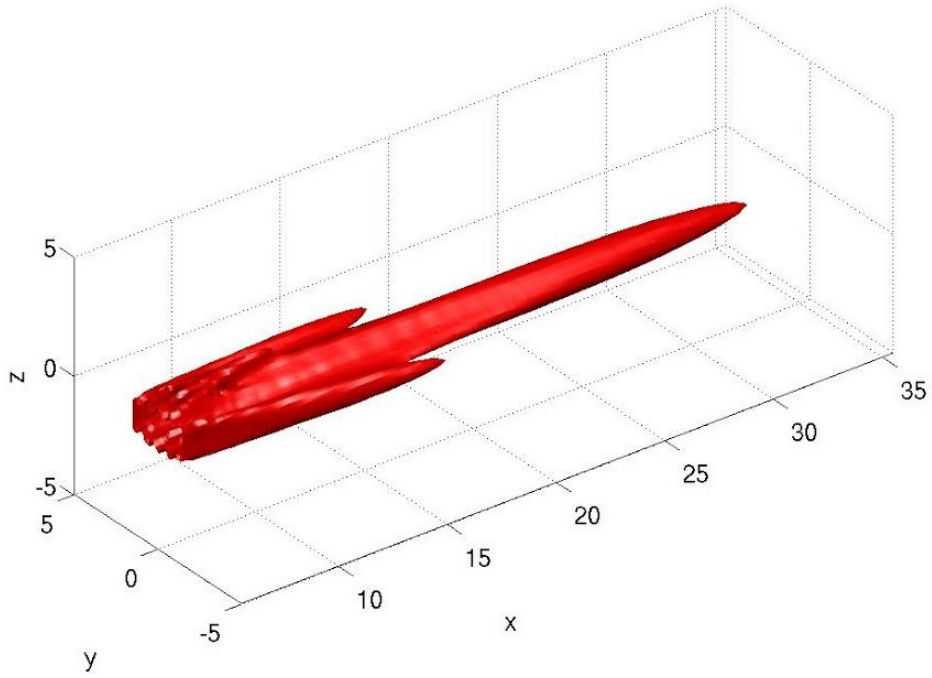

(a) 3D view.

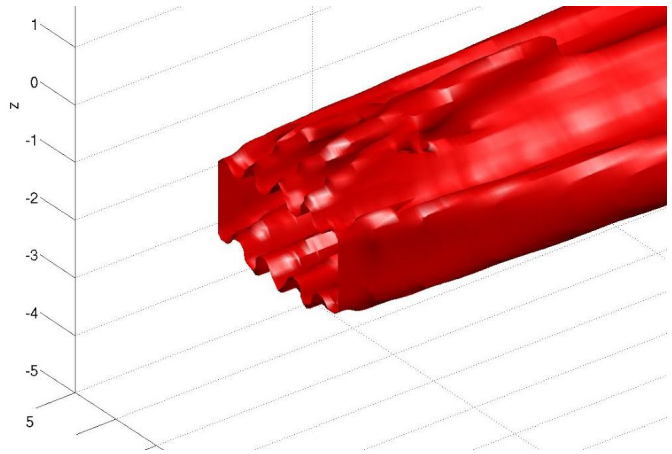

(b) Close up view of chevron effect.

Figure 4.2: A three dimensional view of the Favre averaged axial velocity field, $\widetilde{u}_1$, as well as a close up view of the chevron effect ($\widetilde{u}_1 = 0.75$).

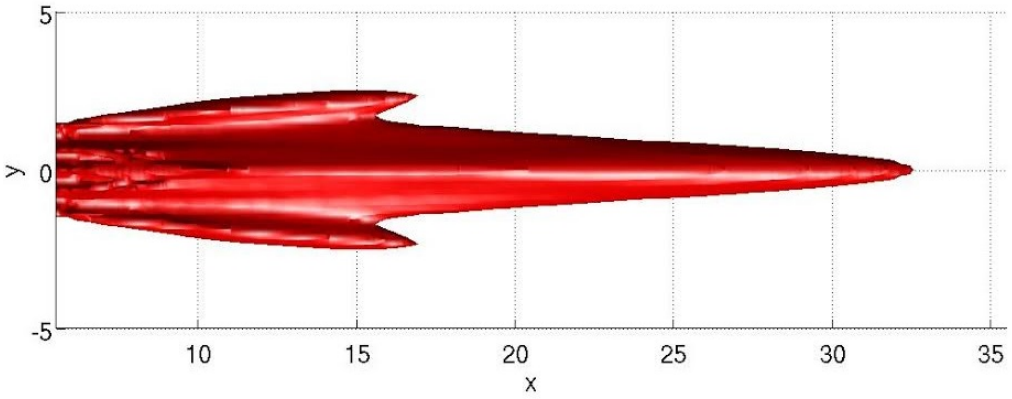

(a) XY view.

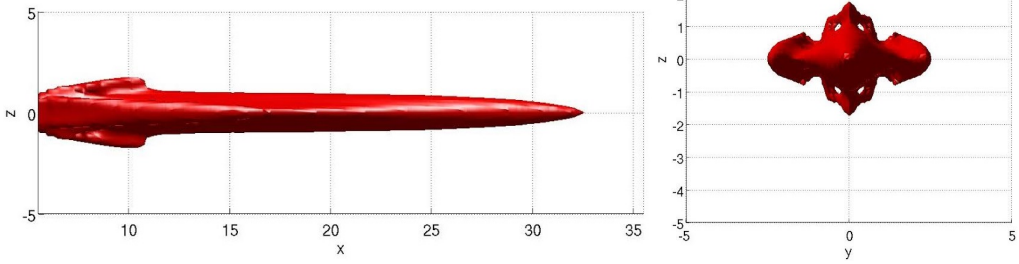

(b) XZ view.

(c) YZ view.

Figure 4.3: A three view system of the Favre averaged axial velocity field, $\widetilde{u}_1$ ($\widetilde{u}_1 = 0.75$).

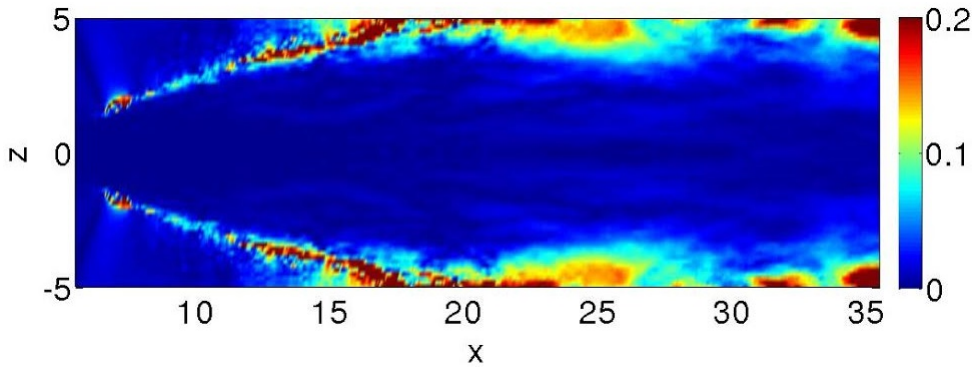

Figure 4.4: Relative change in the Favre averaged axial velocity field, $\widetilde{u}_1$, when using the available 7340 snapshots instead of 6000 snapshots.

when density was not included in the calculations. Figure 4.1(b) shows the residual between the basic time averaged and Favre averaged axial velocity fields, defined as

$$\frac{|\bar{u}_1 - \widetilde{u}_1|}{\widetilde{u}_1}. \tag{4.1}$$

The relative difference between the two velocity fields is minimal with errors peaking near the edges of the flow at about 1-1.5%. Therefore, it would appear that using a basic time average changes the 1^{st} order statistics of velocity averages very little compared to a Favre average.

4.1.1 Convergence test

To test the convergence of the statistics with respect to the sample size, $\widetilde{u}_1$ was computed using only 6000 snapshots in addition to the full set of 7340 snapshots. Then, a calculation was done to see how much the solution changed when the full 7340 snapshots were used. This way, an idea could be obtained on how much the solution may change if more time snapshots were theoretically available. This process shows where the flow statistics can be trusted to be accurate. Figure 4.4 shows this process for $\widetilde{u}_1$. The equation for the

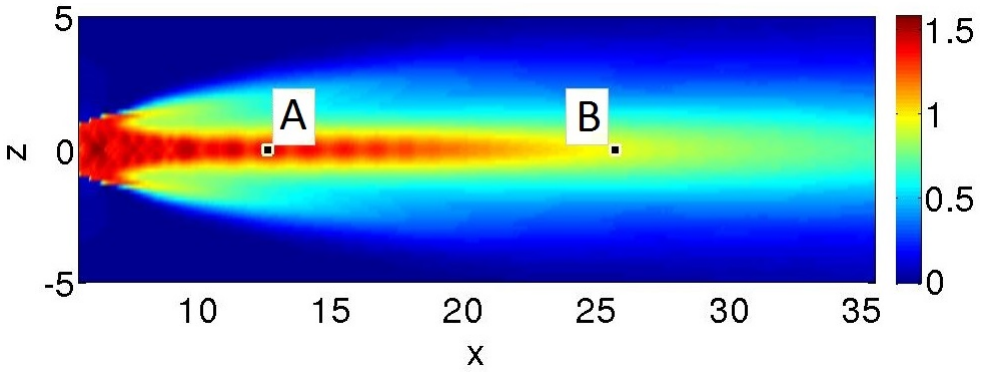

Figure 4.5: Selected points in the flow field for various statistical calculations ($y = 0$ plane).

convergence test is shown as equation 4.2.

$$\left| \frac{\widetilde{u}_1(7340 snapshots) - \widetilde{u}_1(6000 snapshots)}{\widetilde{u}_1(6000 snapshots)} \right| \tag{4.2}$$

It appears that the $\widetilde{u}_1$ field can be trusted everywhere except at the edges of the flow field. Otherwise, within the flow field, the solution appears to change at most 5%, particularly in the downstream regions. Therefore, it can be assumed that additional snapshots later in time would not change the $\widetilde{u}_1$ field by more than 5%. It should be noted that this particular relative measurement highlights errors at the edges of the jet since $\widetilde{u}_1$ is small at these locations. This applies to the second and fourth order statistics as well.

4.2 Turbulence statistics (second order)

Figure 4.5 shows two points in the $y = 0$ plane that were analyzed for their axial velocity power spectra. There is a point upstream (Point A) at coordinates of **(12.6,0,0)**. There is also a point downstream (Point B) at coordinates of **(25.7,0,0)**. Figure 4.6(a) shows the non-normalized axial velocity power spectrum of Point A. The non-normalized aspect of

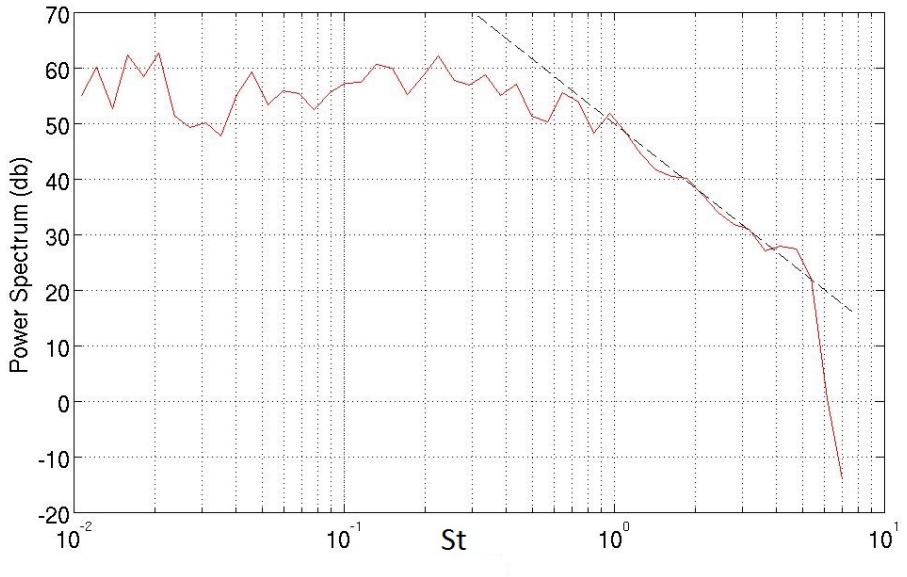

(a) Point A (from figure 4.5).

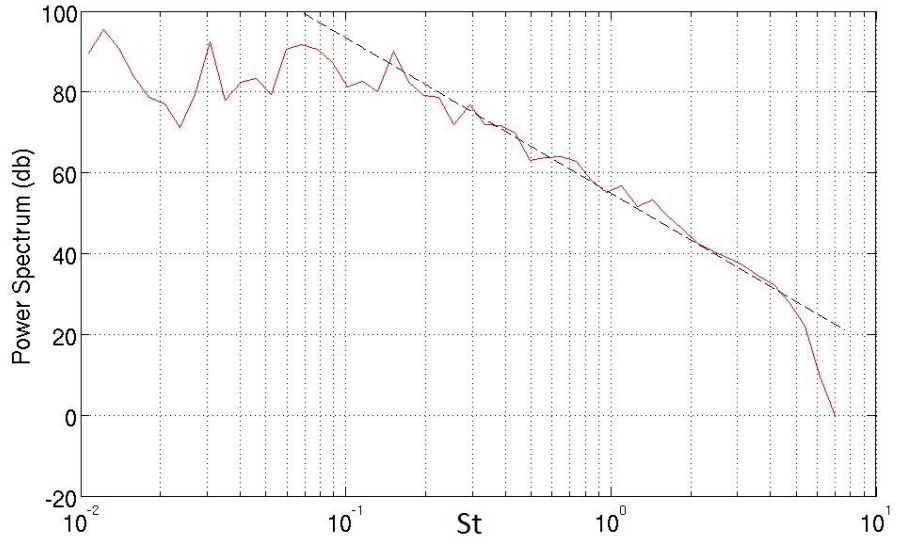

(b) Point B (from figure 4.5).

Figure 4.6: Non-normalized axial velocity power spectra of two chosen points in the flow field.

the plot means that the power spectrum was not divided by the square of the velocity sample size after the FFT was performed. The solid line represents the power spectrum, found by averaging the full power spectrum data using a frequency binning technique. Then, to determine if the flow field simulations represented turbulence accurately, Kolmogorov's $\frac{-5}{3}$ law was used [27]. As one can see from figure 4.6(a), the dashed line represents Kolmogorov's law for the purposes of seeing if the energy cascade of the power spectrum adheres to the slope of the dashed line. The dashed line does appear to adhere to the power spectrum over a given frequency range. Also, one can see the effect of the grid resolution in figure 4.6(a). The power spectrum appears to drop off from the Kolmogorov slope at a certain frequency. This occurs because the flow simulation is an LES. An LES does not simulate all of the eddies in the flow. Therefore, the energy cascade drops off before it reaches the smallest eddies of the flow. If a direct numerical solution (DNS) had been performed, the simulated energy cascade would have fully adhered to the Kolmogorov slope until molecular viscosity caused the same drop-off.

Figure 4.6(b) shows the non-normalized power spectrum of Point B. This was done to see what the effect of larger time scales had on the power spectrum. We find that the velocity spectrum at Point B adheres closely to Kolmogorov's $\frac{-5}{3}$ law. It is interesting to note that the energy cascade appears to encompass more frequencies due to the energy peak occurring at a lower frequency. This is due to the larger time scales farther downstream. Grid resolution once again plays a role, as one can see the drop off from the Kolmogorov slope. The grid resolutions at both Point A and B appear to be about the same, as the power spectrum drop off for both points appears to occur at about the same frequency.

With regard to Reynolds stresses, figures 4.7(a), 4.10, and 4.11 show $\widetilde{T}_{11}$, $\widetilde{T}_{22}$, and $\widetilde{T}_{33}$ respectively for the $y = 0$ plane. The auto-correlations of the fluctuations about these Reynolds stresses contribute the most to the sound [35]. When analyzing these

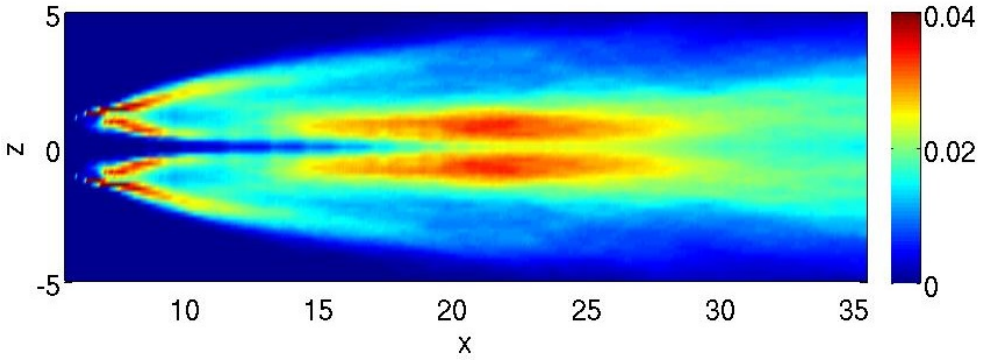

(a) $\widetilde{T}_{11}$ component of the mean Reynolds stress.

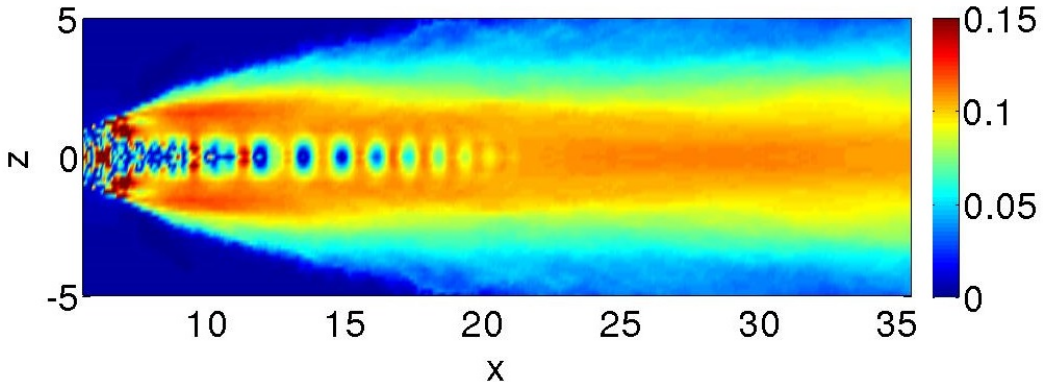

(b) Contours of the residual between the Favre averaged and time averaged mean Reynolds stress, $\widetilde{T}_{11}$ and $\hat{T}_{11}$, respectively.

Figure 4.7: $\widetilde{T}_{11}$ component of the mean Reynolds stress and a comparison between the time averaged and Favre averaged mean Reynolds stress, $\hat{T}_{11}$ and $\widetilde{T}_{11}$, respectively ($y = 0$ plane).

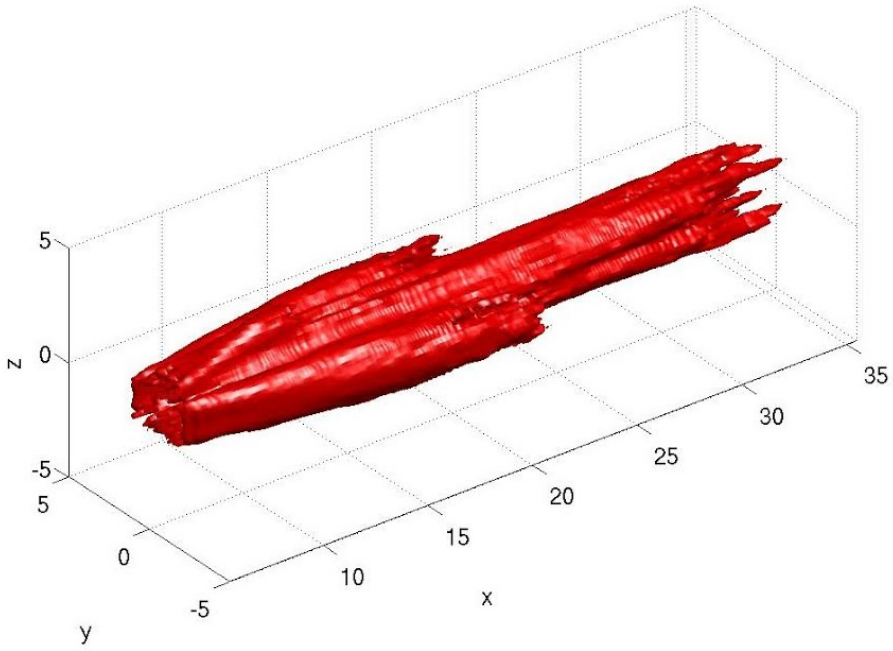

Figure 4.8: A three dimensional view of the $\widetilde{T}_{11}$ mean Reynolds stress component ($\widetilde{T}_{11} = 0.02$).

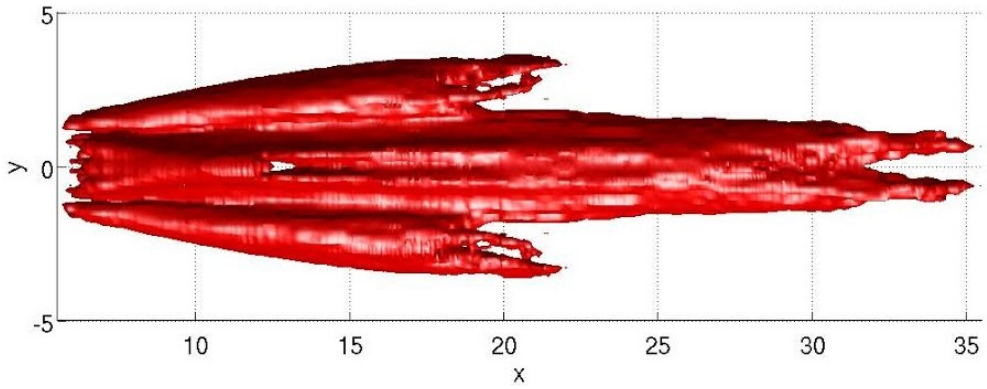

(a) XY view.

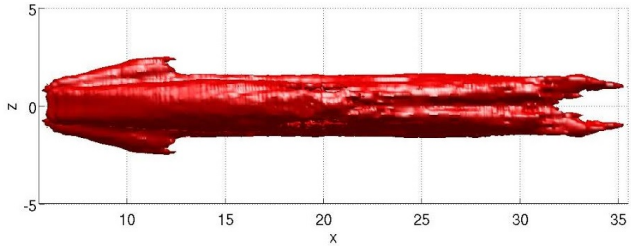

(b) XZ view.

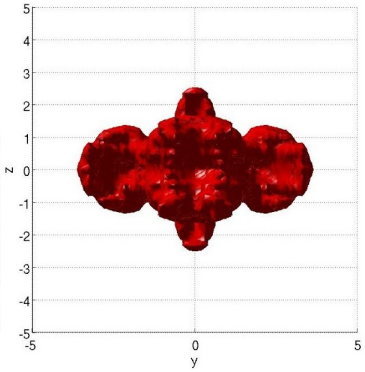

(c) YZ view.

Figure 4.9: A three view system of the $\widetilde{T}_{11}$ mean Reynolds stress component ($\widetilde{T}_{11} = 0.02$).

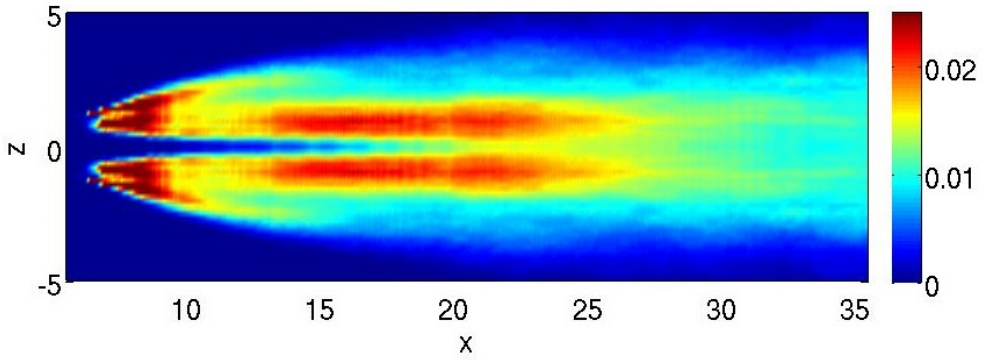

Figure 4.10: $\widetilde{T}_{22}$ component of the mean Reynolds stress ($y = 0$ plane).

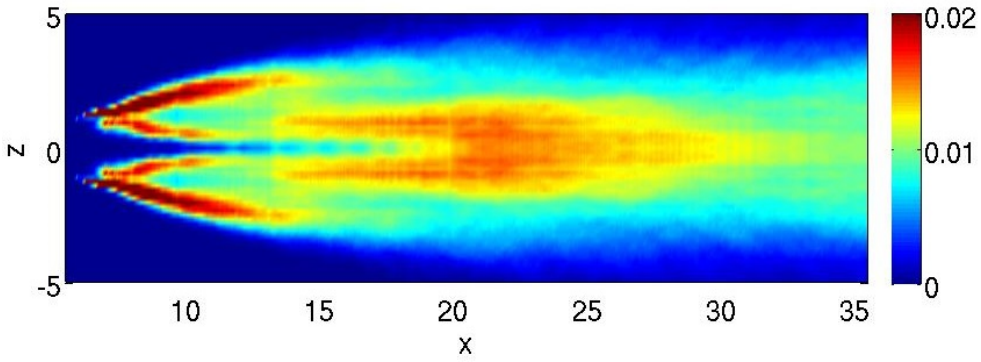

Figure 4.11: $\widetilde{T}_{33}$ component of the mean Reynolds stress ($y = 0$ plane).

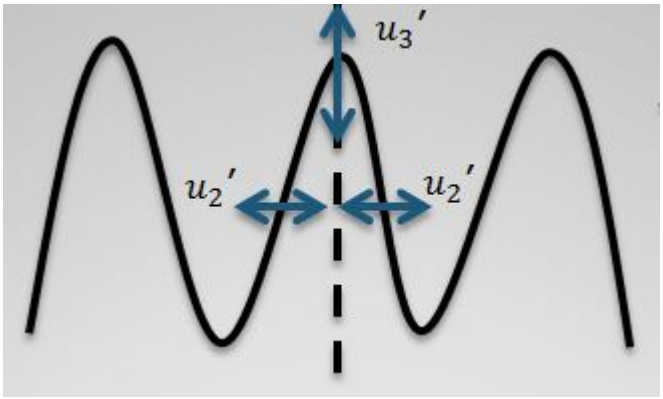

Figure 4.12: Radial cross section of side jets showing fluctuation behavior.

plots, it is apparent that the values are peaked near the nozzle, inside and near the side jets. This can be attributed to the chevrons enhancing turbulence by generating side jets that cause strong shear layers. Also, the shape of the peak values near the nozzle is noticeably different between $\widetilde{T}_{22}$ and $\widetilde{T}_{33}$. The reason for the peak value shape of $\widetilde{T}_{22}$ is that fluctuations in the y direction occur in between the side jets since shear layers form between each side jet. $\widetilde{T}_{33}$'s peak values are shaped differently, horseshoe shaped, because the fluctuations in the z direction occur strongly at the tips of the side jets. This effect can be seen as figure 4.12, where figure 4.12 represents a YZ view of a cross section of the side jets. As will be shown later, these same peak value trends are seen for the fourth order statistics. A three dimensional view as well as a three view system of $\widetilde{T}_{11}$ is shown as figures 4.8 and 4.9 respectively. These figures show an isosurface value of 0.02. The shape of the three dimensional $\widetilde{T}_{11}$ is very similar to that of $\widetilde{u}_1$.

As with the 1^{st} order statistics, we compare 2^{nd} order statistics using basic time averages, $\hat{T}_{11}$, versus Favre averages and the density field, $\widetilde{T}_{11}$. Figure 4.7(b) shows the relative difference between $\widetilde{T}_{11}$ and $\hat{T}_{11}$, where the relative difference is defined as

$$\frac{|\hat{T}_{11} - \widetilde{T}_{11}|}{\widetilde{T}_{11}}. \tag{4.3}$$

Figure 4.7(b) shows that the difference is more pronounced with the 2^{nd} order statistics. Intuitively, this makes sense due to the fact that the smaller differences present with the 1^{st} order statistics become larger when multiplied together to obtain the 2^{nd} order quantities. The differences are up to 10-15% the amount of the actual $\widetilde{T}_{11}$ values. Therefore, the side effect of excluding density from the calculations becomes more pronounced with the 2^{nd} order statistics.

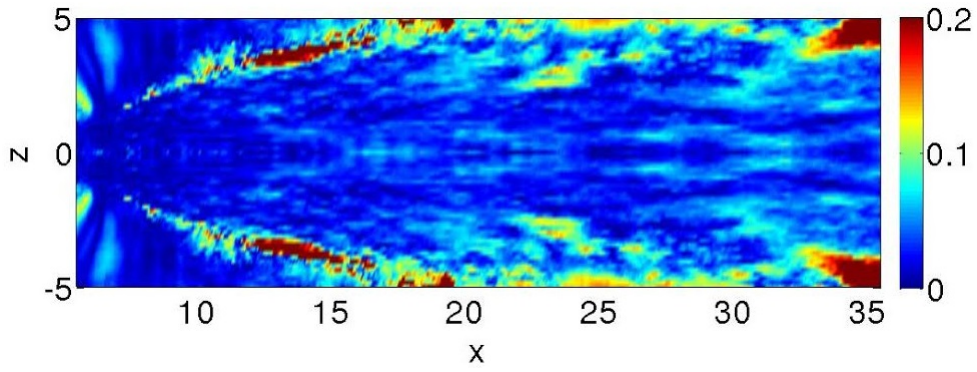

Figure 4.13: Relative change in the $\widetilde{T}_{11}$ mean Reynolds stress field when using the available 7340 snapshots instead of 6000 snapshots.

4.2.1 Convergence test

Figure 4.13 shows the convergence test for the $\widetilde{T}_{11}$ field. The equation for the convergence test is shown as equation 4.4.

$$\left| \frac{\widetilde{T}_{11}(7340 snapshots) - \widetilde{T}_{11}(6000 snapshots)}{\widetilde{T}_{11}(6000 snapshots)} \right| \tag{4.4}$$

The change in solution from 6000 to 7340 snapshots is more pronounced in this case. This of course makes sense due to a less resolved $\widetilde{u}_1$ field being used for the calculation of $\widetilde{T}_{11}$. The edges of the flow field are once again a concern for convergence. While the upstream flow field appears to have not changed much, as one moves farther downstream, the change in solution gradually increases until it uniformly hits close to 10% when $x > 30$. There are certainly a few small areas before $x > 30$, especially closer to the edges of the flow, where the change in solution reaches 10-15%. However, the overall conclusion is that the majority of the flow field would not change by much more than 5% if additional snapshots were available.

4.3 Correlation statistics (fourth order)

Figures 4.14(a), 4.17, and 4.18 represent the correlation terms R_{1111}, R_{2222}, and R_{3333} for the $y = 0$ plane. In the interest of seeing how excluding the density in the calculations affects R_{1111}, figure 4.14(b) has been included to show the residual between R_{1111} and $\hat{R}_{1111}$ for the $y = 0$ plane. The residual is defined as

$$\frac{|\hat{R}_{1111} - R_{1111}|}{R_{1111}}. \tag{4.5}$$

The relative difference is largest for the 4^{th} order statistics which once again makes sense due to 2^{nd} order differences being multiplied together during the 4^{th} order statistical calculations. The relative difference is as high as 25-30% of the original R_{1111} values in some locations. Therefore, the overall determination is that including density and Favre averaging into the R_{1111} calculation makes a significant difference. This makes sense because the flow field is highly compressible. A three dimensional view as well as a three view system of R_{1111} is shown as figures 4.15 and 4.16 respectively. These figures show an isosurface of the value 0.00075. Figure 4.15 shows that the three dimensional plot is similar in shape to both the $\widetilde{T}_{11}$ and $\widetilde{u}_1$ plots.

4.3.1 Convergence test

Once again, a convergence test was done and can be seen for R_{1111} as figure 4.19. The equation for the convergence test is shown as equation 4.6.

$$\left| \frac{R_{1111}(7340 snapshots) - R_{1111}(6000 snapshots)}{R_{1111}(6000 snapshots)} \right| \tag{4.6}$$

As expected, the R_{1111} flow field can be trusted upstream. However, around $x = 20$ there are some solution changes up to roughly 15%. Past this x value, there are various areas of concern, including some small areas reaching 25% solution changes. However,

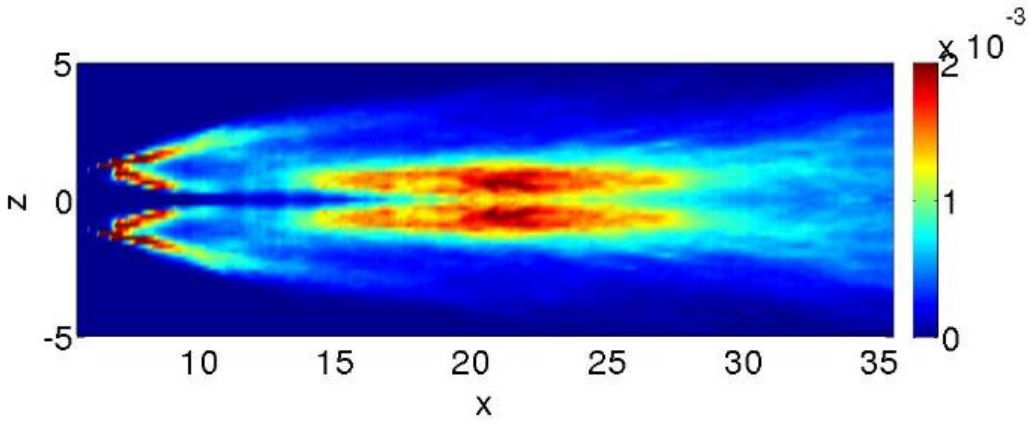

(a) R_{1111} single point fourth order Reynolds stress correlation.

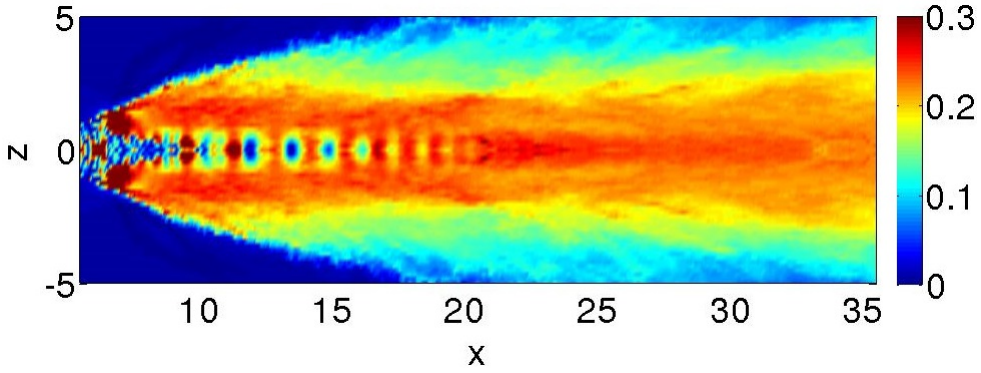

(b) Contours of the residual between the Favre averaged and time averaged fourth order Reynolds stress correlation , R_{1111} and $\hat{R}_{1111}$, respectively.

Figure 4.14: R_{1111} single point fourth order Reynolds stress correlation and comparison between the time averaged and Favre averaged Reynolds stress correlation, $\hat{R}_{1111}$ and R_{1111}, respectively ($y = 0$ plane).

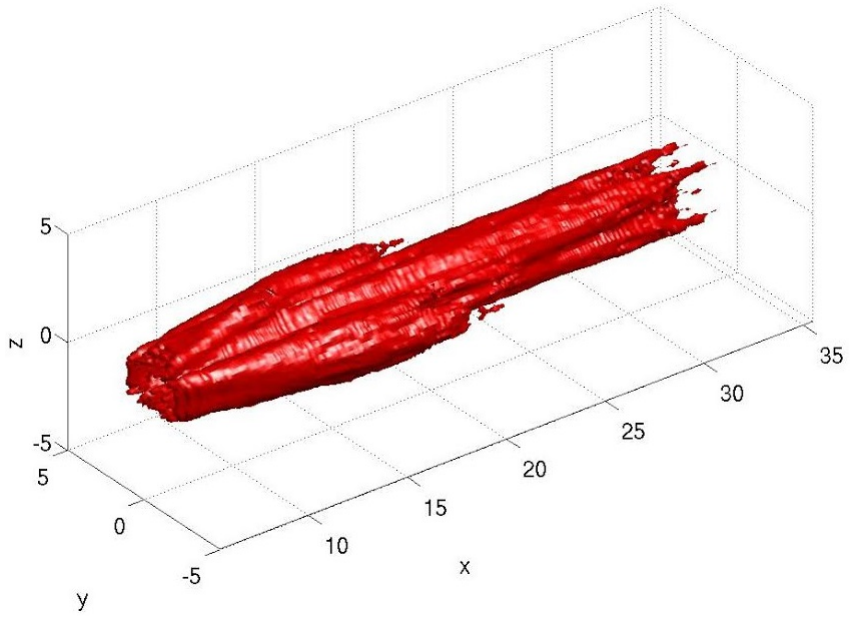

Figure 4.15: A three dimensional view of R_{1111} with no spatial offsets or time delays ($R_{1111} = 0.00075$).

it is still important to note that there is a majority portion of the flow field past $x = 20$ where the solution change is 10% or lower. Therefore, it should be said that the second half of the flow field has areas of concern where the R_{1111} solution could change by up to 25% if additional snapshots were available. Therefore, this area cannot be fully trusted.

4.4 Quasi-normality hypothesis (second and fourth order statistics)

This study was done to see if 2^{nd} order statistics of the flow field can be used to accurately model 4^{th} order acoustic source term behavior. The MGBK code, still used by NASA, is a jet noise prediction code that implements the idea that if a flow is quasi-normal, the scaling factor is the same for all three spatial dimensions [30]. In particular, the code looks

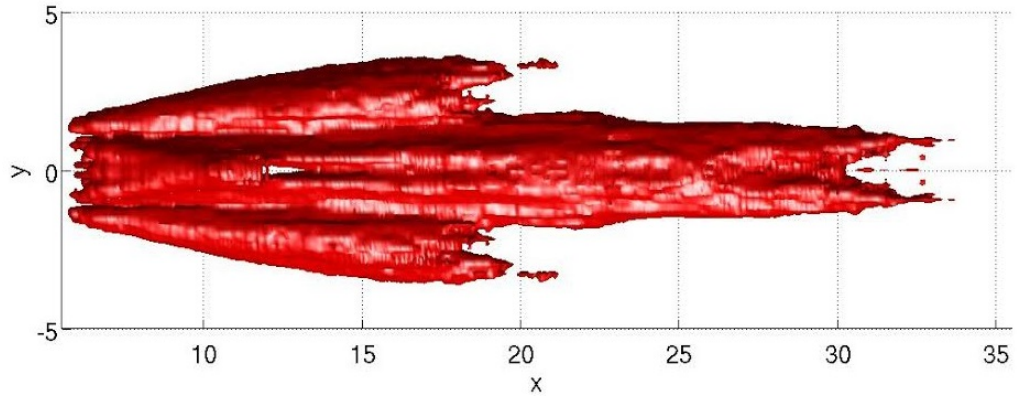

(a) XY view.

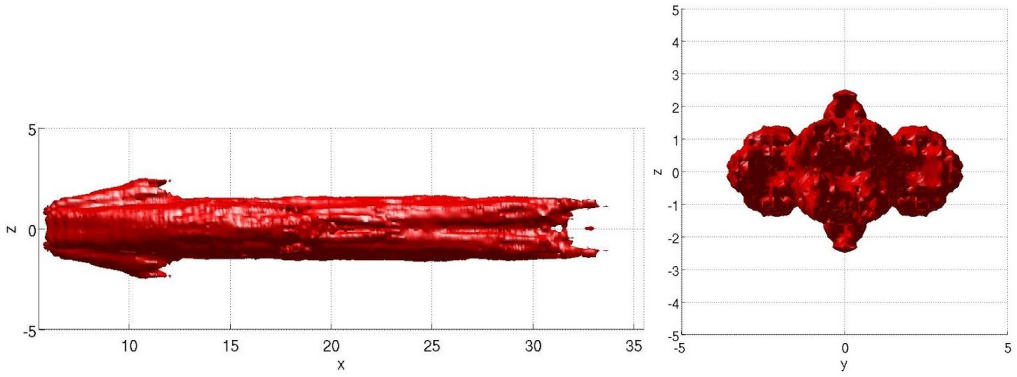

(b) XZ view.

(c) YZ view.

Figure 4.16: A three view system of R_{1111} with no spatial offsets or time delays ($R_{1111} = 0.00075$).

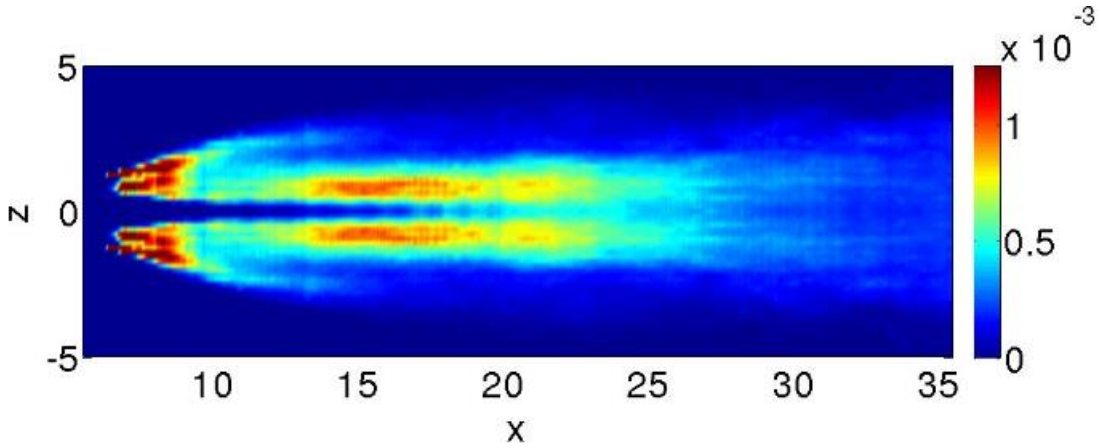

Figure 4.17: R_{2222} with no spatial offsets or time delays ($y = 0$ plane).

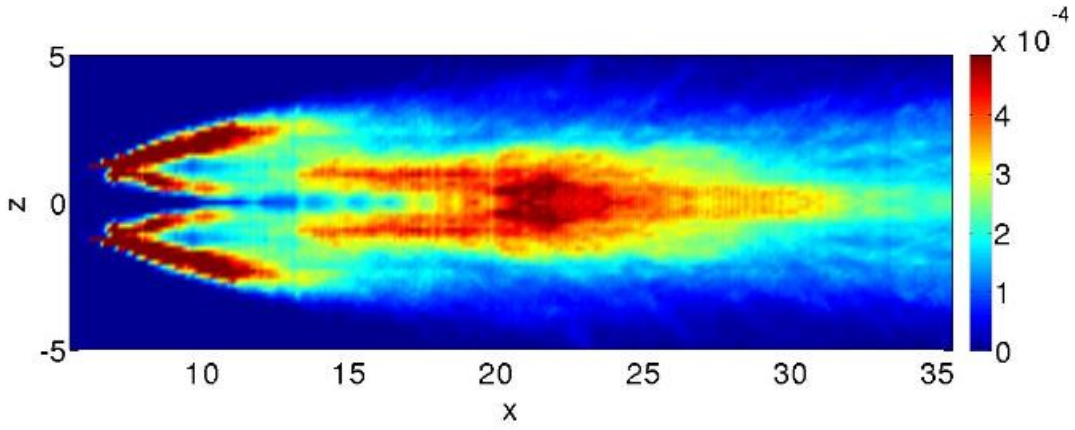

Figure 4.18: R_{3333} with no spatial offsets or time delays ($y = 0$ plane).

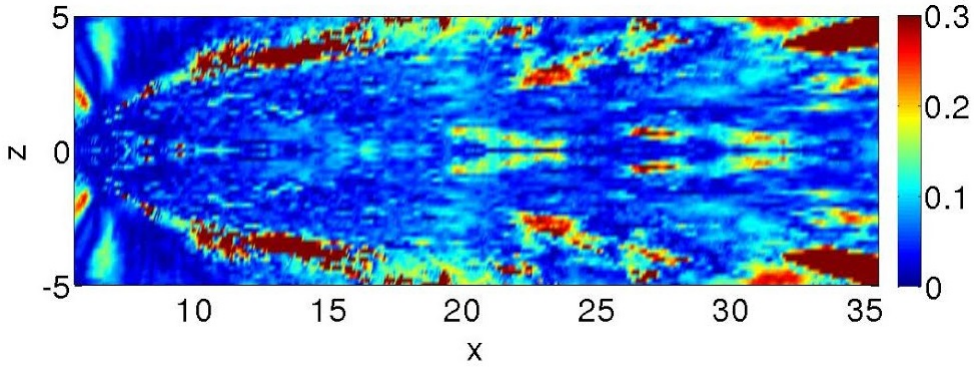

Figure 4.19: Relative change in the R_{11111} field when using the available 7340 snapshots instead of 6000 snapshots.

at two-point quasi-normal studies. Therefore, in order to be consistent with this code, the potential quasi-normality of the flow was first tested by adhering to the logic used by the MGBK code. Both single-point and two-point studies are analyzed. To perform this study, $\hat{R}_{1111}$, $\hat{R}_{2222}$, and $\hat{R}_{3333}$ were calculated and compared to their respective Reynolds stress terms by squaring the Reynolds stresses and multiplying them by a constant factor. This factor was found using a least squares method that minimized the error between the correlation term, $\hat{R}_{1111}$, and the square of the Reynolds stress times the scaling factor, $\alpha \hat{T}_{11}^2$ (see section 3.6.6).

4.4.1 Determining the scaling factor

When no spatial offsets were included, the full 512x65x65 points domain was used for the scaling factor simulation. When spatial offsets were included, the 503x65x65 points domain was used for the simulation. It is important to note that the spatial offset study is not a single point statistical analysis. It is included in this chapter for convenience and comparison to the single point quasi-normality study. As discussed in Chapter 3, we expect a scaling factor of $\alpha = 2$ for quasi-normal processes. Applying the least squares

method, however, resulted in $\alpha = 1.72$. Including correlations at non-zero spatial offsets resulted in $\alpha = 1.70$. While these values are not close to 2, the thought process was that if all three dimensions had this same scaling factor, the flow could still be quasi-normal with the error in scaling factor being possibly due to the LES simulation.

In the interest of seeing how convergence affects the scaling factors, a couple additional studies were done with the single point statistics case. The same simulation that was done to find the scaling factor for the entire three dimensional flow field was applied separately to both the first and second half of the flow field. The two halves were generated by separating the three dimensional flow field into $5.5 \leq x < 20.5$ and $20.5 \leq x \leq 35.5$ parts. When the $5.5 \leq x < 20.5$ section was analyzed, the scaling factor was found to be **1.71**. When the $20.5 \leq x \leq 35.5$ section was analyzed, the scaling factor was calculated to be **1.77**. Therefore, the scaling factor increased by about **3.5%** from the upstream to the downstream section. Therefore, this small difference in upstream and downstream scaling factors means that the scaling factor is largely independent of axial location. Therefore, one should see accurate error minimization between second and fourth order statistics across the entire flow field for a single scaling factor.

The scaling factor was also calculated using 6000 time snapshots instead of the full 7340 snapshots. This way, one can see how much the scaling factor would possibly change if additional snapshots were available. When using 6000 snapshots, the scaling factor is found to be 1.71. This means that from 6000 to 7340 snapshots, the scaling factor changed by **0.58%**. Therefore, this very small change in scaling factor leads to the conclusion that the calculated scaling factor of 1.72 can be trusted to be converged in time.

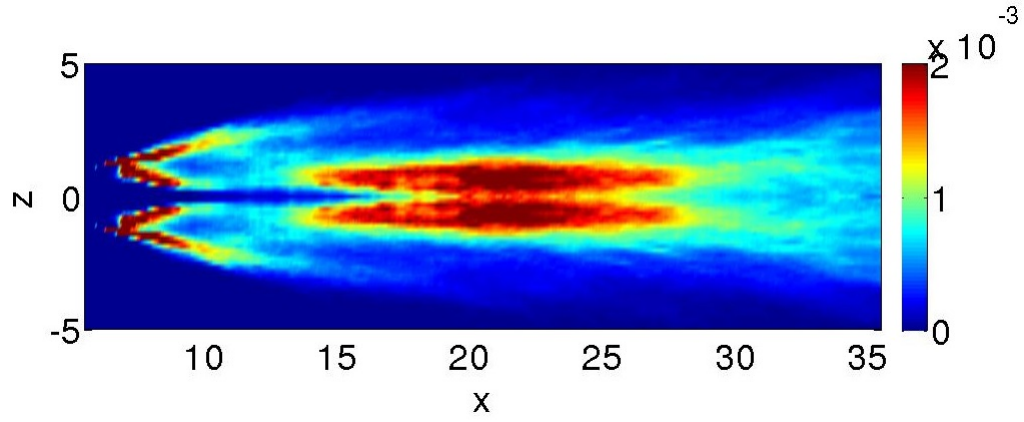

(a) $\hat{R}_{1111}$.

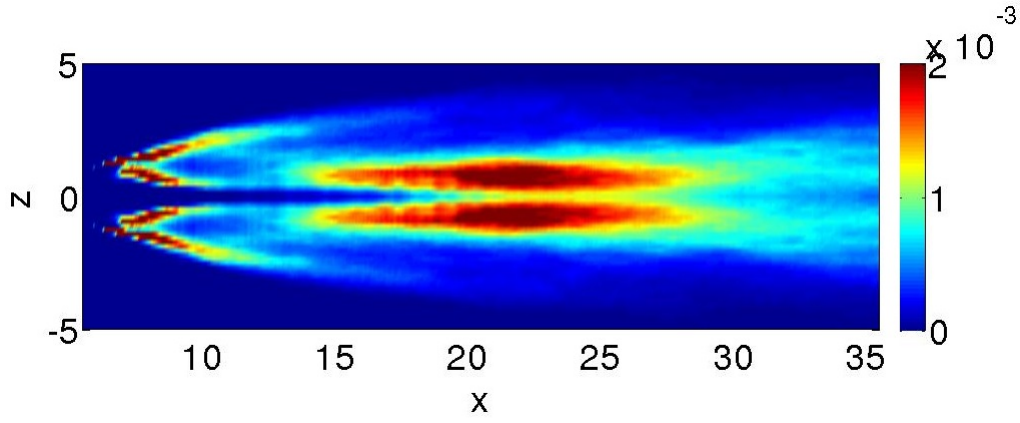

(b) $\alpha\hat{T}_{11}^2$.

Figure 4.20: Comparison of $\hat{R}_{1111}$ and $\alpha\hat{T}_{11}^2$ with no spatial offsets or time delays ($y = 0$ plane).

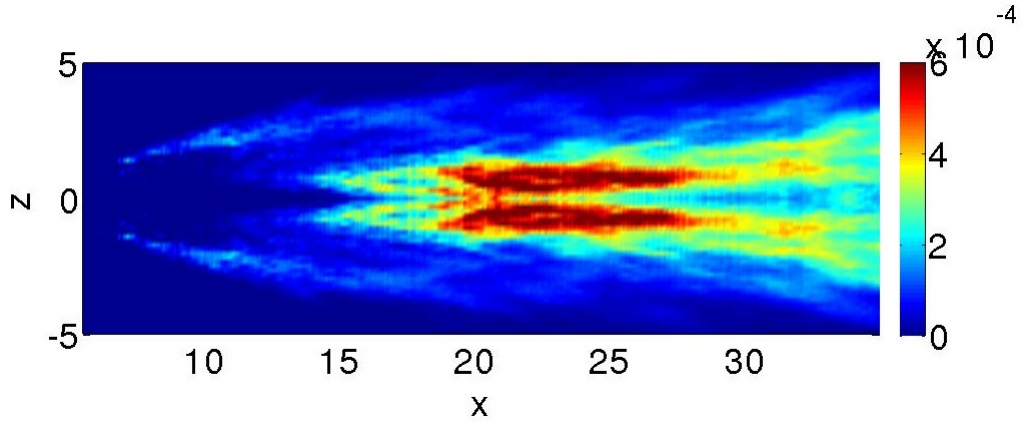

(a) $\hat{R}_{1111}$.

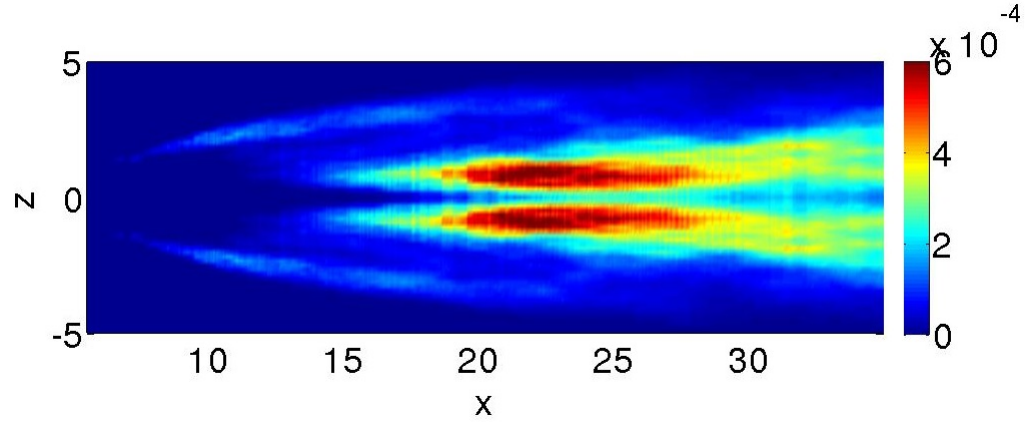

(b) $\alpha\hat{T}^2_{11}$.

Figure 4.21: Comparison of $\hat{R}_{1111}$ and $\alpha\hat{T}^2_{11}$ at 9 Δx spatial offset ($y = 0$ plane).

4.4.2 Comparison between fourth and second order statistics

Figure 4.20 shows the comparison between $\hat{R}_{1111}$ and $\alpha\hat{T}_{11}^2$ with no spatial offsets for the $y = 0$ plane. As already stated, the error between the two was minimized with the appropriate scaling factor. The scaling factor was then used for comparing the other two correlation terms, $\hat{R}_{2222}$ and $\hat{R}_{3333}$, with the square of their respective Reynolds stresses.

Figure 4.21 shows the comparison between $\hat{R}_{1111}$ and $\alpha\hat{T}_{11}^2$ at a spatial offset of 9 Δx for the $y = 0$ plane. The error between the two fields has been minimized with the appropriate scaling factor. It is also important to note that, as expected, the fields at 9 Δx spatial offset have lower values than the fields at zero spatial offset shown in figure 4.20. This is because a given point in the flow field correlates with itself more highly at zero time delay than with a point downstream at zero time delay.

Figure 4.22 shows that $\hat{R}_{2222}$ and $\alpha\hat{T}_{22}^2$ with no spatial offsets actually appear to correlate with one another by possessing the same turbulence shape. This lends some evidence to the fact that in a non-axisymmetric jet, 4^{th} order statistics appear to correlate with 2^{nd} order statistics. Figure 4.23 however appears to show that $\hat{R}_{2222}$ and $\alpha\hat{T}_{22}^2$ do not correlate with each other very well when a spatial offset is considered. This is in contrast to the single point study in figure 4.22. However, they may not correlate well with each other because the flow field is less converged farther downstream. Since the 9 Δx spatial offset comparison in figure 4.23 highlights downstream points in the calculations, this may be a reason as to why they do not correlate as well.

Figure 4.24 shows once again that 4^{th} order statistics appear to correlate with 2^{nd} order statistics when no spatial offsets are considered for $\hat{R}_{3333}$ and $\alpha\hat{T}_{33}^2$. However, once again, figure 4.25 shows a result for spatial offset data that is in contrast to the zero spatial offset data shown in figure 4.24. This may once again be due to convergence issues downstream. This first study has shown that second order statistics appear to correlate with fourth order statistics when single point statistics are considered but not for two-point statistics. The

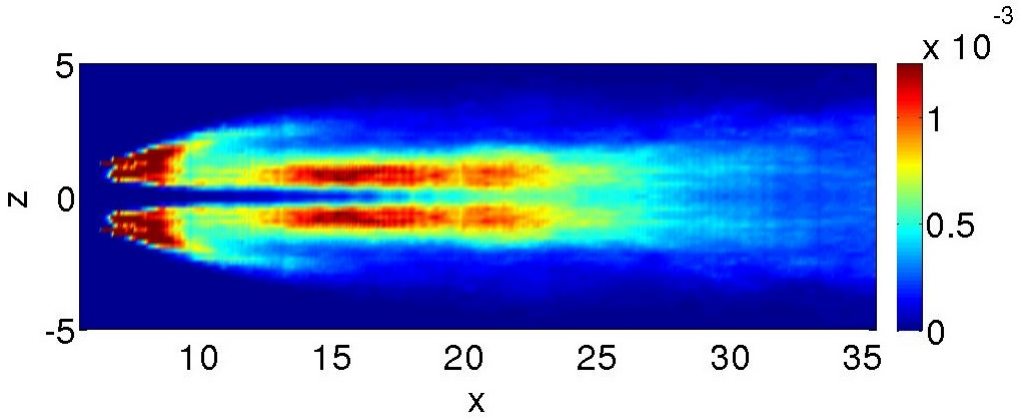

(a) $\hat{R}_{2222}$.

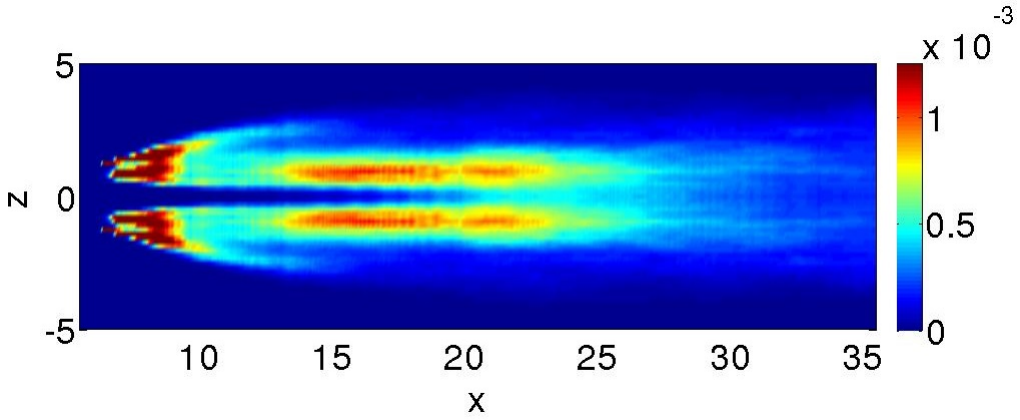

(b) $\alpha\hat{T}_{22}^2$.

Figure 4.22: Comparison of $\hat{R}_{2222}$ and $\alpha\hat{T}_{22}^2$ with no spatial offsets or time delays ($y = 0$ plane).

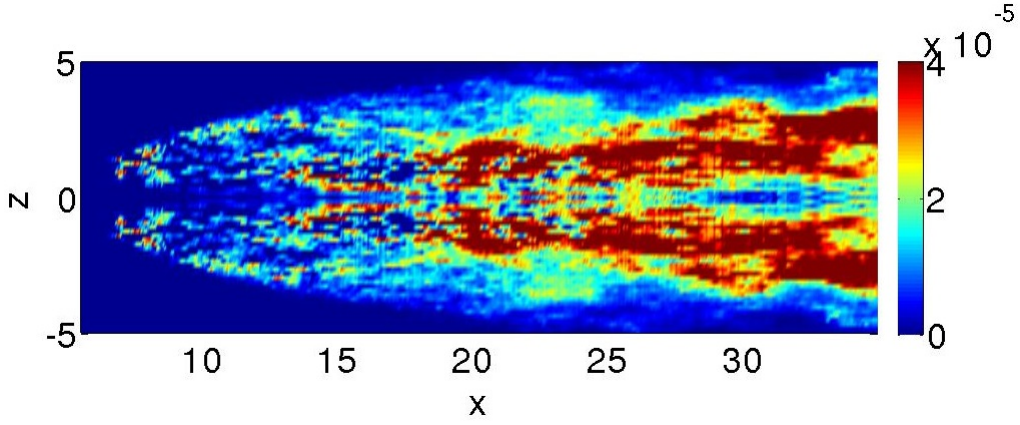

(a) $\hat{R}_{2222}$.

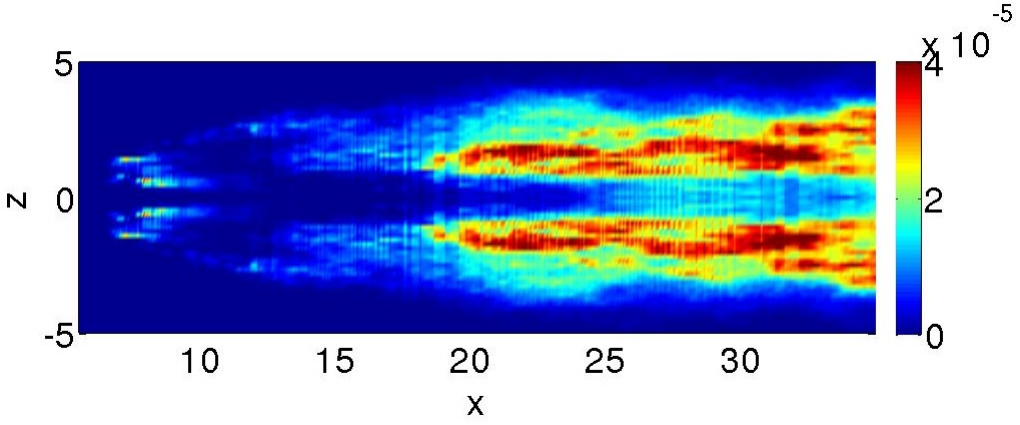

(b) $\alpha\hat{T}^2_{22}$.

Figure 4.23: Comparison of $\hat{R}_{2222}$ and $\alpha\hat{T}^2_{22}$ at 9 Δx spatial offset ($y = 0$ plane).

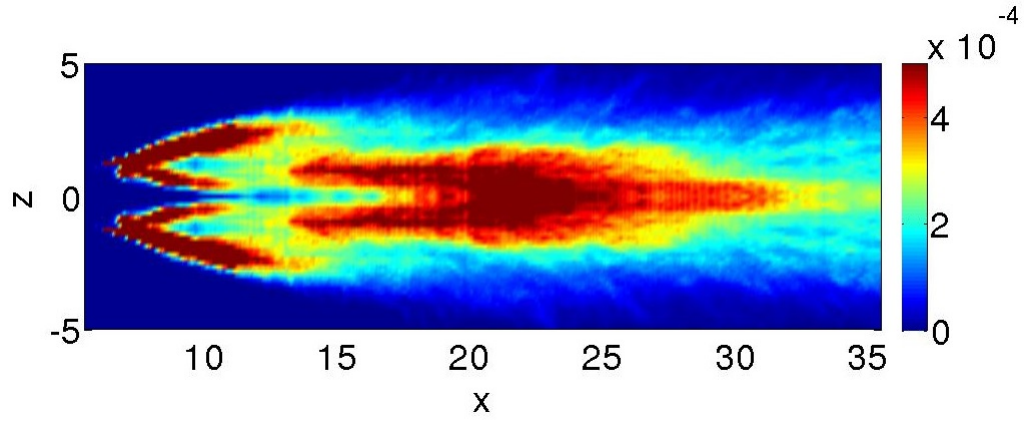

(a) $\hat{R}_{3333}$.

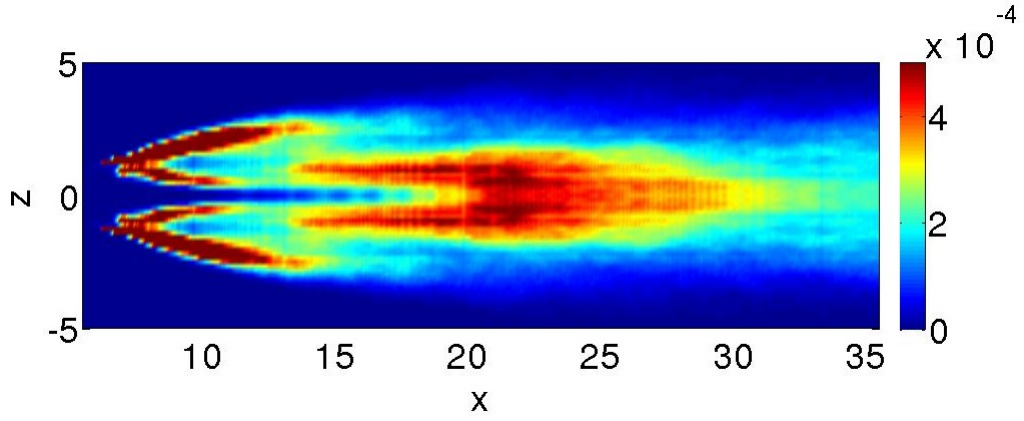

(b) $\alpha\hat{T}_{33}^2$.

Figure 4.24: Comparison of $\hat{R}_{3333}$ and $\alpha\hat{T}_{33}^2$ with no spatial offsets or time delays ($y = 0$ plane).

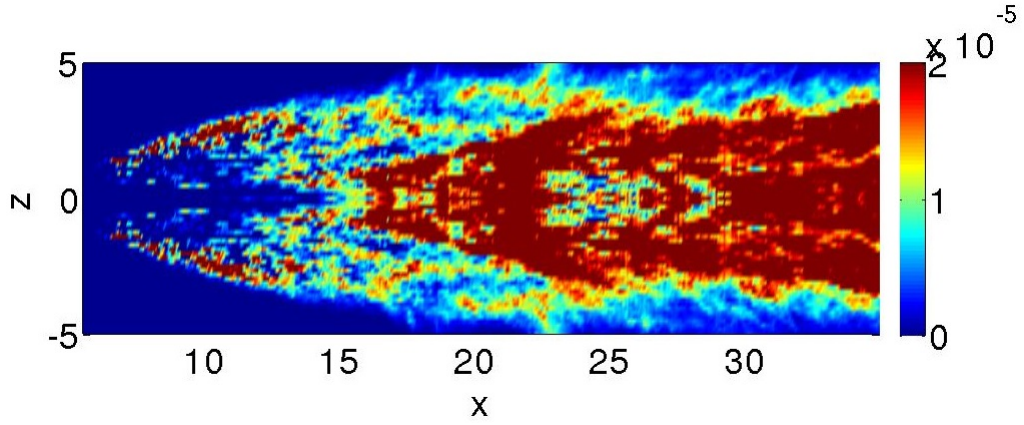

(a) $\hat{R}_{3333}$.

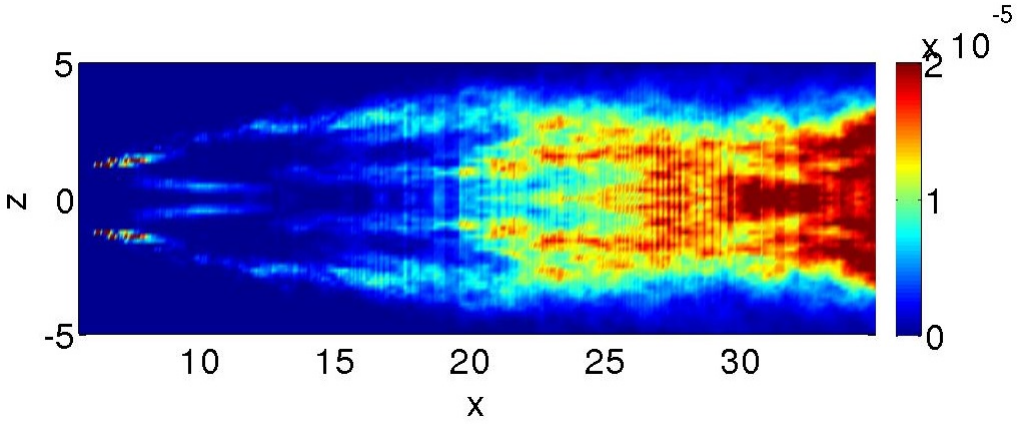

(b) $\alpha\hat{T}^2_{33}$.

Figure 4.25: Comparison of $\hat{R}_{3333}$ and $\alpha\hat{T}^2_{33}$ at 9 Δx spatial offset ($y = 0$ plane).

two-point statistics case could be a victim of convergence problems downstream though.

To quantify the quasi-normal behavior of this flow field, we computed the L^2 norm of the error between the fourth and second order statistics using the calculated scaling factors for no spatial offsets and with offsets included. These values are shown as the first columns of tables 4.1 and 4.2. As expected, the errors are much higher with the spatial offset case in table 4.2. In order to obtain an accurate depiction of the effect of a constant scaling factor being used, minimum L^2 norm of the error and optimized scaling factor columns were included. It was stated earlier that the constant scaling factors that were used were calculated based on minimizing the error between $\hat{R}_{1111}$ and $\alpha\hat{T}_{11}^2$. These scaling factors were found to be much lower than 2. Therefore, it was desired to see if the transverse directions yielded scaling factors that were closer to 2 because this would indicate quasi-normality in these directions.

The optimized scaling factor column represents a calculated scaling factor based on minimizing the error between the corresponding 4^{th} and 2^{nd} order statistic in the same row. This process is where the minimum L^2 norm of the error was found. Theoretically, if the flow field is quasi-normal in all directions, the optimized scaling factors should all be 2. This is seen to not be the case based on analyzing tables 4.1 and 4.2. In particular, the scaling factors found for the axial directions reach up to 15% error. Interestingly enough though, the optimized scaling factors for the $\hat{R}_{2222}$ and $\hat{R}_{3333}$ cases are actually very close to 2 with errors all below 5%. Therefore, it would appear that the transverse components of the flow field are nearly quasi-normal, while the axial direction is not.

Figure 4.26 directly compares second and fourth order statistics for each spatial dimension using the theoretical scaling factor of 2. Every data point, represented by the dots, has a horizontal coordinate equal to the lower order statistic and a vertical coordinate equal to the corresponding higher order statistic. The line of equality is represented by the solid line. The entire flow field was analyzed. For quasi-normality, the data should

	L^2 **Norm**	**Min.** L^2 **Norm**	**Optimized** α	**Percent Error** (α)
$\hat{R}_{1111}$ **and** $\alpha\hat{T}^2_{11}$	0.1874	0.1874	1.72	14%
$\hat{R}_{2222}$ **and** $\alpha\hat{T}^2_{22}$	0.0874	0.07233	1.94	3%
$\hat{R}_{3333}$ **and** $\alpha\hat{T}^2_{33}$	0.0878	0.07607	1.91	4.5%

Table 4.1: Error analysis for quasi-normality study without spatial offsets.

	L^2 **Norm**	**Min.** L^2 **Norm**	**Optimized** α	**Percent Error** (α)
$\hat{R}_{1111}$ **and** $\alpha\hat{T}^2_{11}$	0.3515	0.3515	1.70	15%
$\hat{R}_{2222}$ **and** $\alpha\hat{T}^2_{22}$	0.1395	0.1160	1.97	1.5%
$\hat{R}_{3333}$ **and** $\alpha\hat{T}^2_{33}$	0.1362	0.1160	1.95	2.5%

Table 4.2: Error analysis for quasi-normality study including spatial offsets.

match up with the line of equality because this line indicates that the theoretical scaling factor perfectly equates the square of the lower order statistics with the higher order statistics. It can be seen that Figure 4.26(a) once again shows that the axial direction is not quasi-normal since the data do not correspond well to the line of equality. Figure 4.26(b-c) shows that, as expected, the transverse directions are quasi-normal because the data line up pretty well with the line of equality.

The same study done in figure 4.26 was done for the upstream and downstream half of the flow field with $\hat{R}_{2222}$ and $2\hat{T}^2_{22}$ and shown as figure 4.27. Figure 4.27 shows that the flow appears to be more quasi-normal farther downstream due to the data adhering to the line of equality better compared to the upstream section. Higher order statistics appear to correlate with lower order statistics better in lower turbulent regions.

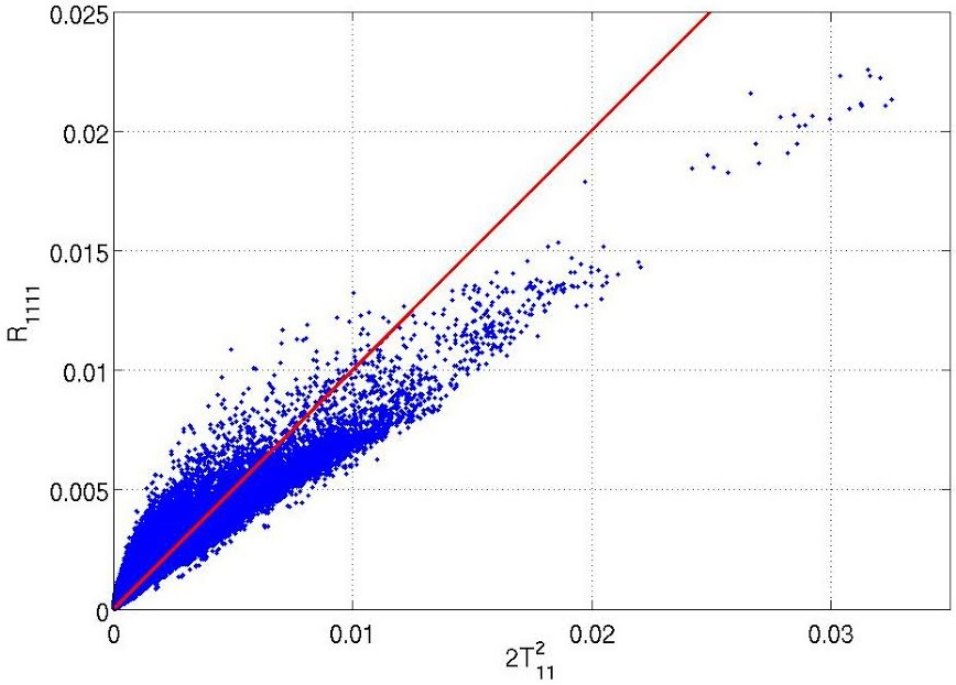

(a) $\hat{R}_{1111}$ vs. $2\hat{T}^2_{11}$.

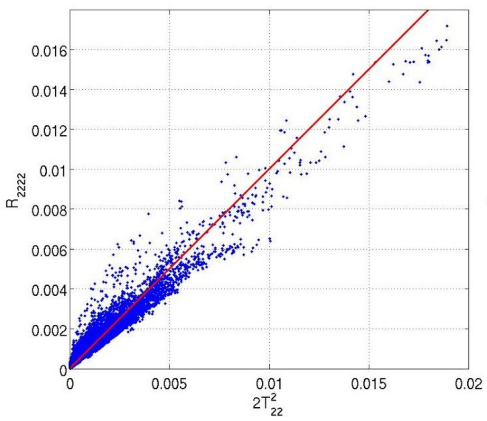

(b) $\hat{R}_{2222}$ vs. $2\hat{T}^2_{22}$.

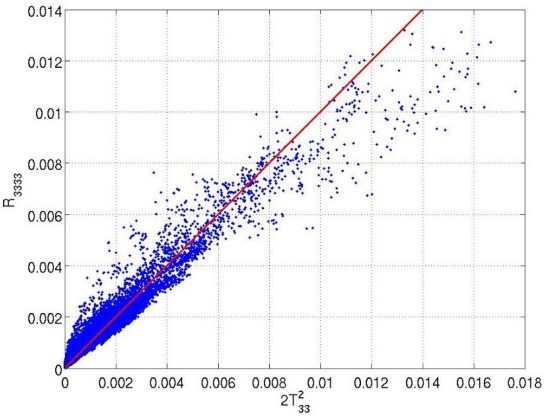

(c) $\hat{R}_{3333}$ vs. $2\hat{T}^2_{33}$.

Figure 4.26: Comparison of second and fourth order statistics by using the theoretical scaling factor and seeing if statistics adhere to line of equality (solid line = line of equality; dots = simulated data).

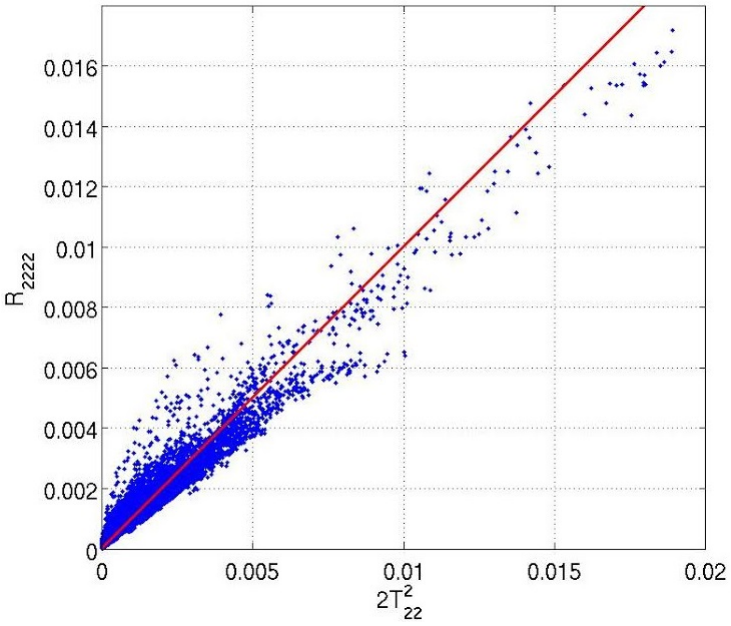

(a) Upstream half.

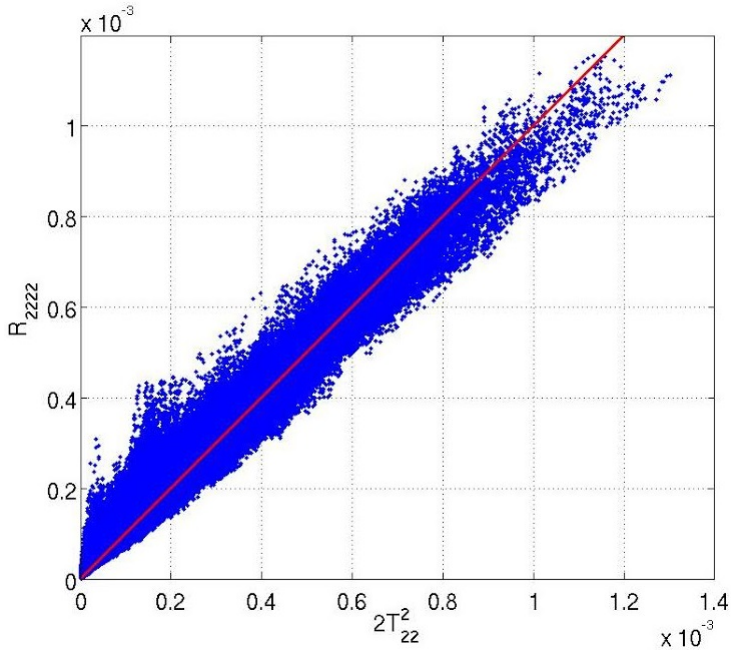

(b) Downstream half.

Figure 4.27: Comparison of $\hat{R}_{2222}$ and $2\hat{T}^2_{22}$ by analyzing both the upstream and downstream sections of the flow field.

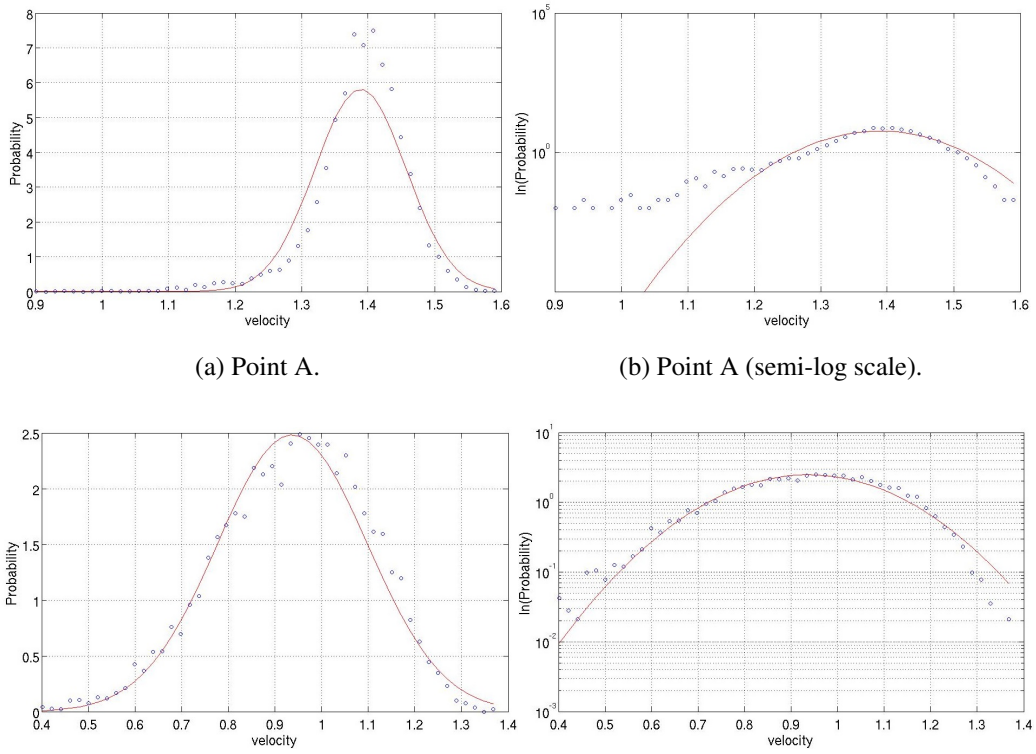

(a) Point A.

(b) Point A (semi-log scale).

(c) Point B.

(d) Point B (semi-log scale).

Figure 4.28: PDF analysis of u_1 with Gaussian curve fits for two selected points (circles = PDF data; solid lines = Gaussian curve).

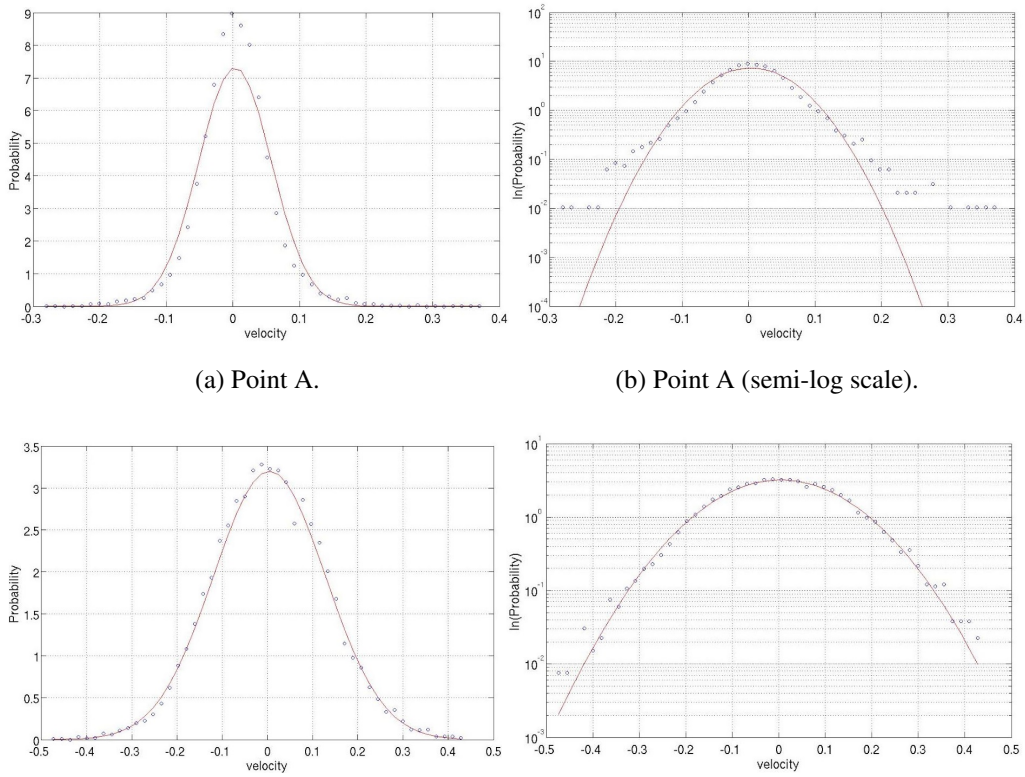

(a) Point A.

(b) Point A (semi-log scale).

(c) Point B.

(d) Point B (semi-log scale).

Figure 4.29: PDF analysis of u_2 with Gaussian curve fits for two selected points (circles = PDF data; solid lines = Gaussian curve).

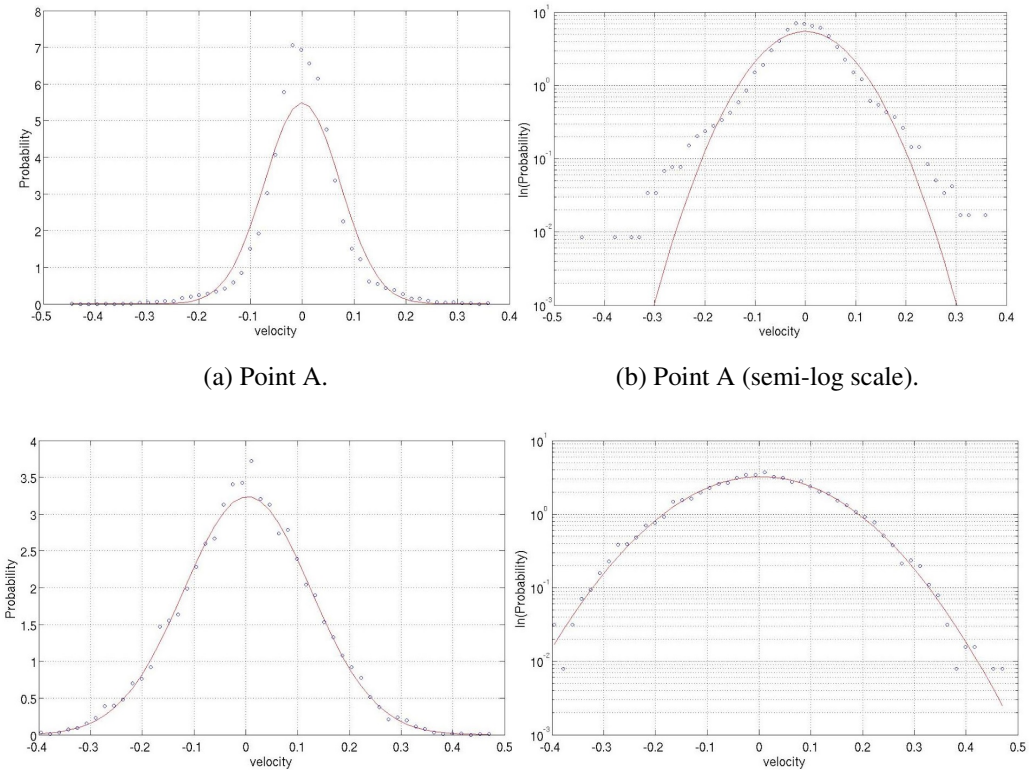

(a) Point A.

(b) Point A (semi-log scale).

(c) Point B.

(d) Point B (semi-log scale).

Figure 4.30: PDF analysis of u_3 with Gaussian curve fits for two selected points (circles = PDF data; solid lines = Gaussian curve).

4.4.3 PDF Analysis

To further verify the finding in the previous section, a probability distribution function (PDF) analysis was done for two separate points in the flow field. These points can be seen as Points A and B in figure 4.5. The points were chosen to highlight upstream and downstream behavior. The PDF velocity data, calculated from a histogram study, are compared to Gaussian curves with the same mean and standard deviation as the velocity data. If the data are perfectly Gaussian, the component of velocity under analysis is normal. Figure 4.28 shows PDF plots for the axial component of velocity. The data represented by the circles are the PDF velocity data, while the solid lines represent the Gaussian curve. These plots reveal that the axial velocity is skewed and therefore not quasi-normal. The skewness is particularly noticeable if the semi-log scale plots are analyzed. This is evident by the asymmetry of the data. However, figures 4.29 and 4.30 show that the transverse velocities are closer to Gaussian, and therefore this is further evidence of their quasi-normality. There is still some skewness associated with the transverse velocities, though. Table 4.3 shows the skewness, quantified by

$$SK(u_i) = E\left[\frac{(u_i - \bar{u_i})^3}{\sigma_{u_i}^3}\right]. \tag{4.7}$$

The skewness of the transverse velocity components is approximately an order of magnitude less than the skewness of the streamwise component in all cases. Since Millionshchikov's identity holds when the third order cumulants (skewness) are zero, the y and z directions of the flow field are determined to be fairly quasi-normal, while the axial direction is not. Another interesting observation is that the skewness is higher for all three velocity components for the upstream point. This would indicate that the flow is more quasi-normal farther downstream. This trend was also seen in the previous section.

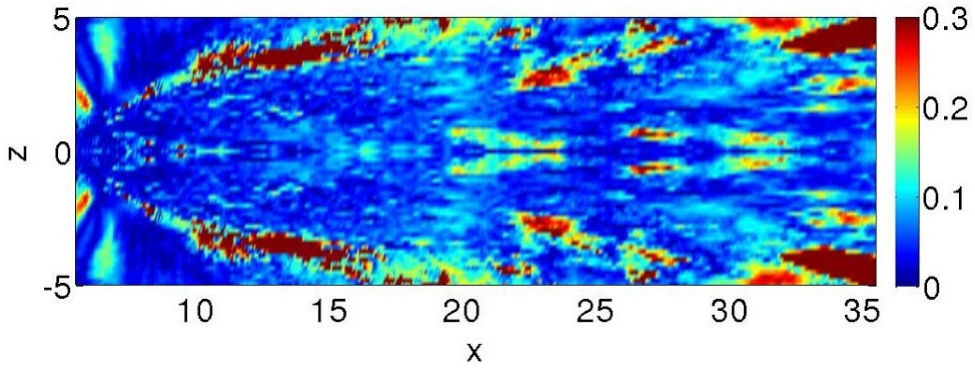

(a) $\hat{R}_{1111}$.

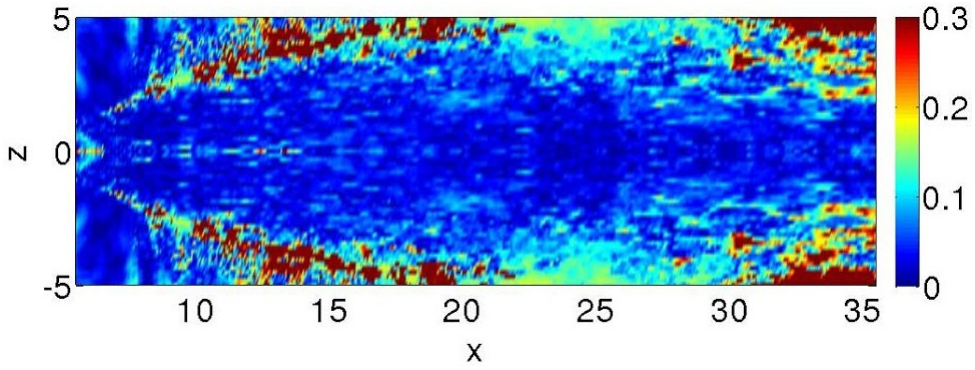

(b) $\hat{R}_{2222}$.

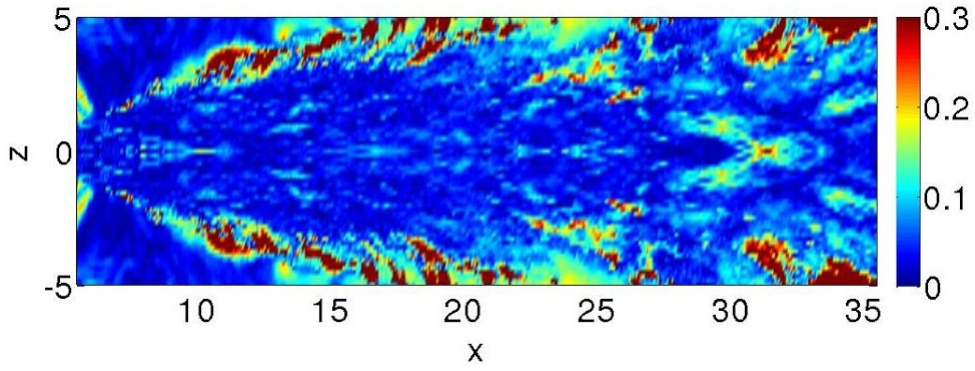

(c) $\hat{R}_{3333}$.

Figure 4.31: Convergence test for the quasi-normality study ($y = 0$ plane).

	u_1	u_2	u_3
Upstream	-1.2244	0.2053	-0.1086
Downstream	-0.3018	0.0366	-0.0083

Table 4.3: PDF Skewness

4.4.4 Convergence test

Figure 4.31 shows the same sample size convergence study that was done for the other statistics in this chapter but for $\hat{R}_{1111}$, $\hat{R}_{2222}$, and $\hat{R}_{3333}$ instead. The main purpose of this study was to see in particular if $\hat{R}_{2222}$ and $\hat{R}_{3333}$ experience higher convergence errors due to their smaller values compared to $\hat{R}_{1111}$. It is seen from figure 4.31 that they do not.

4.5 Statistical axisymmetry (fourth order statistics)

Two different equations were used to test if there was local statistical axisymmetry in the flow [28]. Both sides of equations 3.27 and 3.28 were calculated separately to find the residual error. The results are shown in figure 4.32 for the $y = 0$ plane. Both methods show that most of the flow field is indeed locally statistically axisymmetric due to the low error residual values. A key portion of the flow field that does not fit this description is far upstream near the nozzle. It is believed that the generated side jets are causing highly three dimensional behavior far upstream due to enhanced turbulent mixing specifically between side jets and at the tips of side jets. This is then causing local non-axisymmetric behavior of the fluctuations near the nozzle. As the flow field evolves downstream to form a "plus-shaped" cross section, it appears to be more locally statistically axisymmetric.

An additional test was done to test statistical axisymmetry. Mainly, the identity $R_{2222} = R_{3333}$ was tested since, as stated earlier, this identity should hold for statistical axisymmetry. It should be noted that, as shown before in the statistical axisymmetry

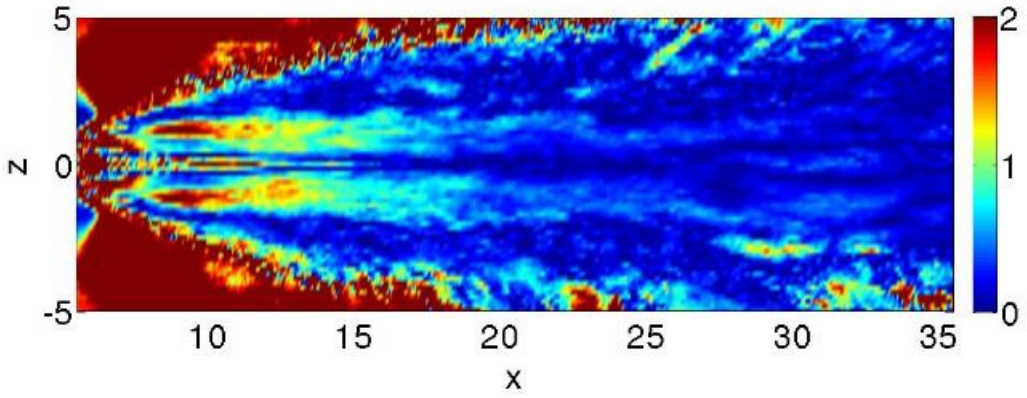

(a) Hermitian quadratic form.

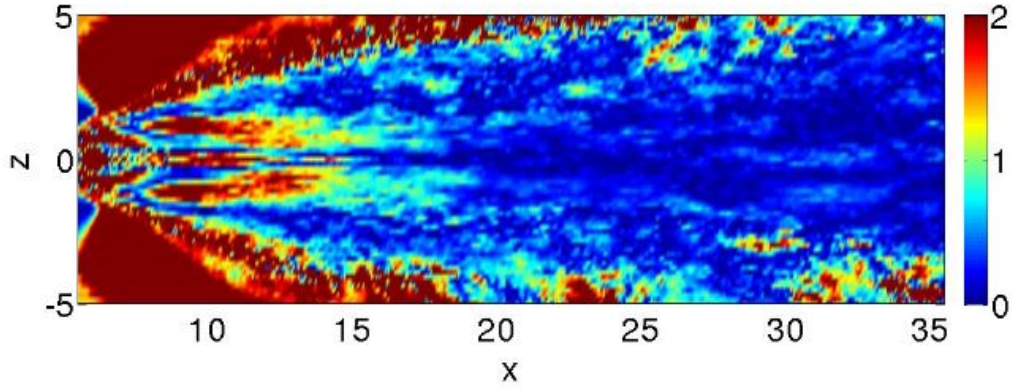

(b) Diagonal quadratic form.

Figure 4.32: Statistical axisymmetry test ($y = 0$ plane).

section of Chapter 3, this identity was included in the equations that were used for the study shown in figure 4.32. A residual error was calculated between R_{2222} and R_{3333} and shown in figure 4.33. The residual error is defined as

$$\left| \frac{R_{2222} - R_{3333}}{R_{2222}} \right|. \tag{4.8}$$

The difference between the two correlations is actually very significant in some areas. The error residuals in some areas are nearly as large as the correlation value R_{2222}. Once again, the error is highest near the nozzle where the three dimensional behavior is strong. However, closer to the edges of the flow field, the errors are low. Therefore, this study suggests that towards the edges of the flow field, the flow is statistically axisymmetric for the $y = 0$ plane. It should be noted that the equations used to test statistical axisymmetry in the first study utilized the additional identities of $R_{1122} = R_{1133}$ and $R_{1212} = R_{1313}$ that are vital to a full description of statistical axisymmetry. Therefore, these identities may agree better in the flow field, and hence the first study possibly found better results in more areas of the flow field because of it. All in all, both studies at least seem to agree that closer to the edges of the moving flow, the flow field can be trusted to be locally statistically axisymmetric.

Figure 4.34 shows a scatter plot comparison between R_{2222} (horizontal axis) and R_{3333} (vertical axis) with the line of equality denoted by the solid line. As one can see, while some of the data adhere well to the line of equality, a lot of the data do not. Specifically, Regions 1 and 2 from figure 4.34 were looked at to see where in the flow field these regions resided. Figure 4.35 is the result of this study. Region 1 is represented by the blue dots, while Region 2 is represented by the black dots. As one can see, since Region 1 is dominated by high R_{2222} values, the data reside more between the side jets. This is due to strong fluctuations in the y direction occurring between side jets, as previously discussed. Also, Region 2 is dominated by high R_{3333} values, so the data in this region

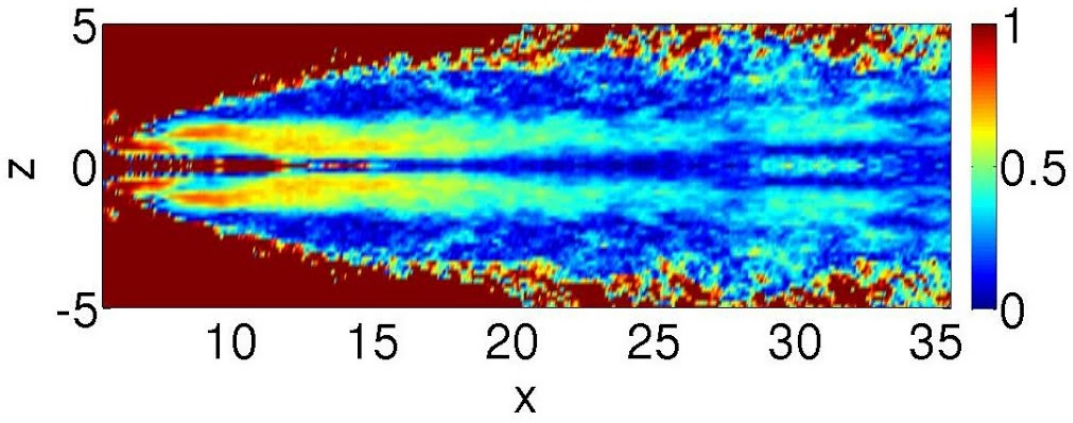

Figure 4.33: Residual error between R_{2222} and R_{3333} ($y = 0$ plane).

reside more on the tips of the side jets since fluctuations in the z direction occur strongly at the tips of the side jets. Overall, it can be seen that Regions 1 and 2, which contain highly statistical nonaxisymmetric behavior, primarily reside upstream and towards the side jets, as expected.

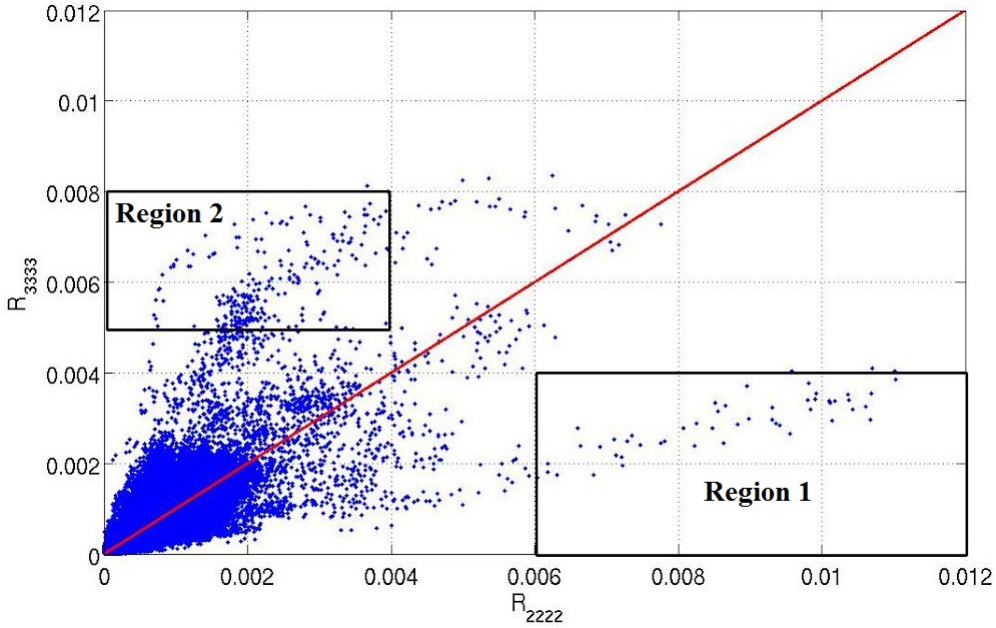

Figure 4.34: R_{3333} vs. R_{2222} (dots = simulated data; solid line = line of equality).

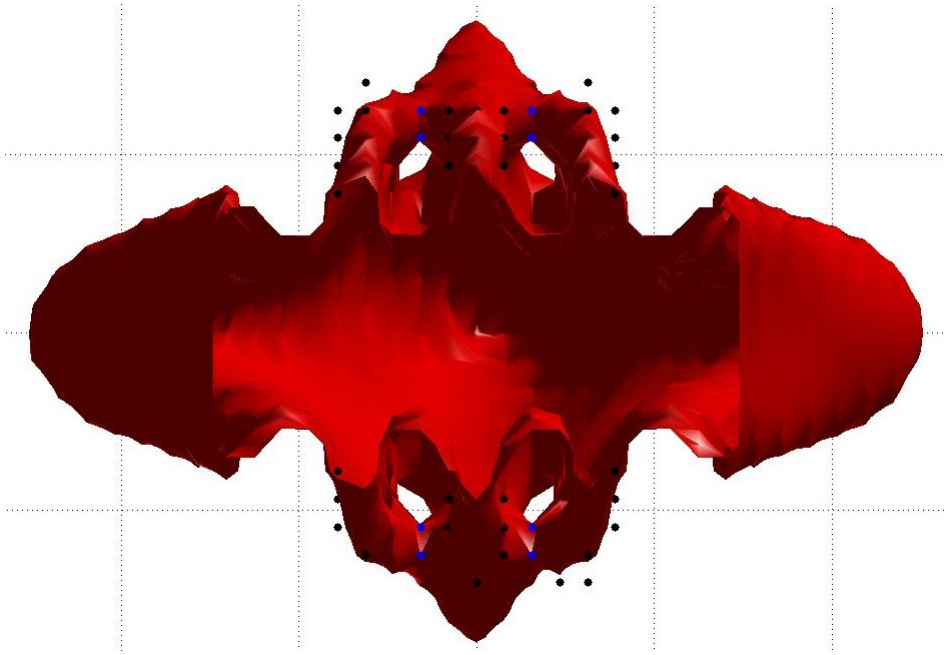

Figure 4.35: Radial cross section of the mean velocity flow field showing Region 1 data (blue dots) and Region 2 data (black dots). Region 1 and 2 are shown in figure 4.34.

Chapter 5

Two-point, two-time statistics

In the previous chapter, we looked at single point statistics in detail including testing the acoustic source model assumptions of quasi-normality and statistical axisymmetry. In this chapter, we directly apply the acoustic source models to two-point, two-time correlations of the analyzed complex jet in order to dictate the accuracy of the models. All cross correlation calculations in this chapter are for R_{1111} because it contributes the most to the sound radiation [18].

5.1 Coefficient fits

The following section will show all coefficient fields related to the acoustic source models for the $y = 0$ plane.

5.1.1 Gaussian model

As shown already in equation 3.29, equation 5.1 is the Gaussian model equation that is used for this thesis with fitting coefficients shown in bold. This model has four free parameters, defined in Chapter 3, that are determined by the fitting procedure discussed

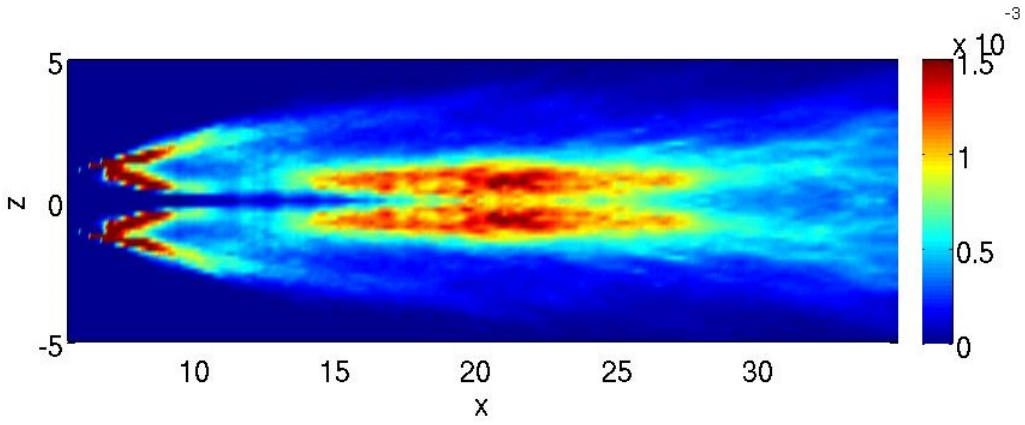

Figure 5.1: Amplitude fit for the Gaussian model ($y = 0$ plane).

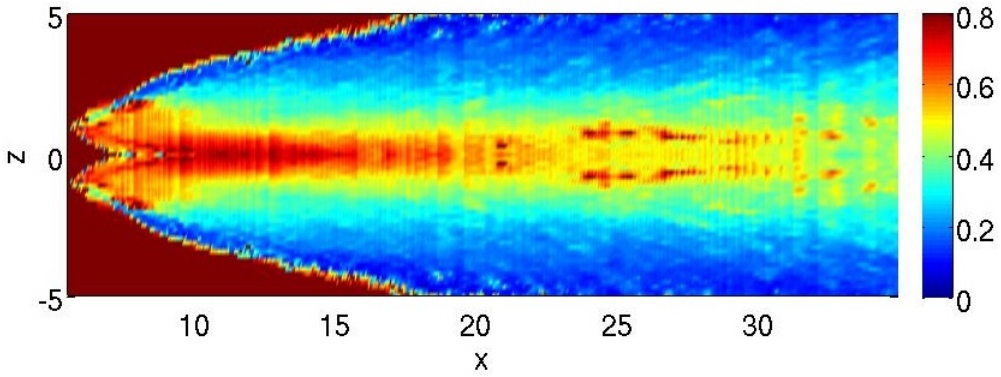

Figure 5.2: Convection velocity fit for the Gaussian model ($y = 0$ plane).

in Chapter 3.

$$R_{ijkl}(\vec{x}, \Delta_1, \tau) = \boldsymbol{A_{ijkl}} exp\left[-\frac{\Delta_1}{\widetilde{\boldsymbol{v_1}}\boldsymbol{\tau_s}} - \ln 2\left(\frac{(\Delta_1 - \widetilde{\boldsymbol{v_1}}\tau)^2}{\boldsymbol{l_1}^2}\right)\right] \tag{5.1}$$

Figures 5.1, 5.2, 5.3, and 5.4 are visual representations of the coefficient fits for the flow field using the Gaussian model equation. The coefficient fit fields appear to correctly capture the gross features of the flow. The amplitude is largest close to the nozzle, as expected. The convection velocity is maximized at the center of the flow field and goes to zero towards the edges of the flow field. Also, the time and length scales get larger farther

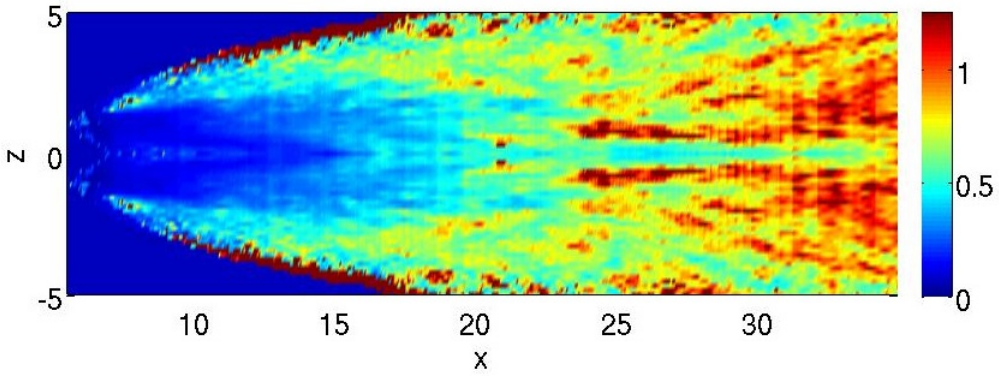

Figure 5.3: Length scale fit for the Gaussian model ($y = 0$ plane).

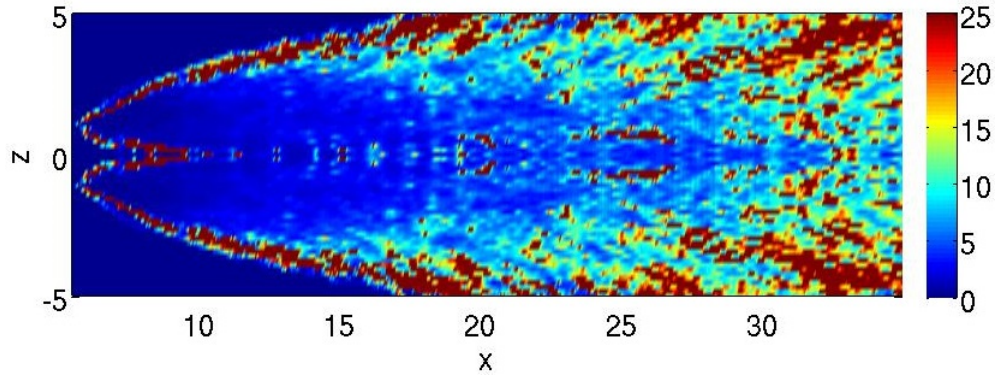

Figure 5.4: Time scale fit for the Gaussian model ($y = 0$ plane).

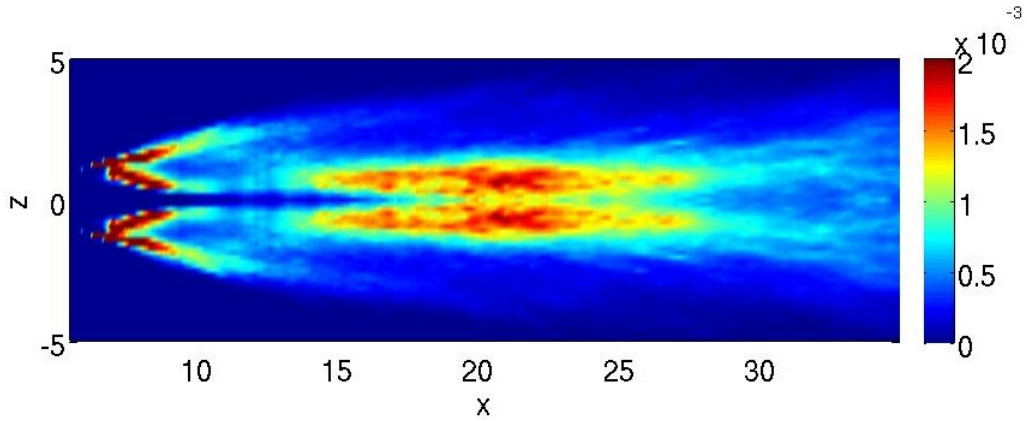

Figure 5.5: Amplitude fit for the moving-frame model ($y = 0$ plane).

downstream, as expected. They also get larger near the edges of the flow field. The flow is slower near the edges, so this makes sense as well. All expected trends of the flow field are seen using this model.

5.1.2 Moving-frame model

As shown already in equation 3.30, equation 5.2 is the moving-frame model equation that is used for this thesis with fitting coefficients shown in bold. This model has four free parameters.

$$R_{ijkl}(\vec{x}, \Delta_1, \tau) = \boldsymbol{A_{ijkl}} exp\left[-\left(\left(\frac{(\Delta_1 - \widetilde{\boldsymbol{v_1}}\tau)}{\boldsymbol{l_1}}\right)^2 + \left(\frac{\tau}{\boldsymbol{\tau_s}}\right)^2\right)^{0.5}\right] \tag{5.2}$$

Figures 5.5, 5.6, 5.7, and 5.8 are visual representations of the coefficient fits for the flow field using a moving-frame model. Once again, the coefficient fits capture the gross features of the flow.

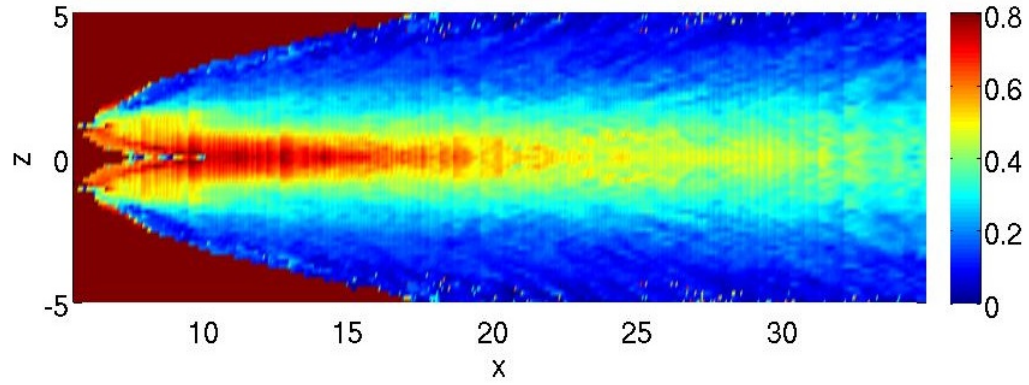

Figure 5.6: Convection velocity fit for the moving-frame model ($y = 0$ plane).

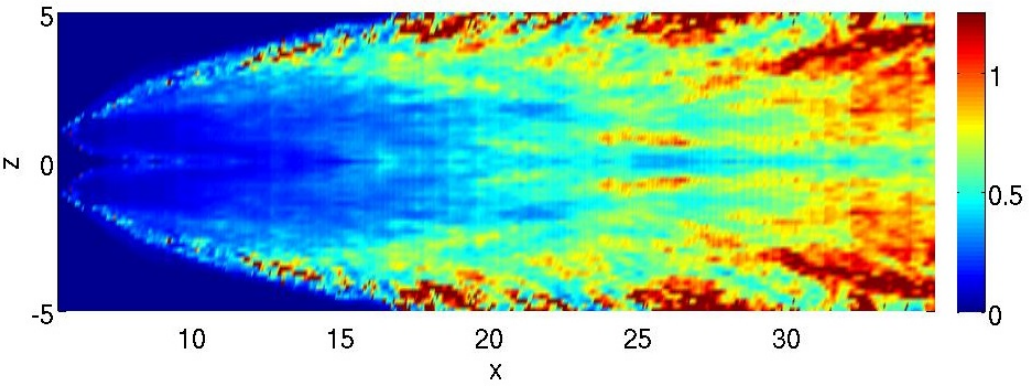

Figure 5.7: Length scale fit for the moving-frame model ($y = 0$ plane).

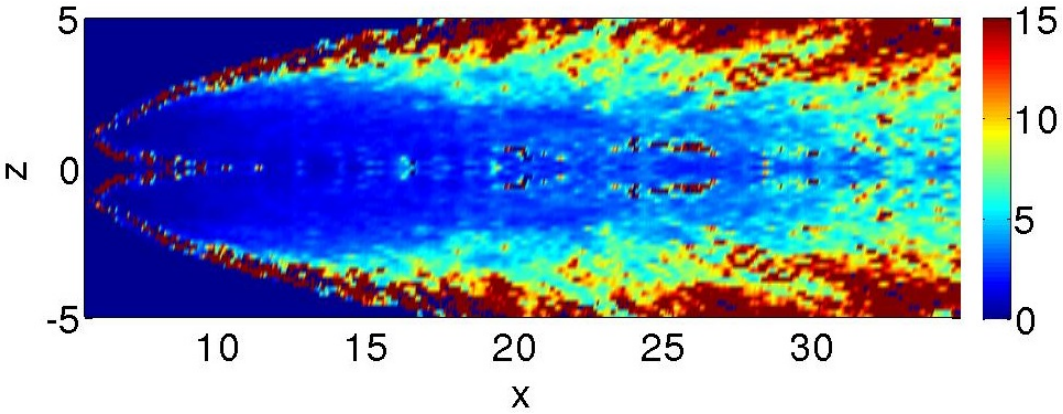

Figure 5.8: Time scale fit for the moving-frame model ($y = 0$ plane).

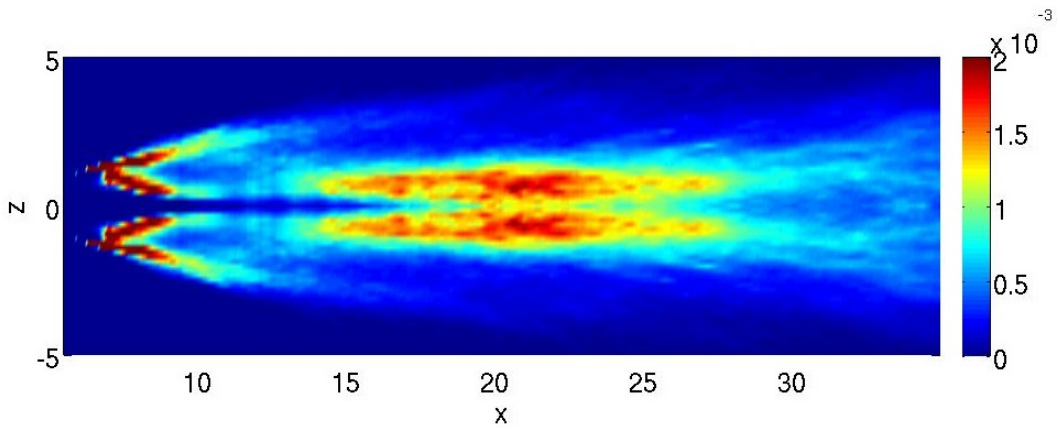

Figure 5.9: Amplitude fit for the fixed-frame model ($y = 0$ plane).

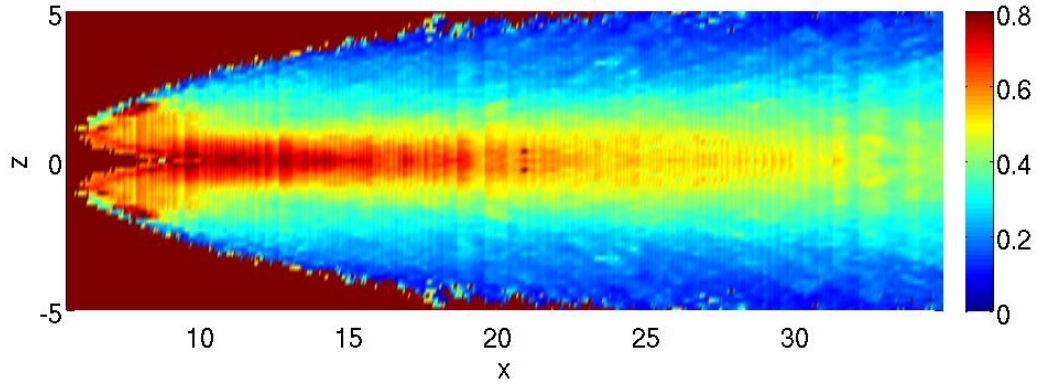

Figure 5.10: Convection velocity fit for the fixed-frame model ($y = 0$ plane).

5.1.3 Fixed-frame model

As shown already in equation 3.31, equation 5.3 is the fixed-frame model equation that is used for this thesis with fitting coefficients shown in bold. This model has four free parameters.

$$R_{ijkl}(\vec{x}, \Delta_1, \tau) = \boldsymbol{A_{ijkl}} exp\left[-\left(\left(\frac{(\Delta_1 - \widetilde{\boldsymbol{v_1}}\tau)}{\boldsymbol{l_0}}\right)^2 + \left(\frac{\Delta_1}{\boldsymbol{l_1}}\right)^2\right)^{0.5}\right] \tag{5.3}$$

Figures 5.9, 5.10, 5.11, and 5.12 are visual representations of the coefficient fits for

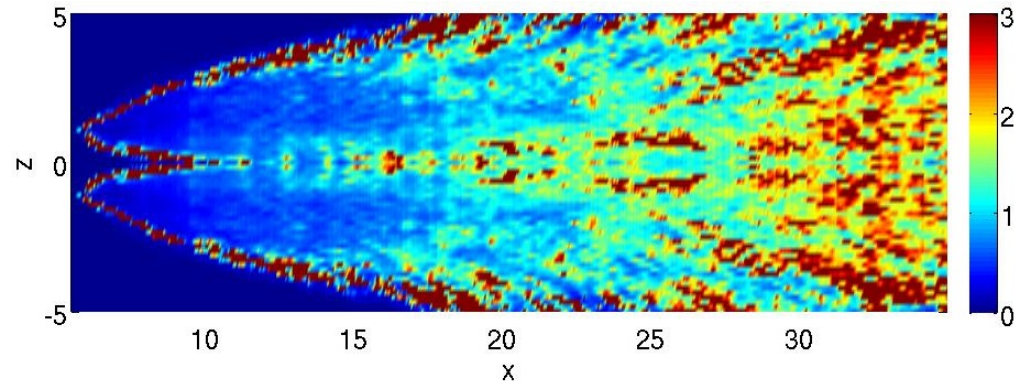

Figure 5.11: Length scale fit for the fixed-frame model ($y = 0$ plane).

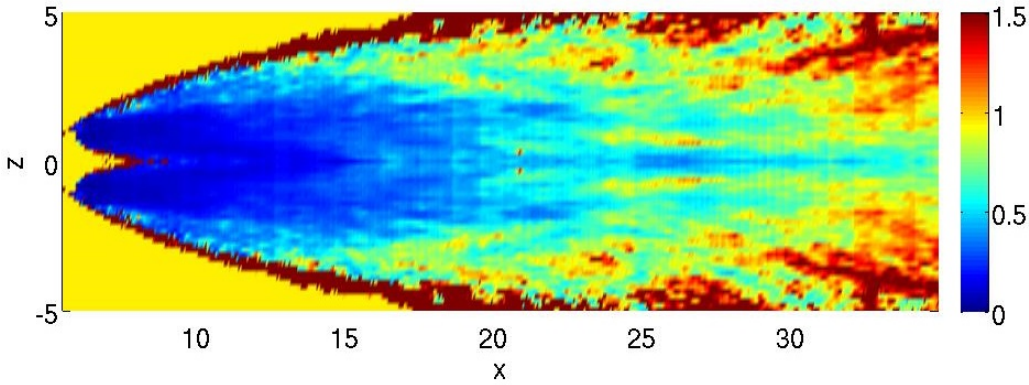

Figure 5.12: Length 0 (l_0) scale fit for the fixed-frame model ($y = 0$ plane).

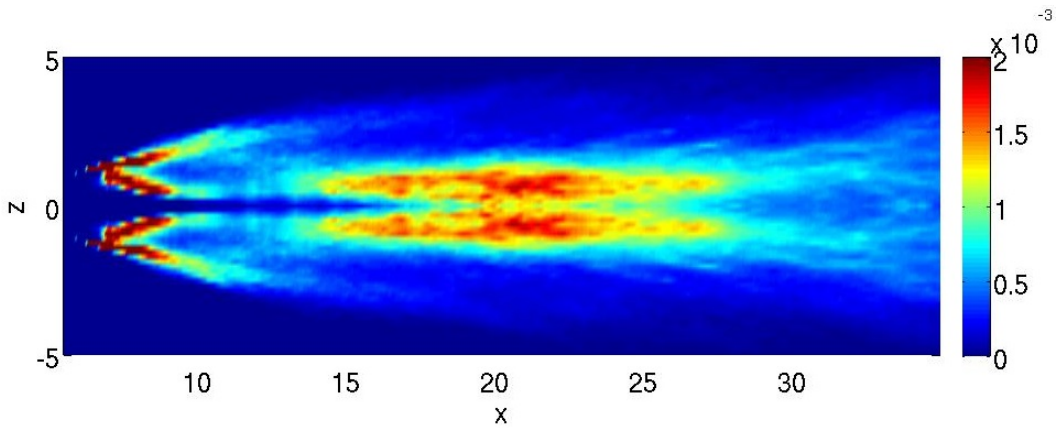

Figure 5.13: Amplitude fit for the modified-distance model ($y = 0$ plane).

the flow field using a fixed-frame model. The coefficient fits capture the gross features of the flow like the previous two models.

5.1.4 Modified-distance model

As shown already in equation 3.32, equation 5.4 is the modified-distance model equation that is used for this thesis with fitting coefficients shown in bold. This model, unlike the others, has five free parameters.

$$R_{ijkl}(\vec{x}, \Delta_1, \tau) = \boldsymbol{A_{ijkl}} exp\left[-\left(\left(\frac{\tau - \frac{\Delta_1}{\widetilde{v_1}}}{\boldsymbol{\tau_s}}\right)^2 + \left(\frac{|\Delta_1|}{\boldsymbol{l_1}}\right)^{\boldsymbol{b_1}}\right)^{0.5}\right] \tag{5.4}$$

Figures 5.13, 5.14, 5.15, 5.16, and 5.17 are visual representations of the coefficient fits for the flow field using a modified-distance model. Unlike the previous three models, the modified-distance model contains a fifth parameter, the peak-decay shape regulator, b_1, which should theoretically allow for a slightly better fit to the data. Figure 5.17 shows that the peak-decay shape regulator, b_1, is between 2 and 3 over most of the flow field. In fact, the modified-distance model is close in form to the moving-frame and fixed-frame models except for the fifth parameter where the other two models have a constant 2. This

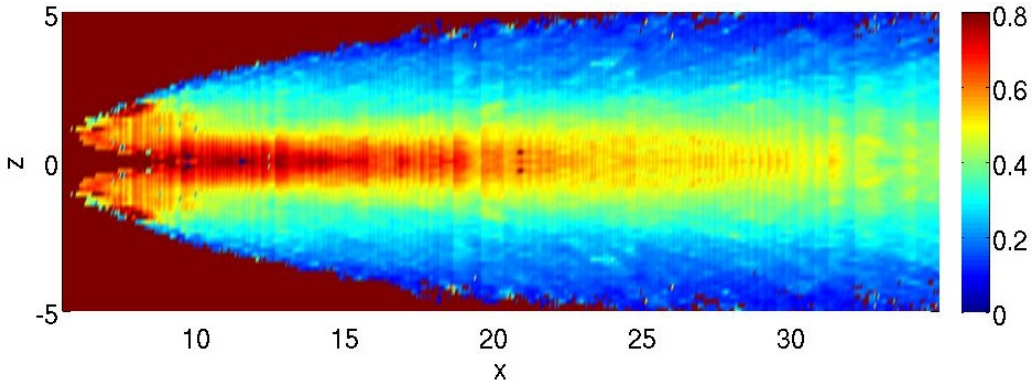

Figure 5.14: Convection velocity fit for the modified-distance model ($y = 0$ plane).

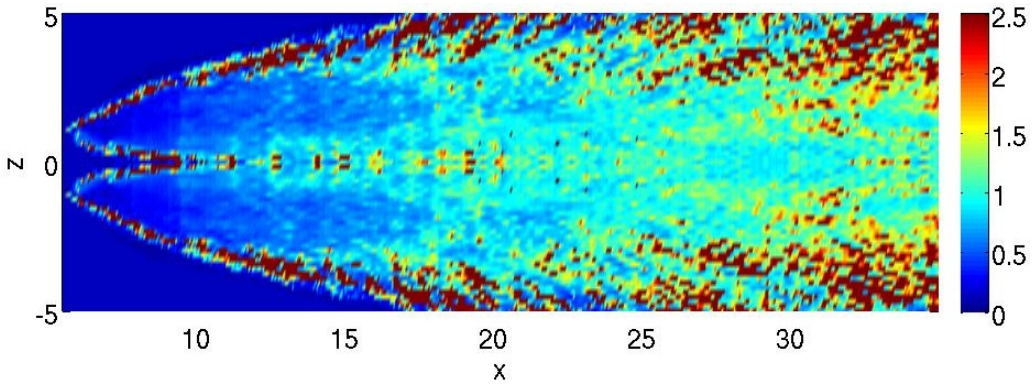

Figure 5.15: Length scale fit for the modified-distance model ($y = 0$ plane).

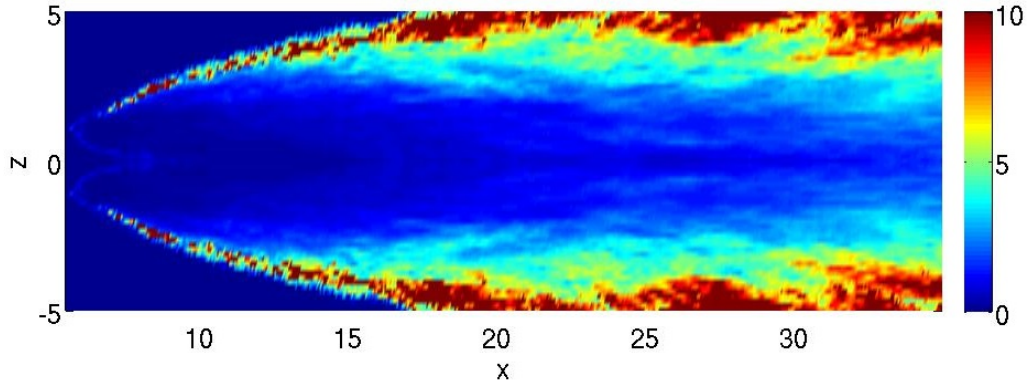

Figure 5.16: Time scale fit for the modified-distance model ($y = 0$ plane).

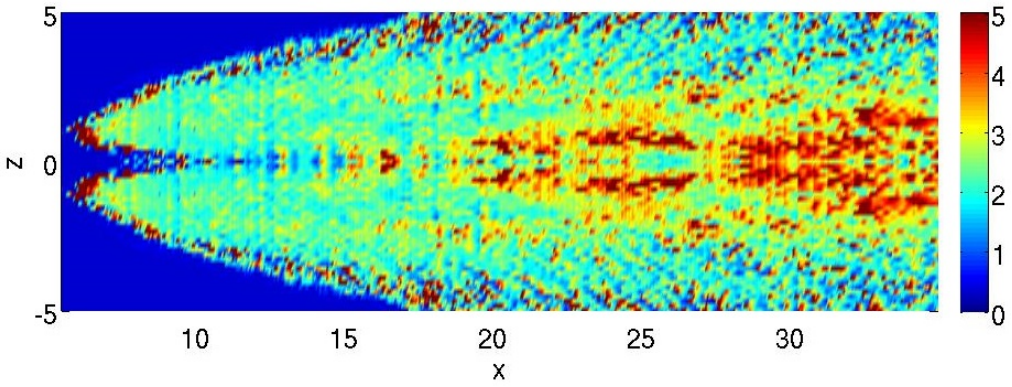

Figure 5.17: Peak-decay shape regulator fit for the modified-distance model ($y = 0$ plane).

explains why the fifth parameter is between 2 and 3 throughout most of the flow field.

5.2 Error analysis

For analyzing the acoustic source model errors, both the $y = 0$ and $z = 0$ planes were analyzed and outputted for all four models. For every error plot, the error is defined as the difference between the source model and the correlation data divided by the square of the amplitude fit of the model. Figure 5.18 represents the error for the Gaussian model. Other than far upstream, the error is pretty significant when using the Gaussian model. Figure 5.19 represents the error for the moving-frame model. The errors are much lower than the Gaussian model. The fixed-frame model error is shown as figure 5.20. The error appears to be about the same as the moving-frame model. Figure 5.21 shows the error plots for the modified-distance model. Once again, the errors appear to be about the same as the moving-frame and fixed-frame models. For all four source models, the error appears to be a little worse for the $z = 0$ plane compared to the $y = 0$ plane.

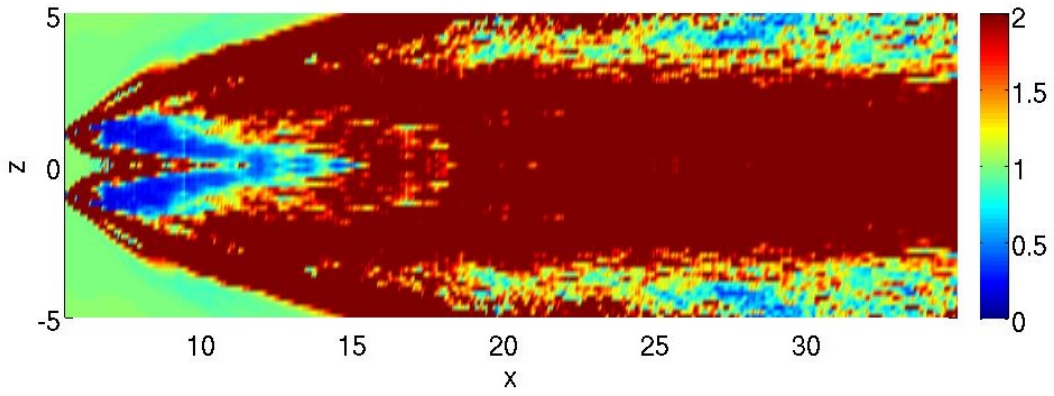

(a) $y = 0$ plane.

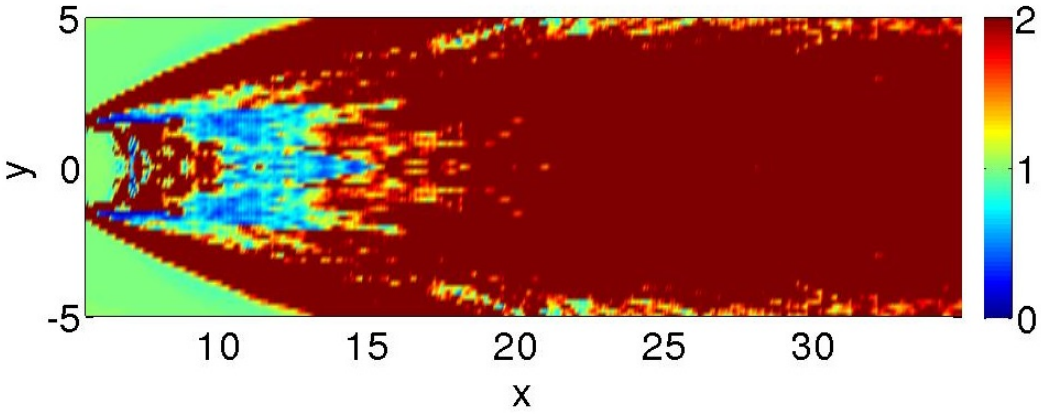

(b) $z = 0$ plane.

Figure 5.18: Error residual between the Gaussian model and R_{1111} correlation data.

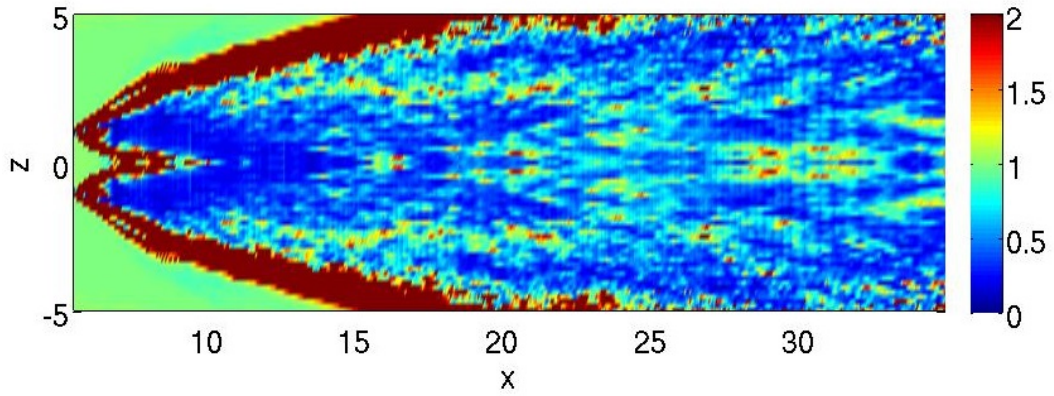

(a) $y = 0$ plane.

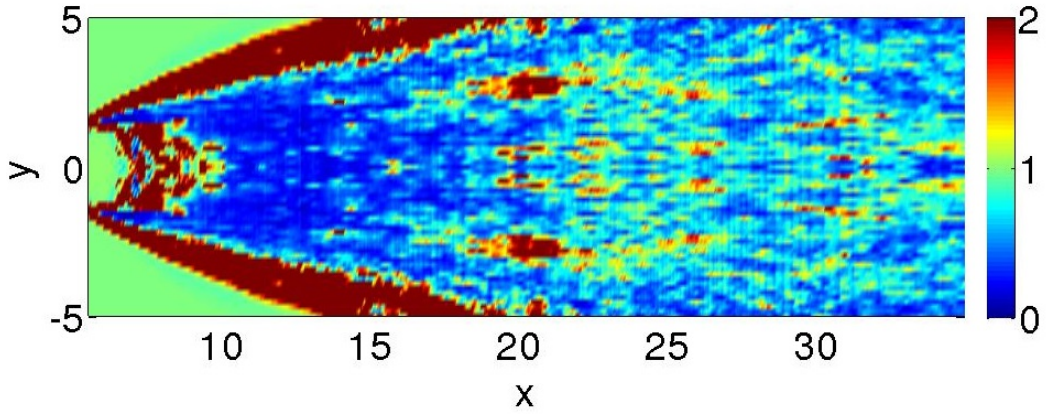

(b) $z = 0$ plane.

Figure 5.19: Error residual between the moving-frame model and R_{1111} correlation data.

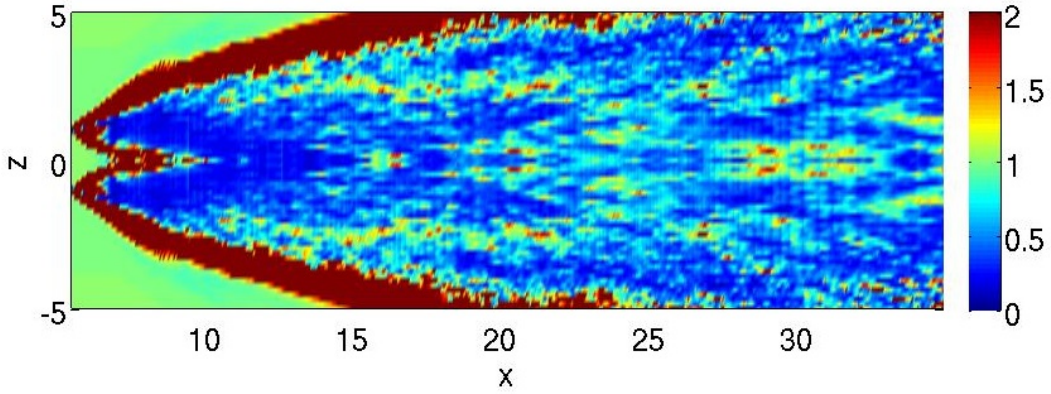

(a) $y = 0$ plane.

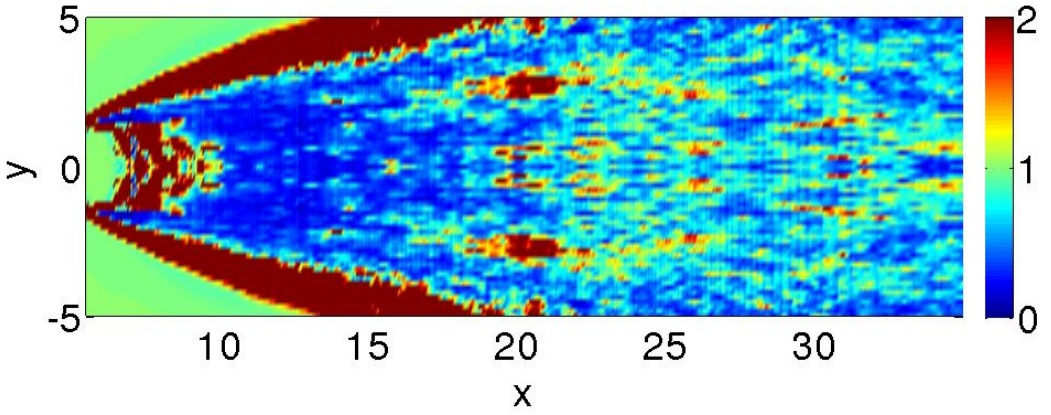

(b) $z = 0$ plane.

Figure 5.20: Error residual between the fixed-frame model and R_{1111} correlation data.

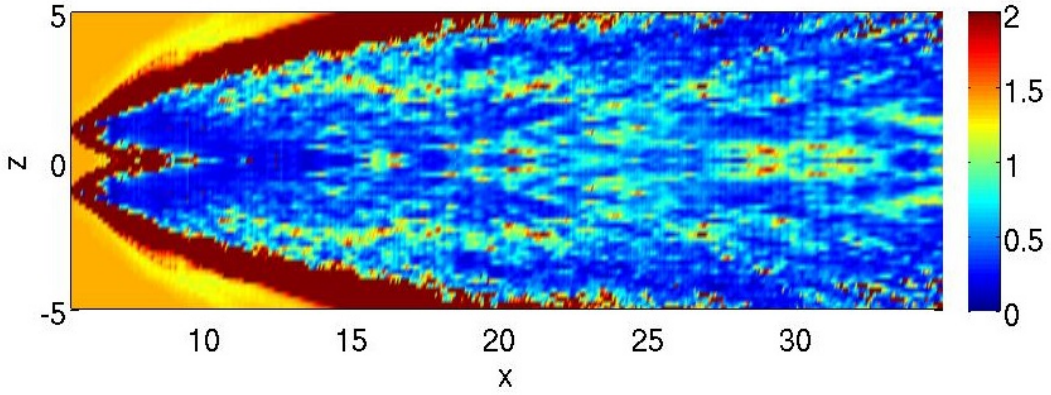

(a) $y = 0$ plane.

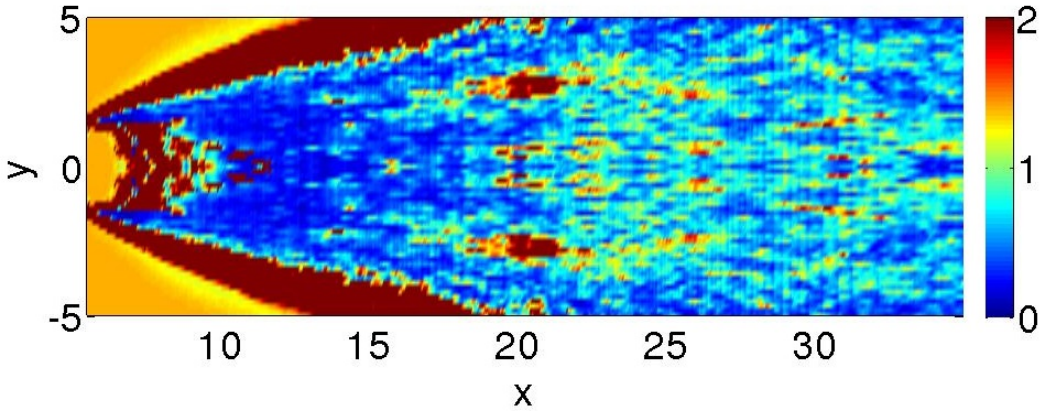

(b) $z = 0$ plane.

Figure 5.21: Error residual between the modified-distance model and R_{1111} correlation data .

5.2.1 Acoustic source model comparisons

The first thing to note from the error plots for all four models is that the Gaussian model is clearly the worst fit to acoustic sources in a rectangular supersonic chevron jet. A primary reason for this observation is that the Gaussian model does not account for the cusp behavior of the correlation values at zero spatial separation. The other models, however, account for this cusp, and hence they are all very similar in modeling accuracy.

As a further study, the $\|error\|_2$ was calculated for each acoustic source model, where $\|error\|_2$ is defined as the L^2 norm of the absolute error between the source model and correlation data. This study was done in a few different ways. At first, the $y = 0$ and $z = 0$ planes were analyzed for error calculations. The results are shown in table 5.1. The Gaussian model's error proves to be the worst in both cases. Also, the other three models are very close in accuracy, with the modified-distance model having the lowest error for both cases. Also, as already seen in the error plots, the $z = 0$ plane contains more error for all four models than the $y = 0$ plane.

For a more detailed study, the entire three dimensional flow field was used for the $\|error\|_2$ calculation for the acoustic source models. The results, also shown in table 5.1, are very similar to the plane analysis with one exception. The modified-distance model no longer has the smallest error. The moving-frame model contains the lowest error. The Gaussian model is still highest in error followed by the modified-distance model. It is important to note that while this is an important study to analyze, it does not fully indicate which source model is best. There are certain areas in the statistical domain where turbulence is nonexistent, and therefore cross correlation data in these areas are meaningless since they reside outside of the actual moving flow field. Certain acoustic source models, particularly the modified-distance model, naturally have higher errors in these areas than others. Hence, this error study could be biased towards certain models with lower errors in these areas. It should be noted though that errors in these areas should

	y = 0 Plane	z = 0 Plane	3D Flow Field
Gaussian	3.4588809375E-04	5.6213490240E-04	0.0025102414
Moving-Frame	1.1647389714E-04	2.1767483099E-04	0.0011098166
Fixed-Frame	1.1647395497E-04	2.1767524039E-04	0.0011253667
Modified-Distance	1.1049319173E-04	2.1296623808E-04	0.0012705751

Table 5.1: L^2 norm of the error for all four acoustic source models.

be very small since these non-turbulent regions have small correlation amplitudes. It is unclear as to how much these errors really contribute to the overall L^2 norm of the error. What can be taken from this study is that the Gaussian model is the worst fit, while the other three models appear to be very close in accuracy.

5.3 Selected points

It is important to show how the different acoustic source models fit the correlation data for selected points in the flow field. The following sections will show how the models fit for single points rather than the entire flow field. For all plots in this section, the dashed lines represent the R_{1111} calculations, while the solid lines represent the acoustic source model. The legend for all of these plots is shown as figure 5.22. Every different color in the plots corresponds to a different spatial offset distance from the main point of interest. Also, for each plot, the horizontal axis is the non-dimensionalized time value of $0.65U_j\frac{dt}{D_e}$. $0.65U_j$ was included in the non-dimensionalizing because it is the typical convection velocity.

5.3.1 Gaussian model

To investigate the accuracy of the Gaussian model, various points in the $y = 0$ plane are considered. These points (A-E in figure 5.23) were chosen to highlight different behavior

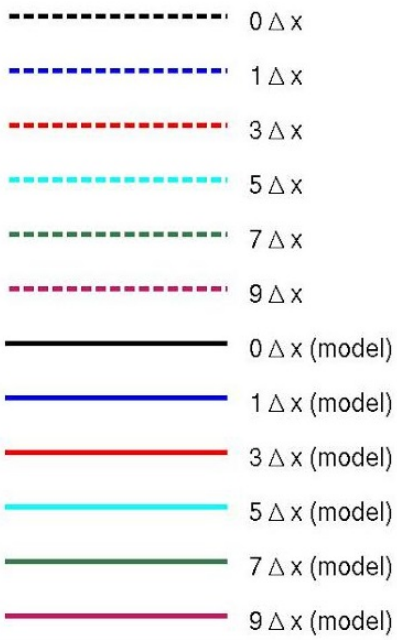

Figure 5.22: Legend for the selected point plots (Length of spatial offsets).

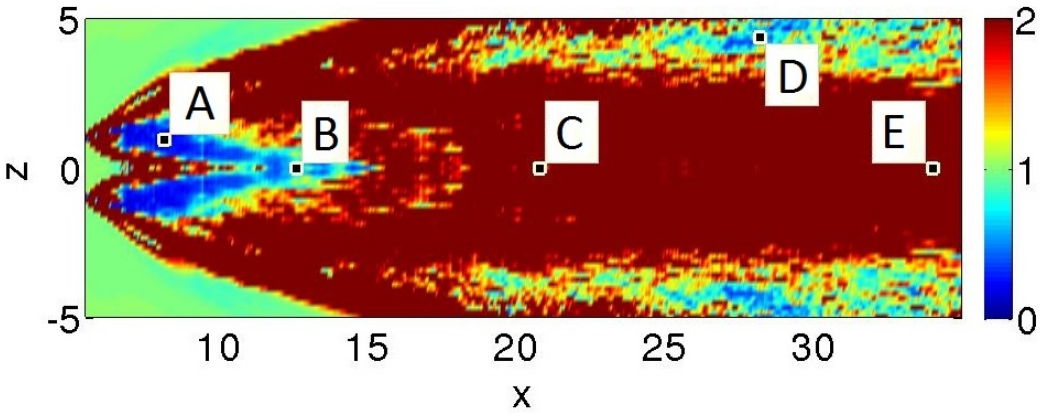

Figure 5.23: Error residual between the Gaussian model and correlation data showing selected points for analysis ($y = 0$ plane).

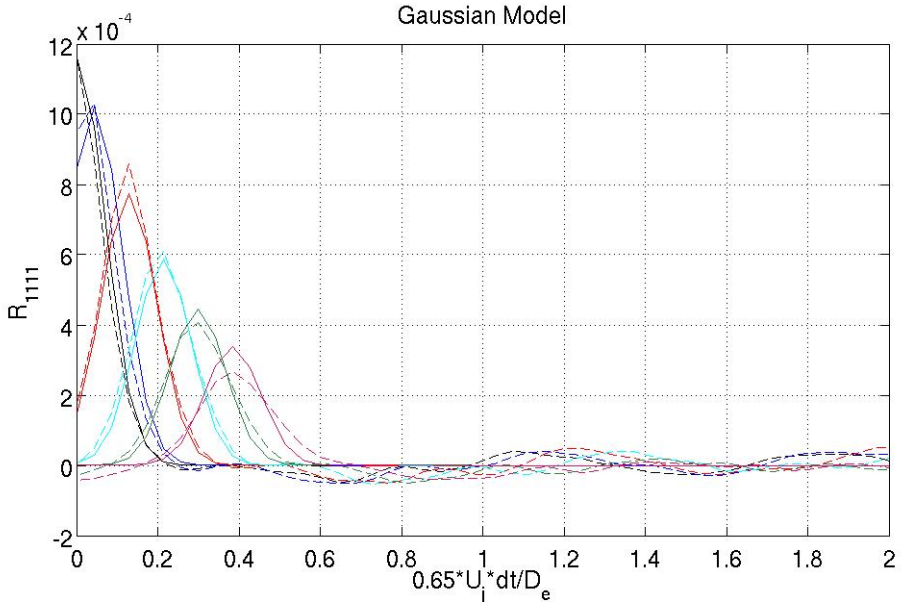

Figure 5.24: Gaussian model (solid lines) fitted to R_{1111} correlation data (dashed lines) for Point A in the flow field.

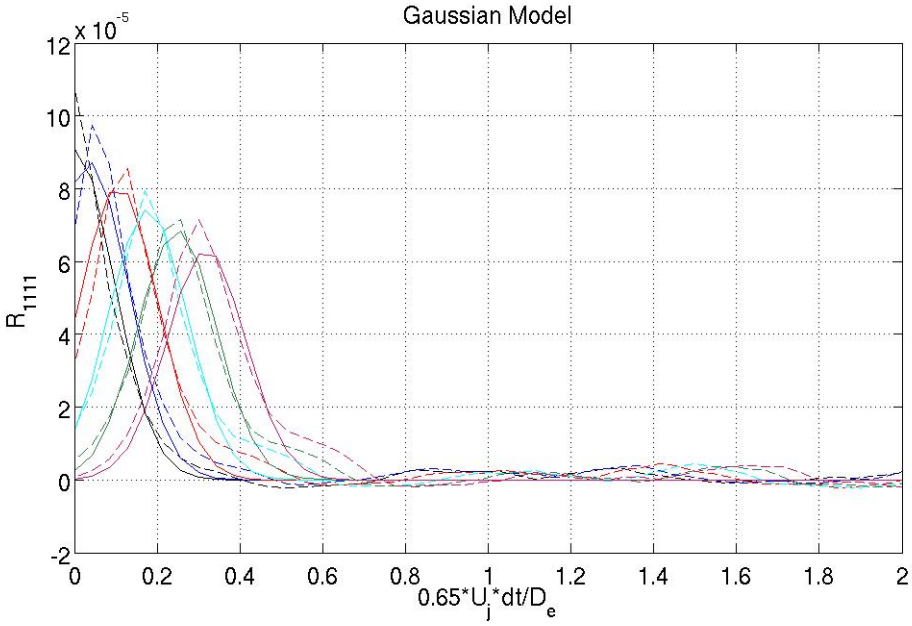

Figure 5.25: Gaussian model (solid lines) fitted to R_{1111} correlation data (dashed lines) for Point B in the flow field.

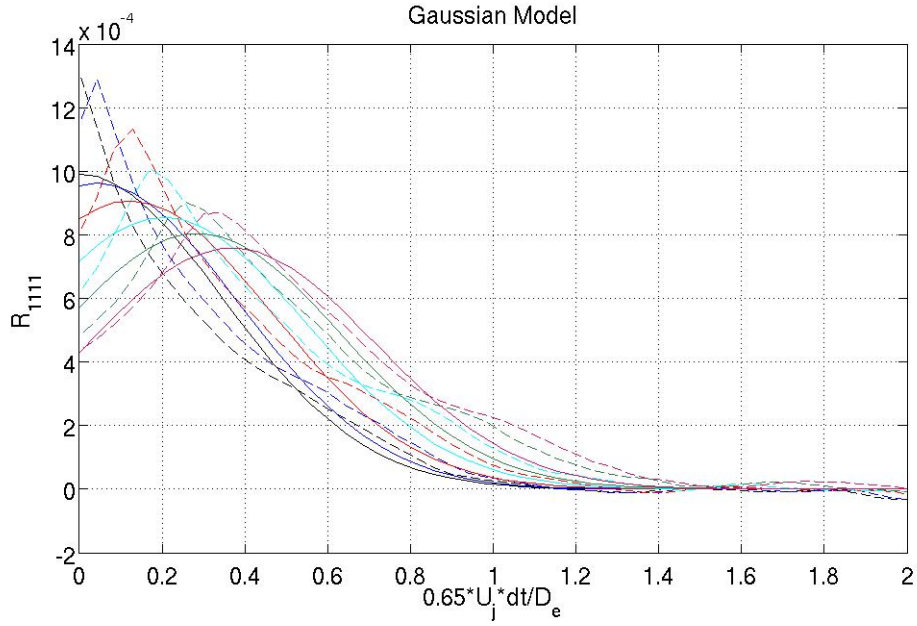

Figure 5.26: Gaussian model (solid lines) fitted to R_{1111} correlation data (dashed lines) for Point C in the flow field.

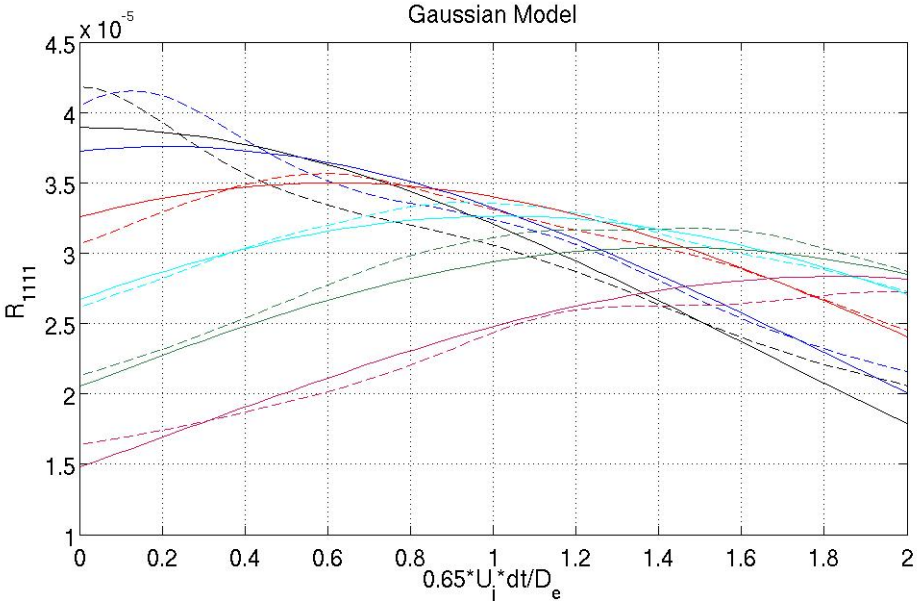

Figure 5.27: Gaussian model (solid lines) fitted to R_{1111} correlation data (dashed lines) for Point D in the flow field.

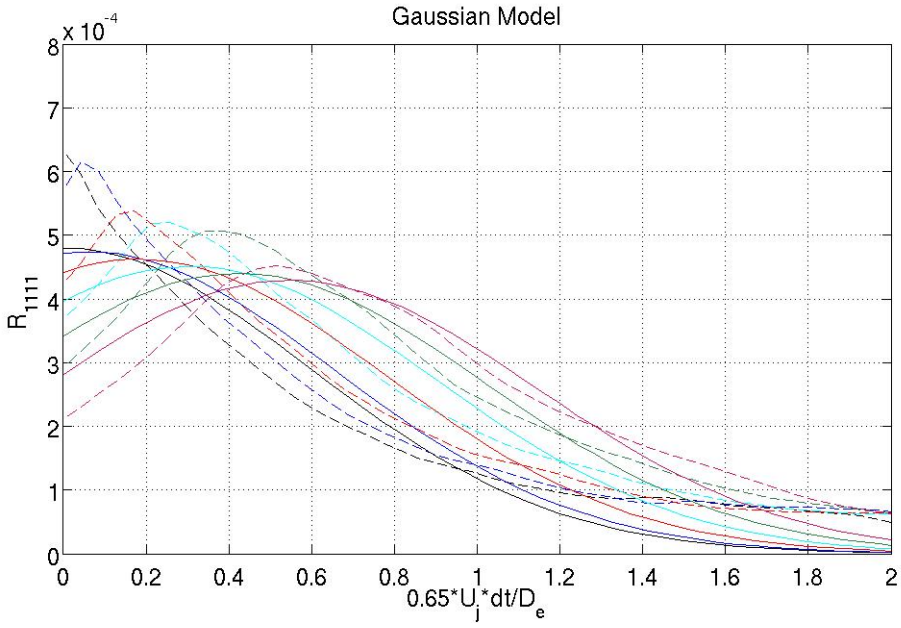

Figure 5.28: Gaussian model (solid lines) fitted to R_{1111} correlation data (dashed lines) for Point E in the flow field.

of the correlation calculations and their respective model fits. It should be noted that while the error in figure 5.23 is divided by the square of the amplitude fit of the model, the selected point plots are not. The first point (Point A) was chosen where the model should be a good fit to the data. Figure 5.24 shows that the Gaussian model fits to Point A in the flow field quite well, although loops of negative correlation are not represented, as expected. The loops of negative correlation are caused by large turbulent structures, which will be discussed in the next chapter. The effect of large turbulent structures can be seen at large time delays because they are responsible for low frequency noise.

An upstream point (Point B) in the center of the jet was chosen to see how the model would fit the data. Figure 5.25 shows the model fit. The Gaussian model fits the data quite well at this location. The amplitude of the R_{1111} data at this location is smaller than the data at Point A. This is because the turbulence is higher at Point A due to strong shear

layers formed by the side jets generated at the nozzle exit. Also, the amplitudes of the spatial offset correlations at Point B do not decay nearly as much for increasing spatial offsets as Point A because the convection velocity is greater at Point B. This means that there is less turbulence decay as the flow goes from Point B to the spatial offset.

A point near the center of the flow field (Point C) was also selected. Figure 5.26 shows the model fit. It can be seen that the model appears to have broken down by Point C in the flow field. The data do not correspond well to the model. Based on figure 5.23, this is no surprise. The Gaussian model appears to underpredict the peaks of the cross correlation data as well as not model the cusp behavior at zero spatial separation.

A downstream point (Point E) was also analyzed. Once again, figure 5.28 shows that the model poorly predicts the data by underpredicting the peaks and failing to model the cusp behavior at zero spatial separation. However, convergence of the R_{1111} values is a concern at this location, so the poor model fit may be partially attributed to that issue. Points B, C, and E are a great representation of the fact that as one moves farther downstream in the flow field, the time and length scales become larger in the flow. Therefore, farther downstream in the flow field, the cross correlation data are more spread out and decay to zero at larger time delays.

As can be seen from figures 5.3 and 5.4, the length and time scales are particularly large downstream near the edges of the flow field. As a visual example, one more point was analyzed near the edge of the flow field (Point D). According to figure 5.23, it is believed to be a good fit. As one can see from figure 5.27, the Gaussian model does in fact fit the data quite well. However, it must be noted that since the time and length scales are so large, the data do not even get close to decaying to zero within the limits of time delay values that were analyzed for this thesis. Therefore, since the model is not fitting to the entire range of possible cross correlation values at this location, the accurate fit seen may not be as accurate if larger time delays were considered. Also, convergence is once

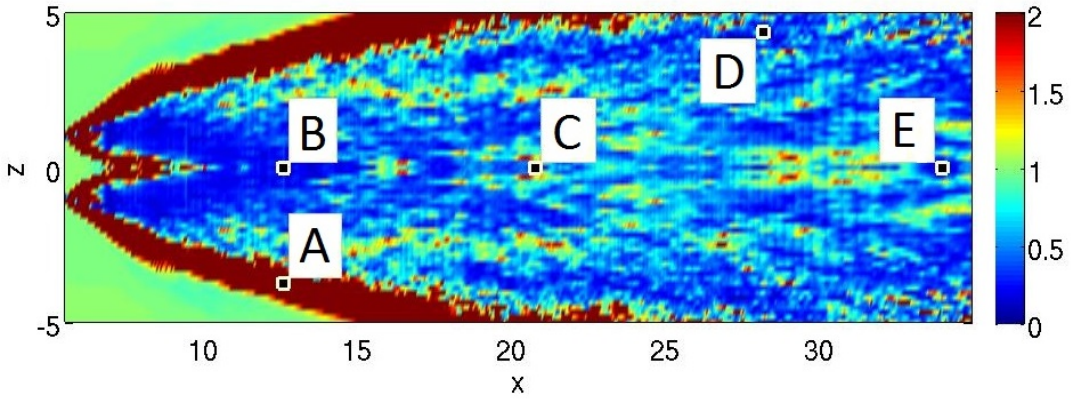

Figure 5.29: Error residual between the fixed-frame model and correlation data showing selected points for analysis.

again an issue at this location, so this model may not be predicting fully converged data.

5.3.2 Fixed-frame model

Figure 5.29 shows where all the analyzed points for the fixed-frame model reside in the flow field. They are labeled as Points A-E. As one can see, these are the exact points that were analyzed for the Gaussian model with the exception of Point A. The Gaussian model analyzed the point **(8.142,0,0.9375)** for Point A to see what an accurate fit looked like with the Gaussian model. For the fixed-frame model, it was necessary to show why the model appears to fail mostly at the edges of the flow field. With this in mind, the point with coordinates **(12.6,0,-3.75)** was chosen for Point A. Figure 5.30 shows the analysis. It is apparent that this point is outside of the moving flow field. This explains the very small R_{1111} values as well as the sporadic nature of the data. The acoustic source models are designed to model turbulence, and since this point is outside of the turbulent regions, the cross correlation data are not meaningful. The model is trying to predict behavior that isn't physically relevant.

Points B-E with the fixed-frame model correspond to the same Points B-E that were

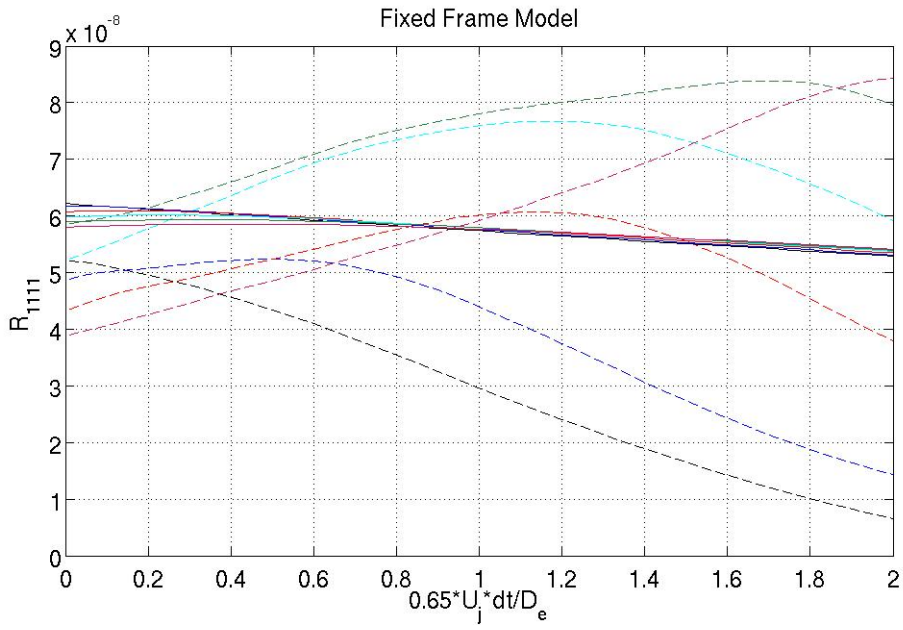

Figure 5.30: Fixed-frame model (solid lines) fitted to R_{1111} correlation data (dashed lines) for Point A in the flow field.

used with the Gaussian model. Figures 5.31, 5.32, 5.33, and 5.34 correspond to Points B-E respectively. The fixed-frame model does an excellent job of accurately modeling the data. As can be seen, the fixed-frame model accounts for the cusp at zero spatial separation. This model also captures the increase in width of the curves as one moves downstream in the flow field. Points D and E should once again be pointed out though for possible R_{1111} convergence errors due to their locations.

5.3.3 Moving-frame and modified-distance model

The moving-frame and modified-distance models are nearly identical in accuracy to the fixed-frame model. Therefore, only Point E, seen from figure 5.29, was analyzed for these two models. The choosing of Point E was purely arbitrary, although there is possible convergence issues at this location. As one can see from figures 5.35 and 5.36, they are

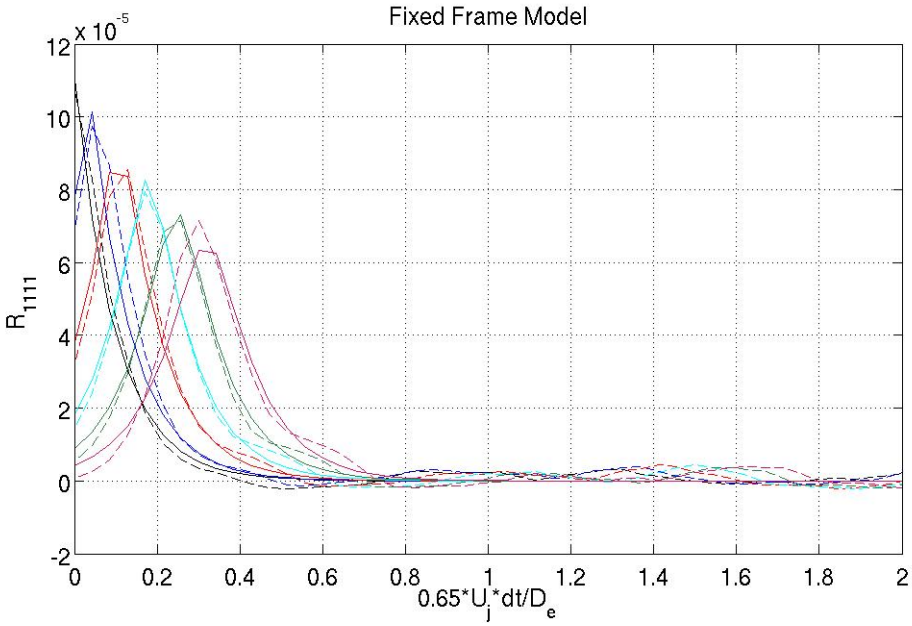

Figure 5.31: Fixed-frame model (solid lines) fitted to R_{1111} correlation data (dashed lines) for Point B in the flow field.

nearly identical to the fixed-frame fit shown in figure 5.34, as expected. It should once again be noted that these two models do not fit the data exactly the same as the fixed-frame model, but all three models are so close in accuracy that the plots look almost identical.

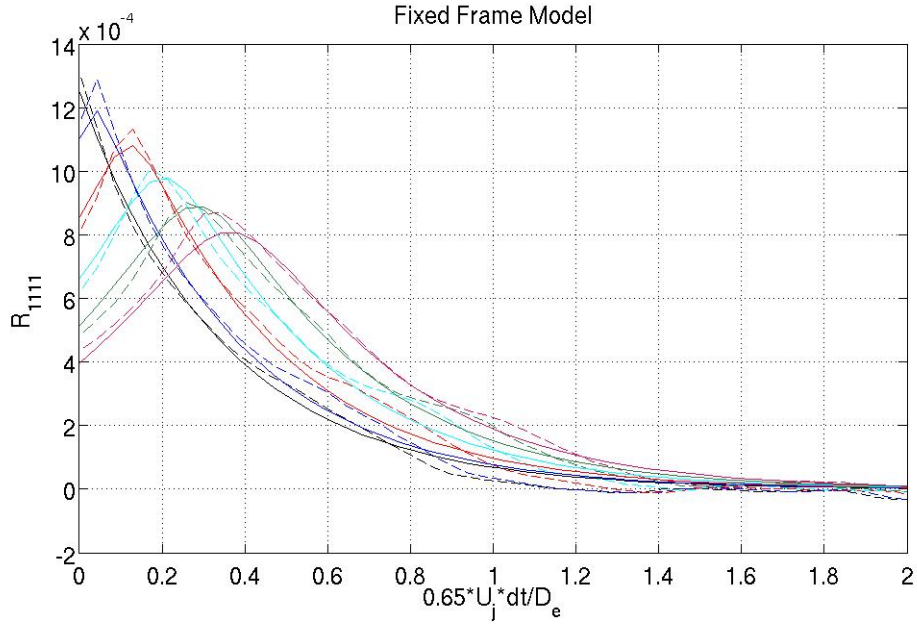

Figure 5.32: Fixed-frame model (solid lines) fitted to R_{1111} correlation data (dashed lines) for Point C in the flow field.

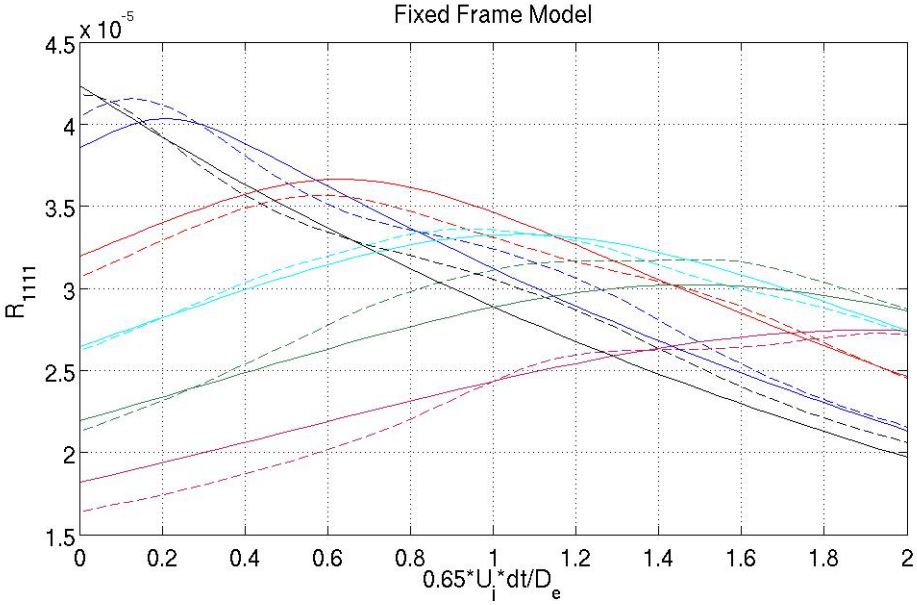

Figure 5.33: Fixed-frame model (solid lines) fitted to R_{1111} correlation data (dashed lines) for Point D in the flow field.

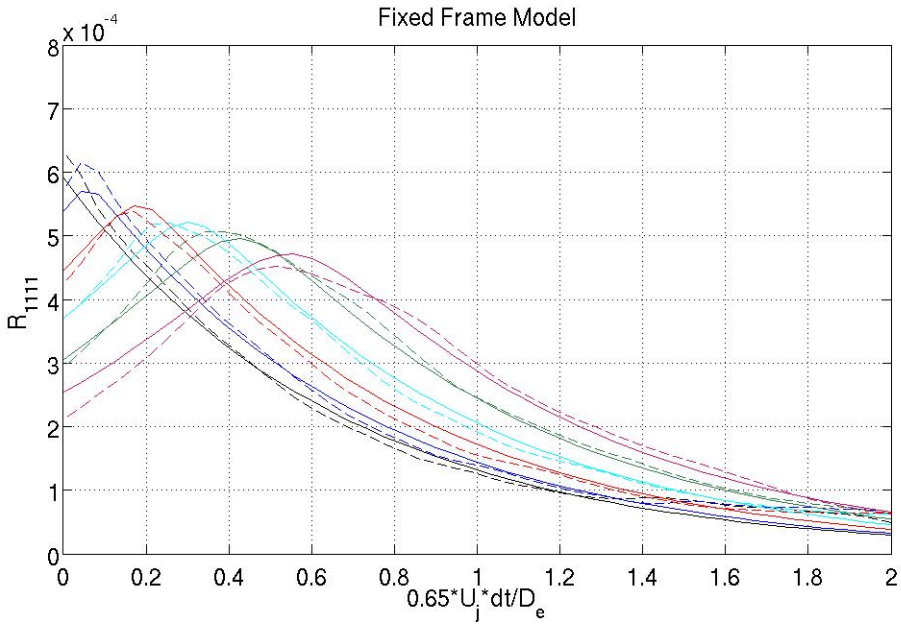

Figure 5.34: Fixed-frame model (solid lines) fitted to R_{1111} correlation data (dashed lines) for Point E in the flow field.

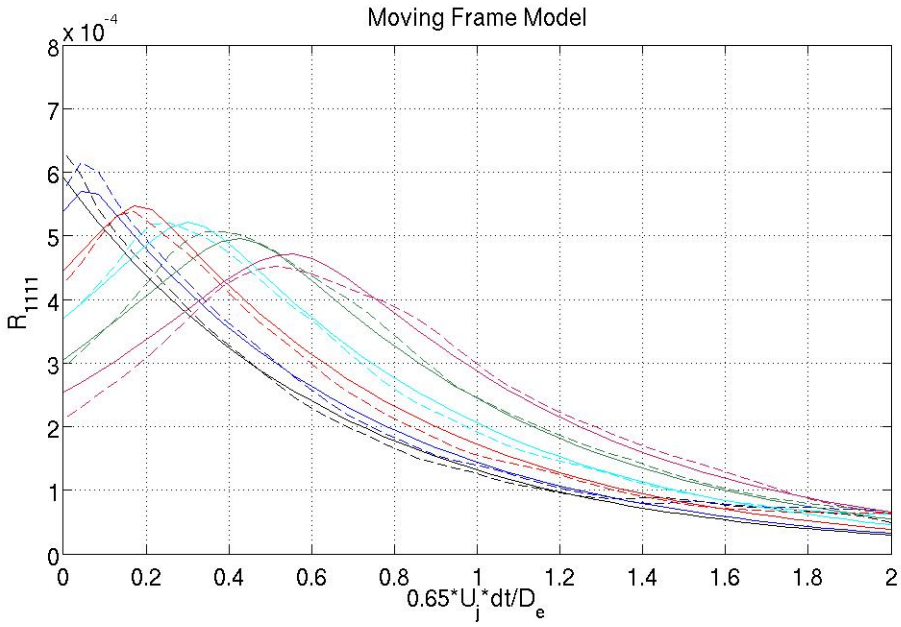

Figure 5.35: Moving-frame model (solid lines) fitted to R_{1111} correlation data (dashed lines) for the coordinate (33.97,0,0).

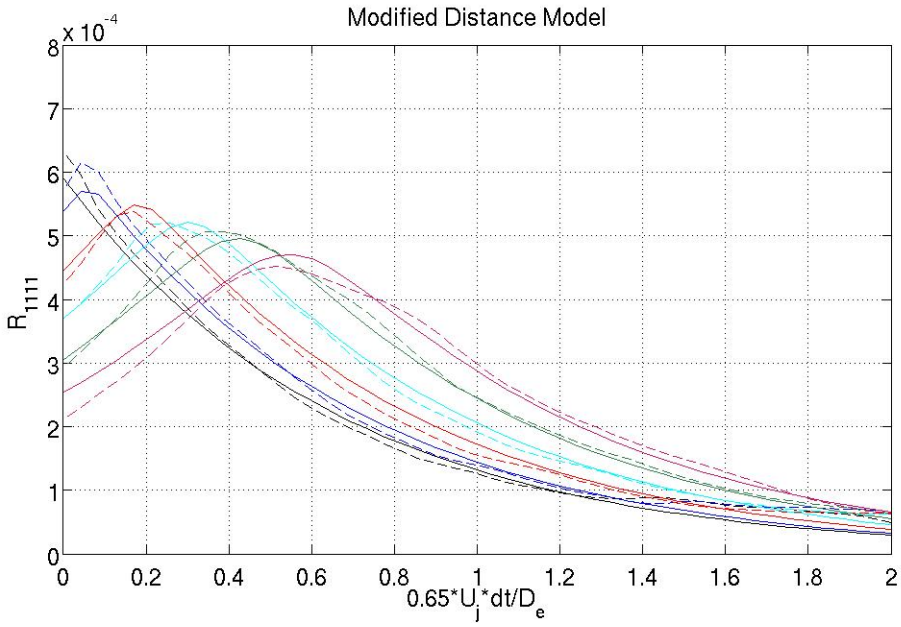

Figure 5.36: Modified-distance model (solid lines) fitted to R_{1111} correlation data (dashed lines) for the coordinate (33.97,0,0).

Chapter 6

Analysis of Large Scale Coherent Structures

While fine-scale turbulence is the focus of this thesis, a brief study was done to analyze large scale turbulent structures in the flow field. These structures are responsible for the loops of negative correlation at large time delays seen in the R_{1111} single point plots of Chapter 5. This means that these structures contribute to low frequency noise. Figures 6.1, 6.3, 6.5, and 6.7 represent Fourier coefficients of the pressure field for Strouhal numbers of 0.0311, 0.0516, 0.1034, and 0.155 for the $z = 0$ plane. The Strouhal numbers are defined as

$$St = \frac{fD_e}{U_j}. \tag{6.1}$$

Coherent periodic structures can be seen for every figure near the edges of the flow field. As the Strouhal number goes up, the large scale coherence becomes more refined, as expected. Figures 6.2, 6.4, 6.6, and 6.8 represent Fourier coefficients of the pressure field for Strouhal numbers of 0.0311, 0.0516, 0.1034, and 0.155 for the $y = 0$ plane. The same type of coherence pattern can be seen at the edges of the flow field for the $y = 0$

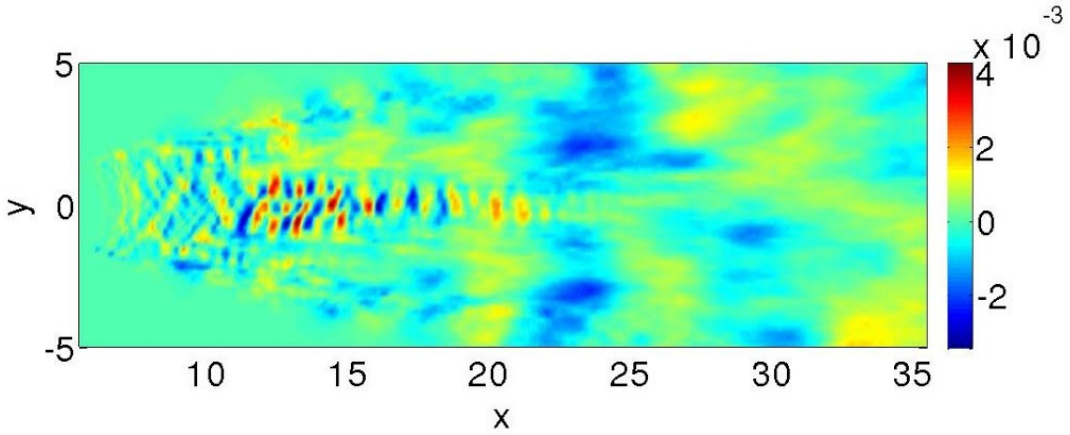

Figure 6.1: Fourier coefficients of the pressure field ($St = 0.0311$) ($z = 0$ plane).

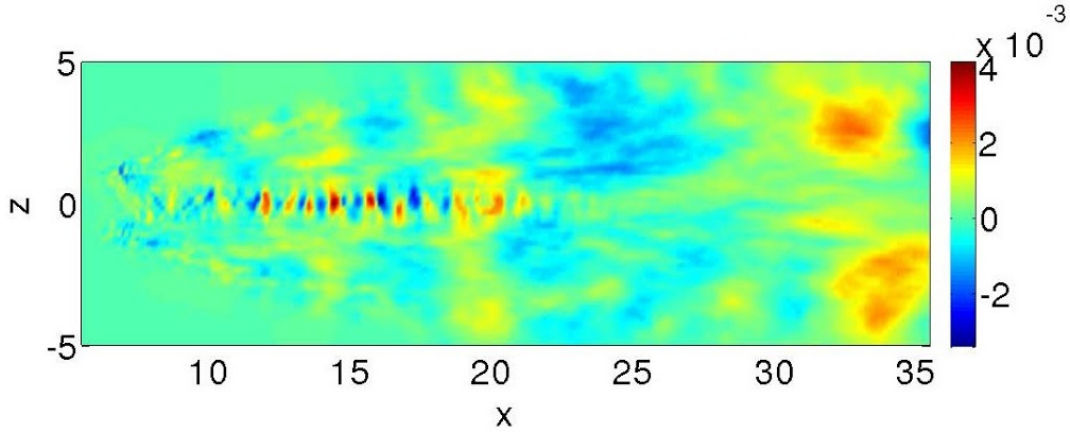

Figure 6.2: Fourier coefficients of the pressure field ($St = 0.0311$) ($y = 0$ plane).

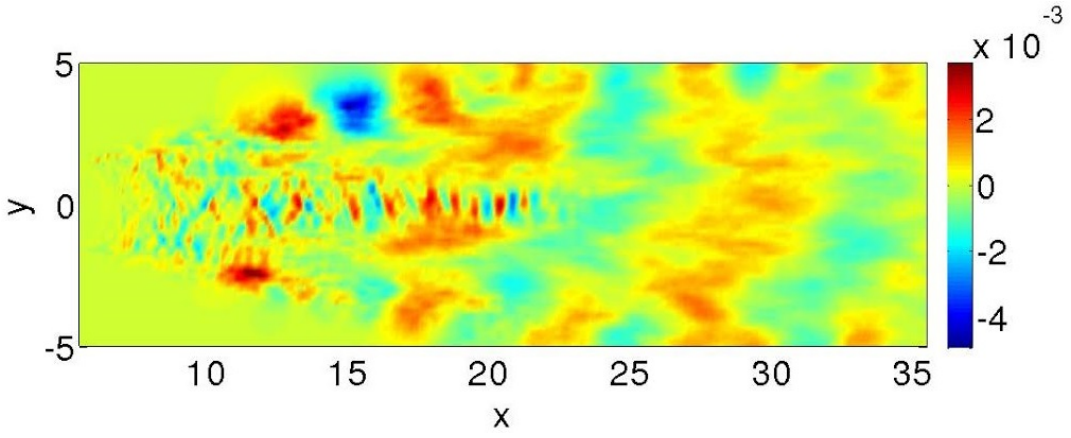

Figure 6.3: Fourier coefficients of the pressure field ($St = 0.0516$) ($z = 0$ plane).

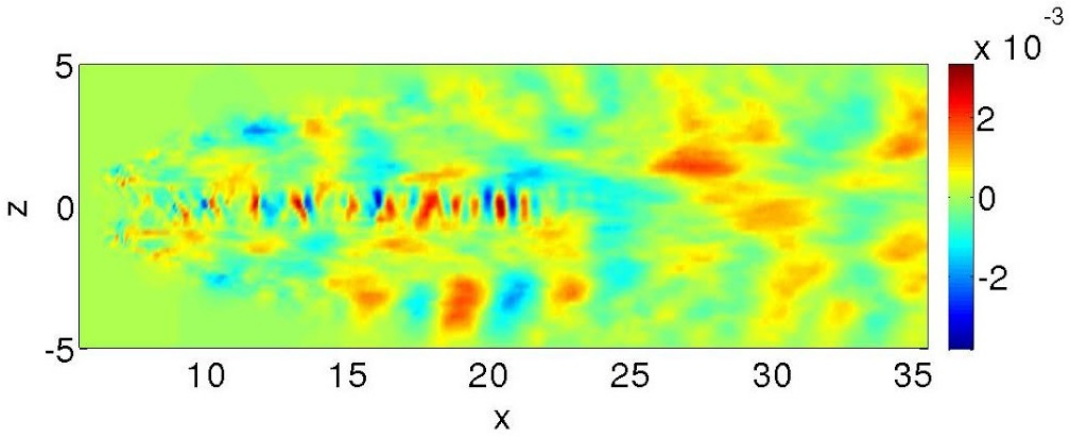

Figure 6.4: Fourier coefficients of the pressure field ($St = 0.0516$) ($y = 0$ plane).

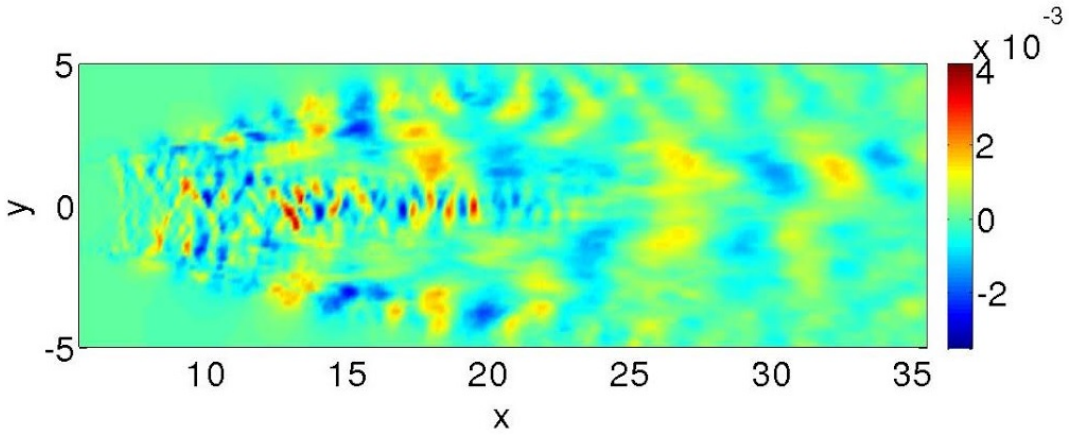

Figure 6.5: Fourier coefficients of the pressure field ($St = 0.1034$) ($z = 0$ plane).

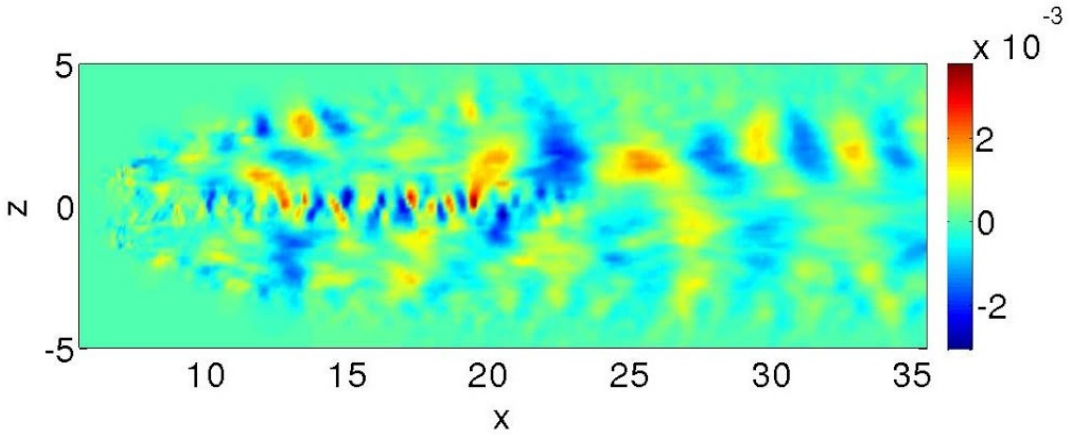

Figure 6.6: Fourier coefficients of the pressure field ($St = 0.1034$) ($y = 0$ plane).

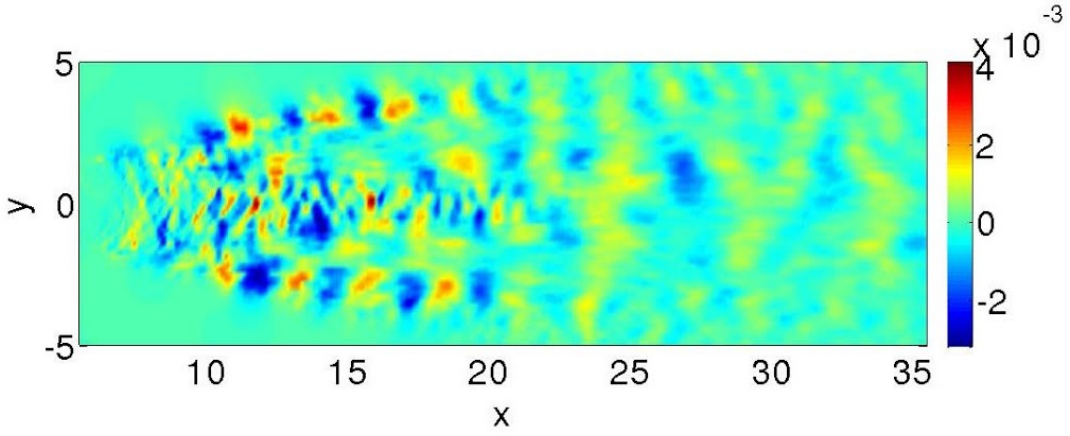

Figure 6.7: Fourier coefficients of the pressure field ($St = 0.155$) ($z = 0$ plane).

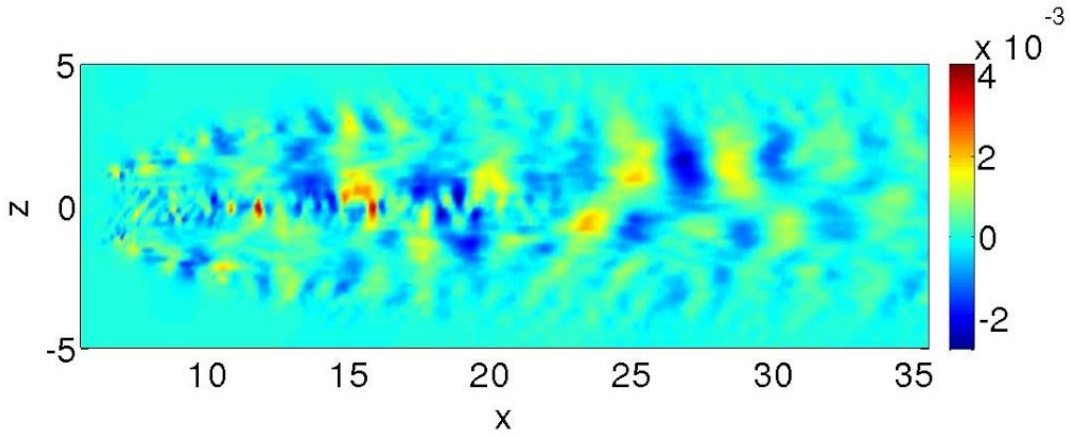

Figure 6.8: Fourier coefficients of the pressure field ($St = 0.155$) ($y = 0$ plane).

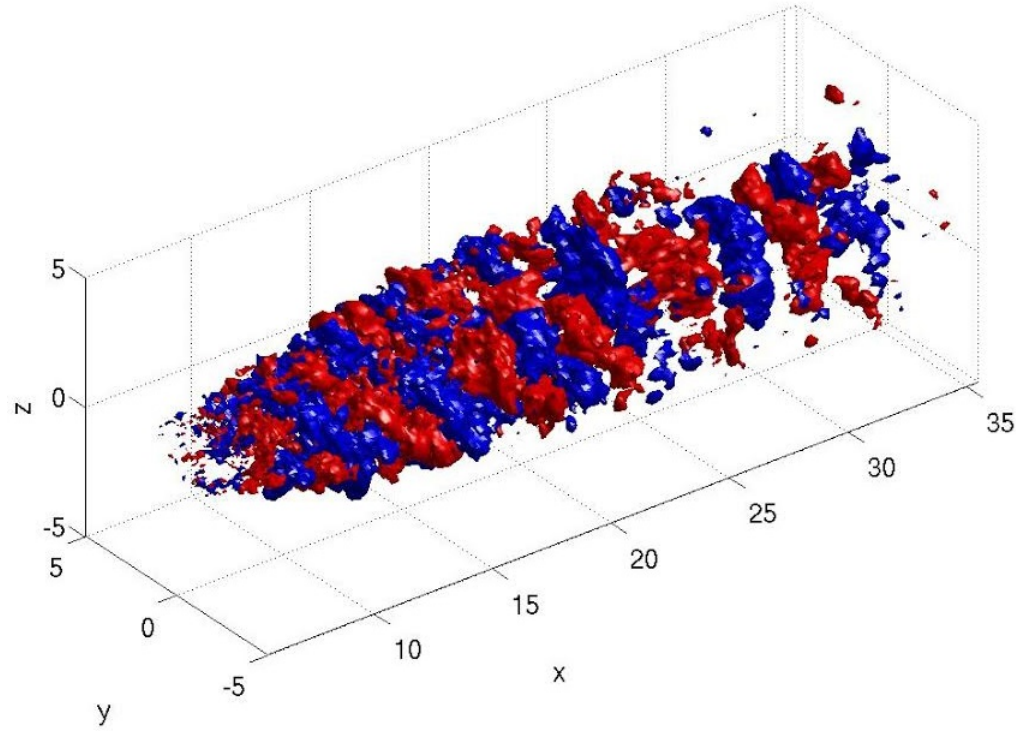

Figure 6.9: Fourier coefficients of +/- 0.0009 for the pressure field ($St = 0.1034$).

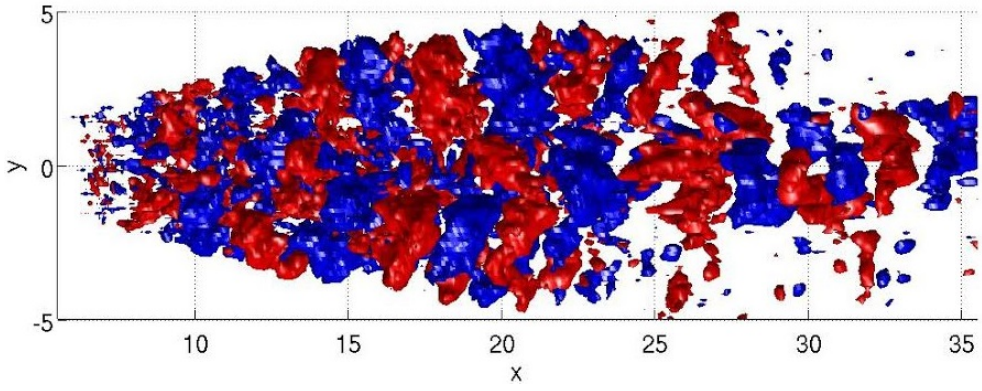

Figure 6.10: Fourier coefficients of +/- 0.0009 for the pressure field ($St = 0.1034$) (XY view).

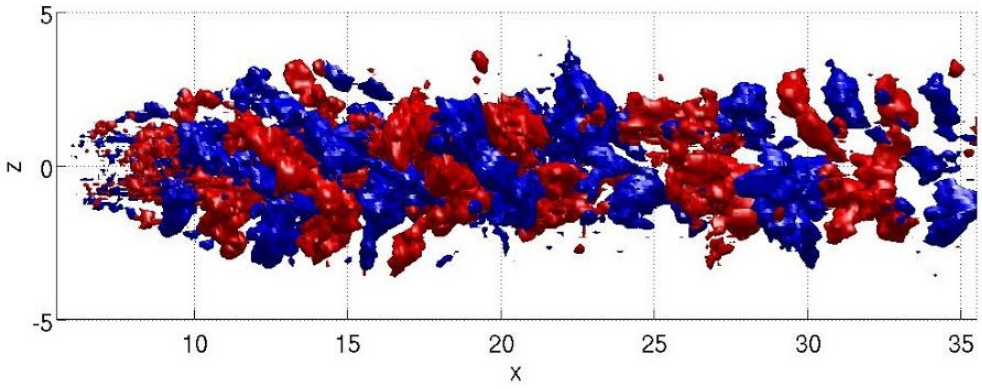

Figure 6.11: Fourier coefficients of +/- 0.0009 for the pressure field ($St = 0.1034$) (XZ view).

plane and the various Strouhal numbers. However, the structures are harder to see and a little less orderly than the $z = 0$ plane.

In order to get a better understanding of what these turbulent structures look like three dimensionally, a three dimensional plot was created for a Strouhal number of 0.1034 with pressure Fourier coefficients of +/-0.0009. The plot is shown as figure 6.9. In order to better see the coherence pattern, figures 6.10 and 6.11 have been included as XY and XZ views respectively. Figure 6.11 is the best view of coherence in the flow field. There is a clear pattern that can be seen in this plot. Therefore, it would appear that this specific complex flow field does have some large scale coherence that would greatly contribute to the sound radiation, particularly downstream due to the nature of large scale turbulent mixing noise [10].

Conclusions

The primary goal of this thesis was to assess the accuracy of acoustic source models in the context of complex nozzle geometry. This thesis extracted and analyzed acoustic source terms from three dimensional data fields generated from a high-fidelity simulation. The simulation was previously validated against experimental acoustic measurements [2]. We further validated the data against PIV turbulence measurements and verified that the data matched Kolmogorov's $\frac{-5}{3}$ law through a spectral analysis.

With the single point quasi-normality study in mind, the scaling factor was found to be 1.72. This is not the theoretical 2, but was used to test turbulence shapes between second and fourth order statistics for all three spatial directions to see if it minimized the error for all three. This study showed similar turbulence shapes between the second and fourth order statistics. However, the two-point quasi-normality study, using 1.7 as the scaling factor, did not display the same turbulence shapes between second and fourth order statistics. While downstream convergence issues may have played a role in this case, there is still significant error between second and fourth order statistics. Since the two-point quasi-normality study did not prove the flow to be fully quasi-normal, the next step was to calculate scaling factors based on the transverse statistics. This was done to see if the flow is quasi-normal in specific directions rather than fully quasi-normal. This study showed that these specific transverse scaling factors were in the range of 1.9-2. Since these are much closer to the theoretical value of 2, we turned to the conclusion that the transverse spatial components of the flow are quasi-normal while the axial direction is

not. To further test this, the PDF's of two points for all three velocity components were calculated. The conclusion was that the skewness of the data in the transverse directions is much smaller compared to the axial direction. Therefore, the highly Gaussian transverse velocity data means that the transverse directions are quasi-normal, while the axial direction is not.

The flow field was initially found to be locally statistically axisymmetric in most locations except far upstream where side jets, caused by the underexpansion of the flow and the use of chevrons, cause highly three dimensional effects. However, directly calculating the validity of the identity $R_{2222} = R_{3333}$ showed a slightly different result. It showed differences between the two values on the order of the correlation values themselves, particularly near the center line and upstream of the flow field. The residual was very low away from the center line though as they were in the first study. Therefore, it can be reasonably concluded that closer to the edges of the flow field, the flow can be trusted to be locally statistically axisymmetric.

With regard to two-point, two-time correlation statistics, the Gaussian acoustic source model provides the worst fit to the correlation data for a rectangular supersonic chevron jet. This is partially due to the inability of the model to accurately model the cusp behavior of the cross correlation data at zero spatial separation. The moving-frame, fixed-frame, and modified-distance models are all about the same in modeling accuracy. Any of these three models would be a suitable choice for modeling acoustic sources from this type of flow field. A selected point analysis was also done to see how each source model fit to a specific point. This study was very telling. For one, it showed that the Gaussian model consistently underpredicts the peaks of the R_{1111} data as well as inaccurately models the cusp at zero spatial separation. All four models correctly predict the enlargement of time and length scales farther downstream by modeling the increase in width of the correlation curves. The study also showed that the accuracy of the source models near the edges

and downstream of the flow should be taken with a bit of skepticism. The large time and length scales at these locations produce R_{1111} data sets that are not complete within the length of time delays analyzed in this thesis.

A study was done to see how much statistics would change if density and Favre averages were not included in the calculations. It was found that a basic time averaged velocity was not much different than a Favre averaged velocity. However, as the order of the statistic went up, the lack of density use in the calculations caused the differences to propagate and became significant, especially for the R_{ijkl} term where the percent difference reached up to 25%. Therefore, for this compressible flow field, the use of density and Favre averages produces a much different result for R_{ijkl} than if basic time averages were assumed.

A brief analysis was done with the purpose of determining if there are large scale turbulent structures in the flow field. If so, these can be large contributors to sound radiation particularly in the downstream directions. The R_{1111} correlation curves had already suggested the existence of large scale turbulent structures from the loops of negative correlation at large time delays. A study analyzing both the $y = 0$ and $z = 0$ planes showed that coherent turbulent structures do exist in the flow. A spatial periodicity of pressure Fourier coefficients can be seen at the edges of the flow field. In addition to center plane analysis, a three dimensional calculation of the pressure Fourier coefficients was performed. In this case, the periodic behavior was harder to see, but there were still large turbulent structures seen in the flow. Therefore, it is believed that while this thesis was primarily concerned with fine-scale turbulence, large scale turbulent structures also exist in this flow and therefore are primary mechanisms of sound.

There is still a lot more that can be accomplished by analyzing this flow field. While this thesis was primarily concerned with the effects of fine-scale turbulence, a further analysis of the large scale turbulent structures as well as shock generated noise would

give a more complete description on the mechanisms of noise in this flow. Also, while three dimensional plots were analyzed, center planes were the primary focus of this thesis, so it would most certainly be beneficial to analyze additional planes in the flow field as well as more three dimensional statistical fields. Analyzing larger time delays for the correlation calculations would also be beneficial in order to better understand the behavior of the acoustic sources far downstream and towards the edges of the flow field. While we have characterized the acoustic sources embedded in a complex jet, to obtain a better understanding of the effect of model choice on the farfield predicted sound, these acoustic source models should be convolved with an adjoint Green's function. Also, it could be beneficial to perform the same analysis done in this thesis but for a rectangular jet without chevrons. It very well could give a better understanding of the chevron jet itself.

Bibliography

[1] F.C. Frate and J.E. Bridges. Extensible rectangular nozzle model system. In *AIAA Paper 2011-975*, 2011.

[2] J.W. Nichols, S.K. Lele, P. Moin, F.E. Ham, and J.E. Bridges. Large-eddy simulation for supersonic rectangular jet noise prediction: effects of chevrons. In *AIAA Paper 2012-2212*, 2012.

[3] J. Bonet and J. Peraire. An alternating digital tree (ADT) algorithm for 3D geometric searching and intersection problems. *International Journal for Numerical Methods in Engineering*, 31:1–17, 1991.

[4] Gp Capt Md Abdus Salam, Gp Capt Nc Chattopadhyay, Md Jalal, Uddin Rumi, and HEM Zahidul Islam Eunus. A review on jet noise reduction. *Journal of Modern Science and Technology*, 1(1), 2013.

[5] Naval research advisory committee report on jet engine noise reduction. Technical report, April 2009.

[6] M.J. Lighthill. On sound generated aerodynamically II. Turbulence as a source of sound. *Philosophical Transaction of the Royal Society of London A*, 222:1–32, 1954.

[7] Y. Khalighi, J.W. Nichols, F. Ham, S.K. Lele, and P. Moin. Unstructured Large Eddy

Simulation for Prediction of Noise Issued from Turbulent Jets in Various Configurations. In *AIAA/CEAS Aeroacoustics Conference*, 2011.

[8] C.K.W. Tam and P. Chen. Turbulent Mixing Noise from Supersonic Jets. *AIAA Journal*, 32(9), September 1994.

[9] C.K.W Tam. Supersonic jet noise. *Annual Review of Fluid Mechanics*, 27, 1995.

[10] C.K.W Tam, M. Golebiowski, and J.M. Seiner. On the two components of turbulent mixing noise from supersonic jets. In *AIAA Paper 96-1716*, 1996.

[11] U. Paliath and P.J. Morris. Prediction of Jet Noise From Rectangular Nozzles. In *AIAA Paper 2006-618*, 2006.

[12] C.K.W. Tam. Influence of Nozzle Geometry on the Noise of High-Speed Jets. *AIAA Journal*, 36(8), August 1998.

[13] C.K.W. Tam and K.B.M.Q. Zaman. Subsonic Jet Noise from Nonaxisymmetric and Tabbed Nozzles. *AIAA Journal*, 38(4), April 2000.

[14] C.K.W. Tam and L. Auriault. Jet Mixing Noise from Fine-Scale Turbulence. *AIAA Journal*, 37(2), February 1999.

[15] P.J. Morris and F. Farassat. Acoustic Analogy and Alternative Theories for Jet Noise Prediction. *AIAA Journal*, 40(4), April 2002.

[16] Mohammed Z. Afsar, Sergey A. Karabasov, Tom P. Hynes, Ann P. Dowling, and Elena de la Rosa Blanco. Jet noise modelling using an acoustic analogy. In *West-East High Speed Flow Field Conference*, 2007.

[17] S.A. Karabasov, M.Z. Afsar, T.P. Hynes, A.P. Dowling, W.A. McMullan, C.D. Pokora, G.J. Page, and J.J. McGuirk. Jet Noise: Acoustic Analogy Informed by Large Eddy Simulation. *AIAA J.*, 48(7):1312–1325, 2010.

[18] S.A. Karabasov, X. Hao, O. Graham, T.P. Hynes, P.G. Tucker, and A.P. Dowling. Low-order modelling for chevron jet noise based on LES data. In *AIAA Paper 2010-3964*, 2010.

[19] S.A. Karabasov, M.Z. Afsar, T.P. Hynes, A.P. Dowling, W.A. McMullan, C.D. Pokora, G.J. Page, and J.J. McGuirk. An investigation of the mechanisms of sound generation in initially laminar subsonic jets using the Goldstein acoustic analogy. *J. Fluid Mech.*, 714:24–57, 2013.

[20] M.E. Goldstein and S.J. Leib. The aero-acoustics of slowly divering supersonic jet flows. *J. Fluid Mech.*, 600:291–337, 2008.

[21] S.J. Leib and M.E. Goldstein. Hybrid Source Model for Predicting High-Speed Jet Noise. *AIAA J.*, 49(7):1324–1335, July 2011.

[22] M. Harper-Bourne. Jet noise turbulence measurements. In *AIAA Paper 2003-3214*, 2003.

[23] A. Bassetti and C.L. Morfey. Impact of the source-correlation model in jet-noise prediction by acoustic analogy. In *AIAA Paper 2007-3604*, 2007.

[24] A. Bassetti and J.W. Nichols. Analysis of LES for source modeling in jet noise. In *AIAA Paper 2014-2905*, 2014.

[25] M.J. Lighthill. On sound generated aerodynamically I. General theory. *Philosophical Transaction of the Royal Society of London A*, 211(1107):564–587, 1952.

[26] M.E. Goldstein. A generalized acoustic analogy. *J. Fluid Mech.*, 488:315–333, 2003.

[27] P. Kundu, I. Cohen, and D. Dowling. *Fluid Mechanics*. Academic Press, fifth edition, 2012.

[28] M.Z. Afsar, J.J. McGuirk, and C.D. Pokora. Statistical axi-symmetry of the two-point time-delayed Reynolds stress auto-covariance tensor for jet noise modelling. In *9th Polish Fluids Mechs. Conf. Paper*, Poznan, Poland, 2010.

[29] A. Monin and A. Yaglom. *Statistical Fluid Mechanics: Mechanics of Turbulence*, volume 2. MIT Press, originally published in 1965 by Nauka Press, Moscow, 1975.

[30] R. Mani et al. High velocity jet noise source location and reduction-task 2. Technical report, FAA-RD-76-79-II, 1977.

[31] J. Jeong and F. Hussain. On the identification of a vortex. *J. Fluid Mech.*, 285:69–94, 1995.

[32] S.K. Robinson. Coherent motions in the turbulent boundary layer. *Annual Review of Fluid Mechanics*, 23:601–639, 1991.

[33] S.B. Pope. *Turbulent Flows*. Cambridge University Press, 2000.

[34] M. Frigo and S.G. Johnson. The Design and Implementation of FFTW3. *Proc. IEEE*, 93(2):216–231, 2005.

[35] S.A. Karabasov, M.Z. Afsar, T.P. Hynes, A.P. Dowling, W.A. McMullan, C.D. Pokora, G.J. Page, and J.J. McGuirk. Using large eddy simulation within an acoustic analogy approach for jet noise modelling. In *AIAA Paper 2008-2985*, 2008.

Appendix A

Preliminary work and pressure derivation

A.1 Preliminary work on a coarse grid

Before analyzing the data outputted from the 528 million control volume simulation, a 6 million control volume simulation was analyzed to initially troubleshoot the correlation calculations. This ensured the accuracy of the calculations before they were applied to the refined data. The Argonne National Laboratory's Cetus machine was used to run through this coarse simulated data in parallel while calculating the R_{1111} term. Figure A.1(a) is the result of this study. Spatial offsets both to the left and right of the analyzed point were used. The R_{1111} values are normalized by the R_{1111} value at zero spatial separation and time delay. The simulated flow field solution from the coarse grid was also not fully converged, so figure A.1(a) reflects that fact somewhat. Some basic expected trends are seen though. Peaks of the data with spatial separations are shifted and decayed compared to the zero spatial separation solution. Also, all solutions decay to zero as time delays are increased. This was a promising step toward the actual goal of calculating cross

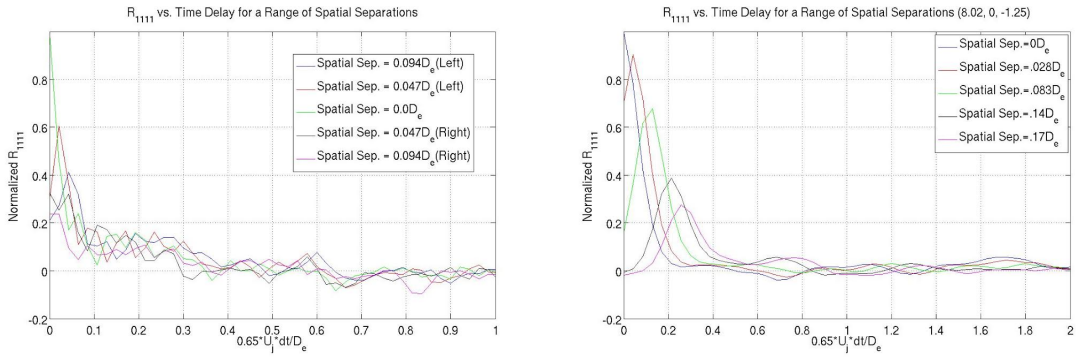

(a) 6 million CV's.

(b) One pass eqn.

Figure A.1: R_{1111}.

correlation values with data found from the full 528 million control volume flow field solution.

A.2 The single pass cross correlation equation

The original process with the extracted mesh off the 528 million control volume grid was trying to run through all of the data in one pass instead of the final determined three pass system. To accomplish this goal, the equation for the R_{1111} term was expanded to include only averages. This way, all averages were calculated in one pass and then plugged into equation A.1. With regard to equation A.1, the subscript 1 refers to a given point in the flow field, while subscript 2 refers to its spatial offset point. For the velocities, the first subscript represents direction, and the second subscript represents whether it is the point of interest (1) or its spatial offset (2).

$$
\begin{aligned}
R_{1111} = \\
&\overline{\rho_1\rho_2 u_{1,1}^2 u_{1,2}^2} - 2\overline{\rho_1\rho_2 u_{1,1}^2 u_{1,2}} \cdot \widetilde{u_{1,2}} + \overline{\rho_1\rho_2 u_{1,1}^2} \cdot \widetilde{u_{1,2}}^2 + 2\overline{\rho_1 u_{1,1}^2} \cdot \overline{\rho_2 u_{1,2}} \cdot \widetilde{u_{1,2}} \\
&- \overline{\rho_1 u_{1,1}^2} \cdot \overline{\rho_2} \cdot \widetilde{u_{1,2}}^2 - 2\overline{\rho_1\rho_2 u_{1,1} u_{1,2}^2} \cdot \widetilde{u_{1,1}} + 4\overline{\rho_1\rho_2 u_{1,1} u_{1,2}} \cdot \widetilde{u_{1,1}} \cdot \widetilde{u_{1,2}} + 2\overline{\rho_1 u_{1,1}} \cdot \overline{\rho_2 u_{1,2}^2} \cdot \widetilde{u_{1,1}} \\
&- 4\overline{\rho_1 u_{1,1}} \cdot \overline{\rho_2 u_{1,2}} \cdot \widetilde{u_{1,1}} \cdot \widetilde{u_{1,2}} + 2\overline{\rho_1 u_{1,1}} \cdot \overline{\rho_2} \cdot \widetilde{u_{1,1}} \cdot \widetilde{u_{1,2}}^2 - 2\overline{\rho_1\rho_2 u_{1,1}} \cdot \widetilde{u_{1,1}} \cdot \widetilde{u_{1,2}}^2 \\
&+ \overline{\rho_1\rho_2 u_{1,2}^2} \cdot \widetilde{u_{1,1}}^2 - 2\overline{\rho_1\rho_2 u_{1,2}} \cdot \widetilde{u_{1,1}}^2 \cdot \widetilde{u_{1,2}} + \overline{\rho_1\rho_2} \cdot \widetilde{u_{1,1}}^2 \cdot \widetilde{u_{1,2}}^2 - \overline{\rho_1} \cdot \overline{\rho_2 u_{1,2}^2} \cdot \widetilde{u_{1,1}}^2 \\
&+ 2\overline{\rho_1} \cdot \overline{\rho_2 u_{1,2}} \cdot \widetilde{u_{1,1}}^2 \cdot \widetilde{u_{1,2}} - \overline{\rho_1} \cdot \overline{\rho_2} \cdot \widetilde{u_{1,1}}^2 \cdot \widetilde{u_{1,2}}^2 - \overline{\rho_1 u_{1,1}^2} \cdot \overline{\rho_2 u_{1,2}^2} \quad \text{(A.1)}
\end{aligned}
$$

At first, this equation proved to be effective. Figure A.1(b) shows R_{1111} data with a number of time delays and spatial offsets for a point with coordinates **(8.02,0,-1.25)** in the flow field. The expected trends were met with equation A.1. Peaks of the data with spatial separations are shifted and decayed compared to the zero spatial separation solution. Also, all solutions decay to zero as time delays are increased. One can compare (a) and (b) from figure A.1 to see the effect of both spatial and temporal resolution on the correlation values. Figure A.1(b) is a much smoother plot due to increased resolution. While this one pass equation proved to be an effective way to calculate the cross correlation tensor, it was found to consume too much memory when analyzing entire flow fields. Therefore, this equation was not used for the rest of the study, and the three pass system was introduced. Using this equation would have saved significant time calculating the cross correlation terms though. Therefore, it was necessary to show the validity of this equation.

A.3 MATLAB's Gaussian Curve Fitting Tool

Before the three pass system was created, the calculated data from the single pass equation was fit to basic Gaussian curves. The formula for these Gaussian curves was much

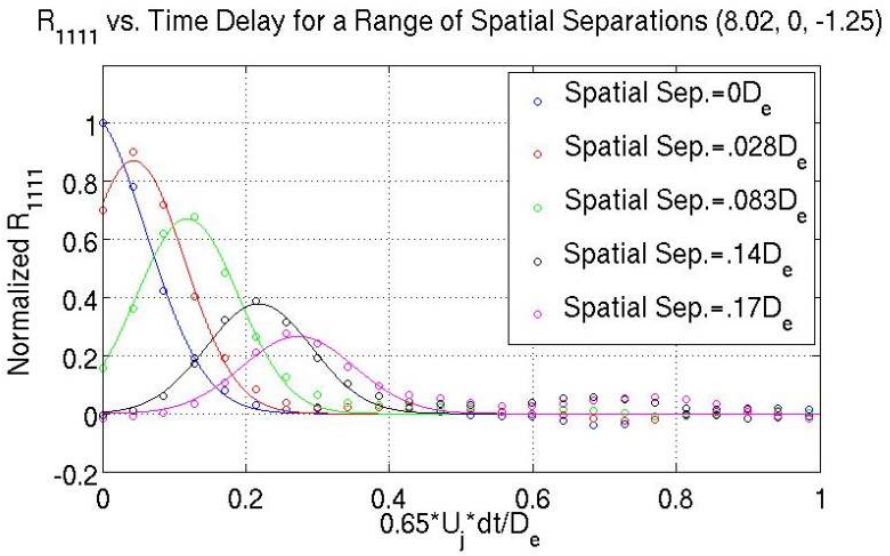

Figure A.2: Basic Gaussian model fit to the R_{1111} calculations at coordinates of (8.02,0,-1.25) using the single pass equation.

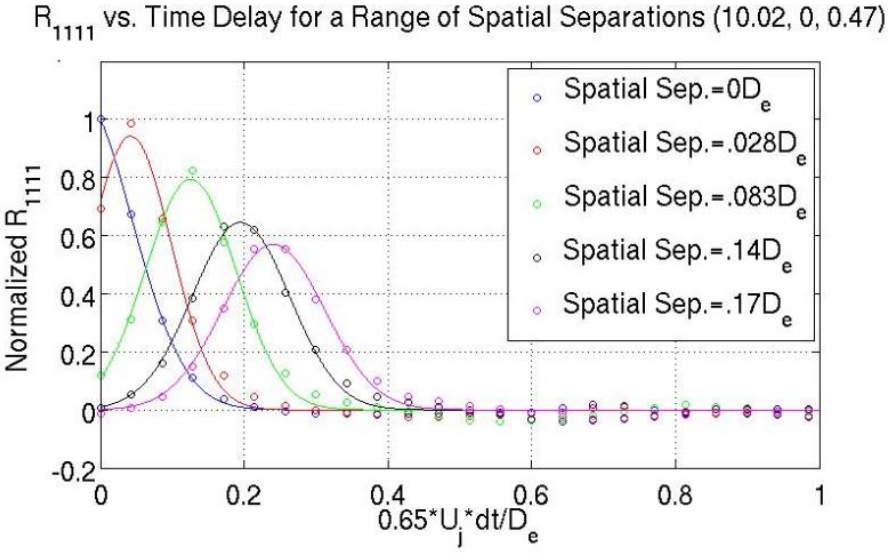

Figure A.3: Basic Gaussian model fit to the R_{1111} calculations at coordinates of (10.02, 0, 0.47) using the single pass equation.

more simplified than the Gaussian equation that was described in equation 3.29. For this particular preliminary study, the basic curve fitting tool in MATLAB was used for the Gaussian fit. The equation that represents the curve fitting tool is shown as equation A.2. This equation was then fit separately to every spatial separation solution. The point of this initial study was just to see if the data were "Gaussian-like" at all. Two random points in the flow field were analyzed. The coordinates of the two points were **(8.02, 0, -1.25)** and **(10.02, 0, 0.47)**. Figures A.2 and A.3 are the final result of this study. Within figures A.2 and A.3, the data represented by the circles are the R_{1111} calculations, while the solid lines represent the Gaussian model. It became apparent during this preliminary study that the simplified Gaussian model fit the calculations surprising well. This led to the initial conclusion that the Gaussian model is a great fit to the R_{1111} data. However, as was shown throughout this thesis, a Gaussian fit breaks down farther downstream and is not a particularly good fit to the calculations.

$$y(x') = aexp\left[-\frac{(x'-b)^2}{c^2}\right] \tag{A.2}$$

A.4 Pressure calculation

First, the ideal gas equation is assumed. Equation A.3 shows the ideal gas equation.

$$P = \rho RT \tag{A.3}$$

Temperature is not included in the available simulated data, so it has to be eliminated from equation A.3. First, the expression for the gas constant, R, is plugged into equation A.3. Equation A.4 is the result.

$$P = \rho(c_p - c_v)T = \rho(c_pT - c_vT) \tag{A.4}$$

The $c_v T$ represents the internal energy, e, of the flow field. Also, one can use the expression $\gamma = \frac{c_p}{c_v}$ to form equation A.5 where γ is assumed to be 1.4.

$$P = \rho(\gamma e - e) = \rho(\gamma - 1)e \tag{A.5}$$

In order to use the total energy, E, that is part of the available data, the kinetic energy, KE, of the flow field has to be included. A generic description of this idea is shown below as equation A.6.

$$e + KE = E \tag{A.6}$$

Subbing in equation A.5 for e and an appropriate "per mass" expression for KE, equation A.7 is the result.

$$\frac{P}{\rho(\gamma - 1)} + \frac{1}{2}V^2 = E \tag{A.7}$$

Rearranging equation A.7 results in an expression for pressure, shown as equation A.8.

$$P = (\gamma - 1)[\rho E - \frac{1}{2}\rho V^2] \tag{A.8}$$

Equation A.8 represents an equation for pressure that can directly be solved using the outputted data from the study done by Nichols et al. [2]. A little more rearranging can be done that directly shows the outputted data of ρ, ρu_1, ρu_2, ρu_3, and ρE. Equation A.9 is the result.

$$P = (\gamma - 1)[(\rho E) - \frac{1}{2(\rho)}\left((\rho u_1)^2 + (\rho u_2)^2 + (\rho u_3)^2\right)] \tag{A.9}$$